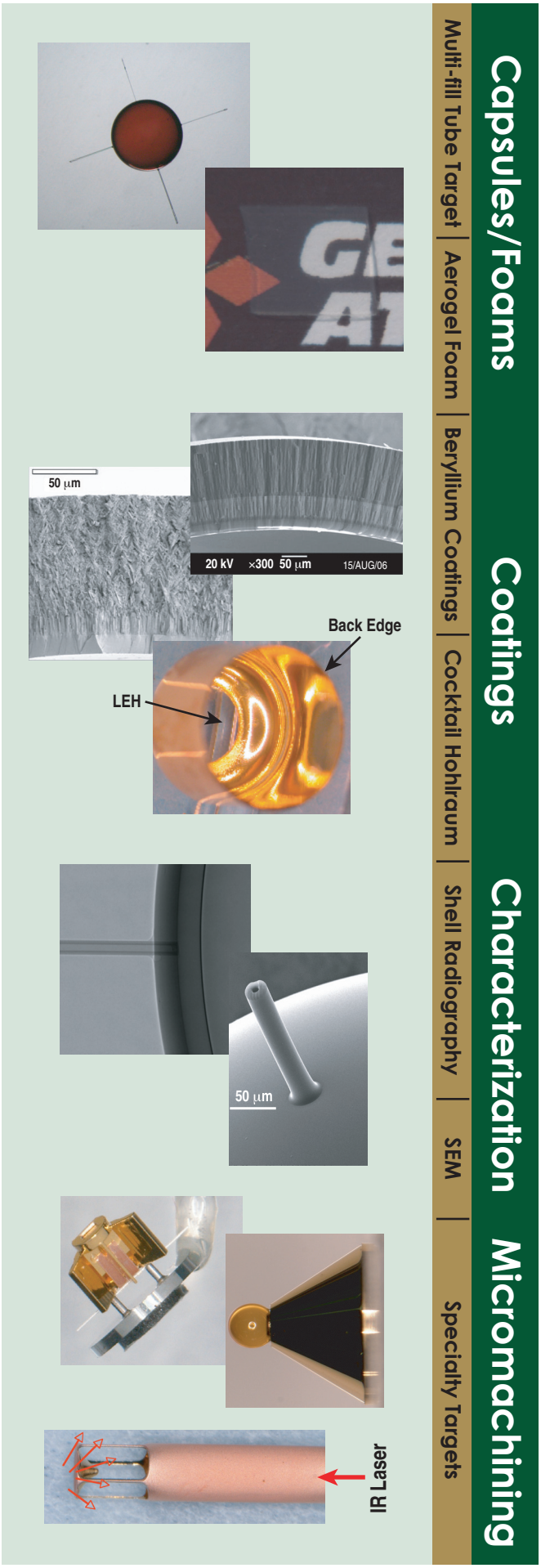

GA-A26403

INERTIAL CONFINEMENT FUSION

Final Report

March 2009

Schafer

GENERAL ATOMICS

DISCLAIMER

GA–A26403

INERTIAL CONFINEMENT FUSION TARGET COMPONENT FABRICATION AND TECHNOLOGY DEVELOPMENT SUPPORT

FINAL REPORT TO THE U.S. DEPARTMENT OF ENERGY

by
PROJECT STAFF

D.A. Steinman, Technical Editor

Work prepared under
U.S. Department of Energy
Contract No. DE-AC03-01SF22260

GENERAL ATOMICS PROJECTS 30095
DATE PUBLISHED: MARCH 2009

1. INTRODUCTION

This report documents General Atomics' (GA) final report for the Inertial Confinement Fusion (ICF) Target Component Fabrication and Technology Development Support under U.S. Department of Energy (DOE) contract DE-AC03-01SF22260. Inertial Confinement Fusion (ICF) is a research and development program of the U.S. Department of Energy National Nuclear Security Administration (NNSA). The program goals are controlled nuclear fusion at laboratory scales using large laser and pulsed power facilities in the U.S., and conducting experiments relevant to high energy density physics using those same facilities.

ICF relies on inertia to confine a mixture of deuterium and tritium (DT) for the time required to create a self-sustained fusion reaction. This also requires that the DT be highly compressed (about 1000 times solid density) and heated to about 100,000,000 deg. Matter at this kind of pressure is called a high energy density plasma (HEDP).

The ICF Ignition and High Yield Campaign supports the NNSA's Stockpile Stewardship Program (SSP). The ultimate goal of the ICF Campaign is to develop laboratory capabilities to create and measure extreme conditions of temperature, pressure, and radiation density, including thermonuclear burn conditions that approach those in nuclear weapons, and to conduct weapons-related research in these environments. Achieving HEDP conditions is critical to validate codes and to characterize weapons component performance.

The strategy to accomplish this long-term goal is centered on four objectives:

1. Achieve ignition in the laboratory and develop it as a scientific tool for stockpile stewardship.
2. Support execution of HEDP experiments necessary to provide advanced assessment capabilities for stockpile stewardship.
3. Develop advanced technology capabilities that support long-term needs of stockpile stewardship.
4. Maintain robust national program infrastructure and attract scientific talent to the SSP.

The ICF Campaign, which includes the National Ignition Campaign (NIC) and HEDP experiments, is presently executed at six sites: Los Alamos National Laboratory (LANL), Lawrence Livermore National Laboratory (LLNL), Sandia National Laboratories (SNL), the University of Rochester Laboratory for Laser Energetics (UR/LLE), the Naval Research Laboratory (NRL) and GA. GA concentrates on making the targets and doing the R&D for the targets for experiments which are carried out at several laser and pulsed power facilities. In this, GA supports all four of the above strategies of NNSA's ICF Campaign.

There are three major ICF facilities: the OMEGA glass laser at UR/LLE, the Z pulsed-power facility at SNL, and the National Ignition Facility (NIF) at LLNL. This 192 beam laser is not yet complete but has been doing preparatory experiments with a few prototype beams. These facilities are supplemented by LANL's Trident laser, NRL's Nike laser and other smaller lasers.

In FY06, the OMEGA laser accounted for the majority of experiments for ICF and HEDP. It fires about 10 times per day on an average of 3 days per week, and in FY06 fired about 1400 shots, with half of the shots for external users. Each shot requires a new target and generally there is a completely different type of tightly specified and well-characterized target for each day or half day of shots. In FY06, the Z facilities usually fired one but sometime two shots per operating day. The facility paused operation during the FY06 summer for a major refurbishment which will be complete in the summer of FY07. In FY06, NIF fired no shots but LLNL staff were analyzing FY05 four beam NIF experiments and preparing for NIF experiments in FY08. Most of the shots on these facilities required targets that were predominantly made by GA. In FY06, GA produced about 4340 components for these facilities consisting of 250 different types. Many of the components are novel and were made by techniques requiring significant development. As the targets are the initial conditions for the experiments, the targets and components need to be accurately measured and characterized for each shot which destroys the target.

In Section 2, we report on the target deliveries for these facilities. By the nature of experiments, there is always an issue of specifying the target well enough in advance for complete manufacture and characterization of the target to specification. The experimentalists often delay specifying the target, pending analysis of previous experiments and computer simulations, but several months are often required for fabrication, which often requires some development and characterization. In FY06, GA started working closely with LLNL to manage the rolling specification of hundreds of targets per year required for OMEGA. At the end of FY06, some of the other sites began to participate in this more rigorous target fabrication scheduling process.

In Section 3, we report on research and development work for targets for the ignition campaign on the NIF (NIC Target Development) and for current deliveries for OMEGA (NIC x-ray drive target production and NIC direct drive target production), Z (SNL Target Development and Production) and the NRL laser target development. The work for NRL was subcontracted to Schafer for half of FY06 and was moved outside of the scope of GA's contract for the second half of FY06.

Demonstration of laboratory ignition is the highest priority and a major objective of NNSA. This work is encompassed in the NIC which is an enhanced management activity of the NNSA, managed with the rigor of a project. There is a point design for the ignition target for the NIC. Major R&D is required to produce this target for 2010 due to the demanding specification on the ignition targets, the cryogenic capability required for ignition, and the higher quality standards required for experiments on the NIF.

In FY06, GA became the major program participant in the development of the non-cryogenic components of the new NIC targets. These include fuel capsules with graded doped ablators with

micron-scale fill tubes. The specifications on the surface finish, roundness, uniformity, doping fraction, fill tube fillet, etc., are demanding. The cryogenic hohlraum that contains the capsules is continuing to evolve. GA is fabricating the prototypes and pieces used in current cryogenic fuel layering experiments. An accelerated program of R&D and preparing for facilitization to produce hundreds of targets per year is required to ensure the success of the NIC.

Development for current x-ray drive targets on OMEGA includes surrogate target components that are shot on OMEGA in preparation for NIC development work. For current direct drive targets on OMEGA, development includes novel ways of attaching fill tubes to direct drive targets, ways of making targets to achieve enhanced implosion performance and x-ray yield for backlighting. Research for SNL includes a design to create targets for Z with many fill tubes on the large Z targets enabling several experiments on one shot to help examine the way the fill tube itself perturbs an implosion. Developments at Schafer include a dual density foam target.

2. DELIVERIES

2.1. Overview

GA and Schafer supplied a wide range of ICF components to LLNL, LANL, NRL, SNL, UR/LLE, and others in FY06. Tables 2-1 through 2-4 summarize these deliveries by quarter.

Table 2-1
First Quarter FY06 Deliveries
(Miscellaneous components are foam assemblies and flat targets)

	Orders	Capsules	μMachined Components	Miscellaneous
LLNL	12	380	193	49
LANL	4		79	
SNL	1		4	25
UR/LLE	9	240	192	
Miscellaneous	2	—	75	—
TOTAL	**28**	**620**	**543**	**74**

Table 2-2
Second Quarter FY06 Deliveries

	Orders	Capsules	μMachined Components	Foams	Miscellaneous Including Assemblies
LLNL	32	350	158		93
LANL	10	45	106		
SNL	75	22	36	17	89
UR/LLE	48	289	94	48	31
Miscellaneous	6	13	20	—	9
TOTAL	**171**	**719**	**414**	**65**	**222**

Table 2-3
Third Quarter FY06 Deliveries

	Orders	Capsules	μMachined Components	Foams	Miscellaneous Including Assemblies
LLNL	17	30	175		3
LANL	6	30	166	40	
SNL	33		5		98
UR/LLE	13	170	102		
MISC.	4	10			52
TOTAL	**73**	**240**	**448**	**40**	**153**

Table 2-4
Fourth Quarter FY06 Deliveries

	Orders	Capsules	μMachined Components	Foams	Miscellaneous Including Assemblies
LLNL	18	20	161		12
LANL	4	15	33		16
SNL	6	7			33
UR/LLE	20	238	35	17	
MISC.	16	40	111		35
TOTAL	**64**	**320**	**340**	**17**	**96**

A grand total of over 4340 target and target components were fabricated for the national program by the GA/Schafer team. The totals for the year are displayed in Table 2-5.

Table 2-5
FY06 Deliveries

	Orders	Capsules	μMachined Components	Foams	Miscellaneous Including Assemblies
LLNL	79	780	687		157
LANL	24	90	384	40	16
SNL	115	29	45	17	245
UR/LLE	90	937	423	65	31
MISC.	28	63	206		127
TOTAL	**336**	**1899**	**1745**	**122**	**576**

2.2. Capsule Support for LANL

Our group coordinated delivery of 105 targets for 12 separate orders in FY06 to LANL with most targets focused on silicon-doped glow discharge polymer (Si-GDP) glass capsules for OMEGA experimental campaigns.

We developed a new technique to implant bromine into the PVA permeation barrier layer on a glow discharge polymer (GDP) capsule with our spin dipping process. The brominated CH capsule was utilized for bromine spectra analysis on OMEGA.

We advanced Si-GDP-to-glass capsule production methods by developing processing conditions necessary to fill the capsules with various high-Z gases and reduced remaining internal residual gases to nominally 0.1 atm. We added diagnostic capability via a mass spectrometer to better quantify the partial pressures of residual gases in the Si-GDP glass capsules as well.

2.3. Capsule Support for LLNL

Our group coordinated delivery of 692 targets for 21 separate orders in FY06 to LLNL. Several target designs were supported including titanium-doped glow discharge polymer (Ti-GDP) capsules with surrogate fill tubes, Si-GDP glass, and double-shell target assemblies. Additional production effort went into supplying poly-α-methylstyrene (PAMS) and GDP mandrels for beryllium (Be) coating studies at LLNL.

We provided multilayered Ti-GDP capsules with a PVA permeation barrier and outer GDP layer. Surrogate CH fill tubes of various diameters were added to these capsules at GA, with additional GDP "bumps" added at LLNL, with the intent to compare implosion characteristics of each on the same capsule.

The Si-GDP glass orders utilized new processing conditions developed to provide high-Z gas fills and residual gas reduction. We developed a technique to fill and seal double-shell targets with neopentane utilizing uv glue as well.

2.4. Capsule Support for SNL

Our group coordinated delivery of 55 targets for 7 separate orders in FY06 to SNL, most of which were delivered before the Z machine retrofit in 2006. We provided capsules for Dynamic Hohlraum and surrogate fill tube experiments on Z, as well as components and assembly for developmental fast igniter targets.

For the Dynamic Hohlraum campaign, we provided GDP capsules with a PVA permeation barrier filled with argon (Ar). The surrogate fill tube capsules consisted of standard multilayer GDP and Ge-doped GDP capsules; however, a majority of the delivery effort was expended on developing multiple SiO_2 and polyimide (PI) fill tubes attached to individual capsules to study effects of tube diameter

and length on implosions. New techniques for laser drilling blind fill tube mounting holes were developed.

We supplied the inner and outer GDP hemi-shells for fast igniter targets and assisted in developing an assembly method to mount the challenging inner GDP hemi-shells.

2.5. UR/LLE Deliveries

Our group continues to coordinate delivery of a wide range of targets to UR/LLE. In 2006, we delivered 1456 targets for 90 separate orders to UR/LLE. This year the capsule delivery emphasis was on cryo shells.

Cryogenic experiments at UR/LLE were supported by the production of thin walled "strong" CD capsules. These were analyzed for burst and buckle pressure. Each delivered shell was wallmapped for wall uniformity and spheremapped for comparison to the "NIF" standard.

Deuterium-filled drop tower glass shells were delivered for use as "backlighters". In addition, we produced diagnostic shells and shells for polar direct drive experiments.

High density (200 mg/cc) resorcinol formaldehyde (RF) foam shells with a GDP permeation barrier were produced for room temperature surrogate shots. This year we developed the capability to coat the GDP/RF foam shells with a thin (~1000Å) layer of aluminum to serve as a permeation barrier. Delivered shells were screened for deuterium (D_2) half-life before shipment to UR/LLE.

Divinylbenzene (DVB) foam cylinders were produced at densities of 70, 100, and 200 mg/cc. We developed monolithic fill tubes (MFT) for shells. Shells with tubes were measured and tested for permeability and buckle pressure. Shells with surrogate fill tube CH "tails" were made to study the affect of the stub on capsule implosions.

2.6. SPECIAL TARGET CENTER

The Special Target Center at GA has fabricated, characterized and assembled several new types of ICF and High Energy Density Physics targets in collaboration with UR/LLE and LLNL. Examples include: NIC shock-breakout targets, ice layering diffusers, isentropic compression experiment targets and 1-D and 2-D x-ray source targets.

The shock-breakout target is a cone-in-capsule target. The cone acts as a plasma shield to allow observation of the shock-breakout on an imploding GDP capsule. Experiments performed at UR/LLE on these targets have permitted measurements of breakout time and shock velocity as a function of capsule thickness. Figure 2-1 shows a schematic of a shock-breakout target and Fig. 2-2 is a photomicrograph of an assembled target. The cone is made from a gold plated micromachined copper mandrel. The capsule is a GDP capsule made by the depolymerizable mandrel technique. The GDP capsule is diamond machined to create a hole that fits on the end of the gold cone. Figure 2-3 shows two photomicrographs, the one on the left is the view of the hole on the cone through the GDP capsule and the one on the right is a view of the inside of the capsule through the hole in the cone.

Future shock-breakout targets will consist of cryogenic cone and capsule targets to enable measurement of shock propagation into condensed fuel. These targets will require a leak tight joint between the cone and capsule and a fill tube.

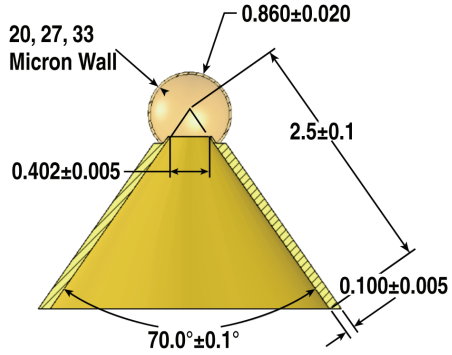

Fig. 2-1. Schematic of a shock-breakout target.

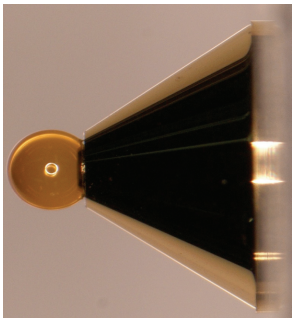

Fig. 2-2. Photomicrograph of a shock-breakout target.

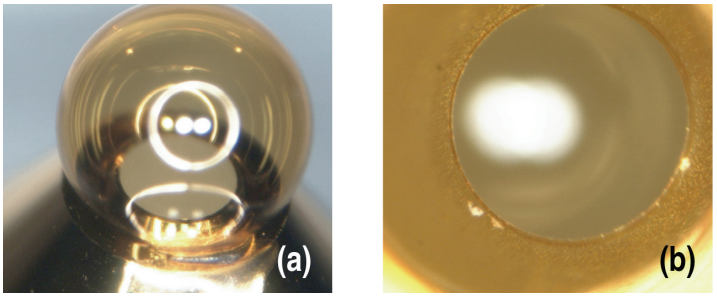

Fig. 2-3. (a) View of the hole on the cone through the GDP capsule and (b) view of the inside of the capsule through the hole in the cone.

Ice layering experiments at UR/LLE with deuterium utilize an incident IR laser for ice layering, however, localized heating from the IR laser can result in non-uniform ice layers. A uniform ice layer can be achieved with the help of a diffuser. The diffuser provides uniform illumination by scattering the IR laser light via the cusp on one end of the diffuser. Figure 2-4 is a photomicrograph of the diffuser illustrating diffusion of the IR laser light. The design for the diffuser was done as a collaboration effort between UR/LLE and GA. The diffuser is a multilayer part consisting of a spectral reflective gold layer, a nickel diffusion barrier layer and a copper structural layer. The layers were deposited on an aluminum mandrel that has one end micromachined with the cusp shape. After all the layers are deposited, the aluminum mandrel is removed by dissolving it in diluted sodium hydroxide. The diffuser is in one of the UR/LLE cryostats ready to be tested.

The Material Science group at LLNL is studying lattice compression by means of isentropically compressed experiments (ICEs) to obtain information on the kinetics of transformation and lattice relaxation. GA has fabricated the components and assembled the targets for these dynamic x-ray diffraction experiments. In these experiments, lasers are used to generate both a shock in a solid and

the x-rays to image the lattice in motion. GA improved the design of the target by designing the backlighter as a single component and making it out of gold. Using a monolithic backlighter increased shielding and minimized film exposure from the x-rays emitted from the expanding backlighter foil plasma. In the fabrication of the backlighter, the Special Target center implemented CAD/CAM in its fabrication. The part design, milling tool path, and part machining were first tested on a computer before any metal was cut. Figure 2-5 is a photomicrograph of the assembled diffraction target. Figure 2-6 is a photomicrograph of the gold monolithic backlighter.

Fig. 2-4. Photomicrograph of the diffuser.

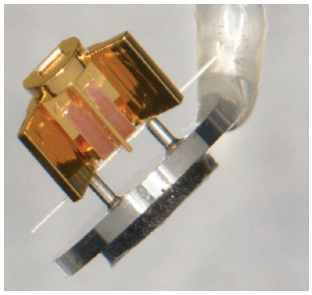

Fig. 2-5. Photomicrographs of the ICE diffraction target.

Fig. 2-6. Photomicrograph of the gold backlighter.

GA is also helping LLNL with the development of high-energy K-alpha backlighters for high-energy density physics experiments by designing and fabricating backlighter targets. The goal is to produce 15 to 100 keV x-rays with 10 to 20 μm spatial resolution as x-ray sources for future experiments in NIF, ZR and OMEGA-EP.

Targets will increase in complexity as new and more powerful laser systems come on line and GA will continue enhancing its fabrication capabilities enabling a wide variety of high quality targets.

3. DEVELOPMENT

NIC TARGET DEVELOPMENT

3.1. THERMAL AND ELECTRICAL CONDUCTIVITIES OF ELECTROPLATED GOLD — T.P. Bernat, N.B. Alexander, J.L. Kaae (GA)

For fuel capsules mounted at the center of cryogenically cooled gold hohlraums,[1] the thermal conductivity of the gold is an important parameter in determining the fuel layer thickness uniformity at shot time. Gold hohlraum walls are fabricated by electroplating onto a machined copper mandrel, which is removed by dissolving in an acid solution. Details of the entire process are given in an earlier paper by Elsner [3-1]. To study the thermal conductivity of the electroplated gold and the effects of varying plating conditions, we made measurements of the electrical resistance of prepared samples at room temperature and at 4.2 K, and related these to the thermal conductivity through the Weidemann-Franz law:

$$\frac{\kappa}{\sigma} = L^{*}T \quad , \tag{3-1}$$

where L is the Lorentz number. Then

$$\frac{\kappa_{4.2}}{\kappa_{300}} = \frac{RRR}{71} \quad . \tag{3-2}$$

In Eq. (3-2), RRR is the "residual resistivity ratio", which is the ratio of room temperature and 4.2 K resistivities.

3.1.1. Experimental

Our aqueous gold electroplating baths are prepared with proprietary components from *Enthone*.[2] The main bath component is sodium aurosulfate [$Na_3Au(SO_3)_2$]. A brightener which contains arsenic in the form of dioxoarsenate ($NaAsO_2$) has traditionally been added to refine the grains and improve surface finish.[2] In this study, we varied the bath brightener concentration (0, 2.65, 5.3, and 7.95 cc/l) and the plating current (1, 4, and 10 mA/cm^2). For comparison, nominal values of these parameters used in our lab for typical gold platings are 5.3 cc/l and 4 mA/cm^2. Samples were prepared by plating onto 0.5 cm diameter copper cylinders 2 cm long. All samples were 40 μm thick as measured by laser micrometer with 0.1 μm measurement precision. At least two samples were made at each coating condition to check for reproducibility. Four-lead solderless electrical resistance of the sample

[1] The presence of a thin "cocktail" layer comprising a mixture of gold and uranium on the inside surface of the hohlraum may change the exact details of the thermal field problem, but not its general nature.
[2] BDT 510 from Enthone-OMI.

cylinders was measured using a current source settable to 0.01 A and a nano-volt meter (Fig. 3-1). Resistance was measured for each sample at room temperature (21±1°C in our laboratory) and 4.2 K.

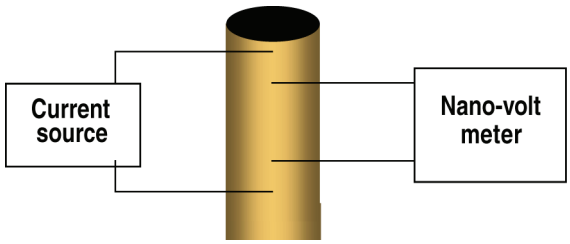

Fig. 3-1. Resistances of hollow electroplated gold cylinders were determined from four-point measurements. All specimens had the same dimensions.

3.1.2. Results

Our main experimental results are given in Fig. 3-2. Each symbol in the figure represents measurement of a different sample. We find that the measured electrical *RRR*s are maximized at about 30 for 4 mA/cm^2 with no brightener in the bath. Since nearly all gold has a thermal conductivity of about 3.3 W/cm-K at room temperature, then by Eq. (3-2), the thermal conductivity at 4.2 K will be about 140 W/m-K. Even our smallest additions of brightener drastically lower the *RRR*, and thus κ at 4.2 K.

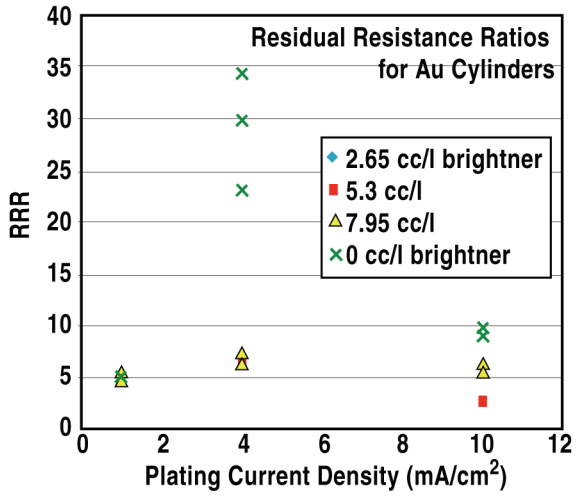

Fig. 3-2. Residual resistance ratios peak at 4 mA/cm^2 with no brightener.

As a check of our technique with this apparatus, we measured the *RRR* of a 99.99% pure gold foil to be 72. While this does not constitute a standard, the result is within the range to be expected.

3.1.3. Discussion

The electroplating literature reports that the grain size of deposited metals decreases when brightener is added to the plating solution, and also decreases with increasing plating current density [3-2]. A model of the effects of small grain size on electrical conductivity was developed by Mayadas and Shatzkes [3-3]. Their model shows that the total resistivity including grain boundary scattering, ρ_g, relative to the "intrinsic" resistivity ρ_0, which includes impurities and defects but not grain boundaries, increases with the ratio of the intrinsic mean-free-path (mfp) to the average grain size. The electron reflection coefficient at the grain boundaries is left as a free parameter. From the electrical conductivity of gold, we estimate the intrinsic mfp for conduction electrons at the Fermi surface at about 40 nm at room temperature and about 4 μm at 4.2 K. Mayadas and Shatzkes find that the electron reflection coefficient for Cu and Al are around 0.2. Assuming the same for Au, from our result that with no brightener and 4 mA/cm^2 the *RRR* at 4.2 K is about one-third that of pure gold, we estimate that the average grain size for those conditions is about 670 nm. At 10 mA/cm^2 and no brightener, the *RRR* is about 0.1 that for pure gold, leading to an average grain size of 150 nm.

Based upon the Mayadas and Shatzkes model, some of the decrease in *RRR* upon addition of brightener results from decrease in grain size. However, brightener also adds impurities, decreasing the intrinsic mfp and increasing the resistivity. We examined several of our samples for impurities by inductively coupled plasma mass spectroscopy. The results for copper and arsenic are shown in Fig. 3-3. Sodium, if present, was less than the detection limit of 50 ppm. The As source is the brightener, while the Cu most likely is from the coating mandrels. Consequently, Fig. 3-2, at 4 and 10 mA/cm^2 the impurities significantly reduce the *RRR*. All of the reduction at 4 mA/cm^2 can be ascribed to a reduction of grain size to about 100 nm. Since the room temperature resistance only increases about 10% for these samples, indicating about the same decrease in intrinsic mfp, this is a reasonable conclusion. At 10 mA/cm^2 the room temperature resistivity increases by about 40%, so the *RRR* reduction can be accounted for by a 40% decrease in intrinsic mfp and average grain size decreased to between 20 and 60 nm.

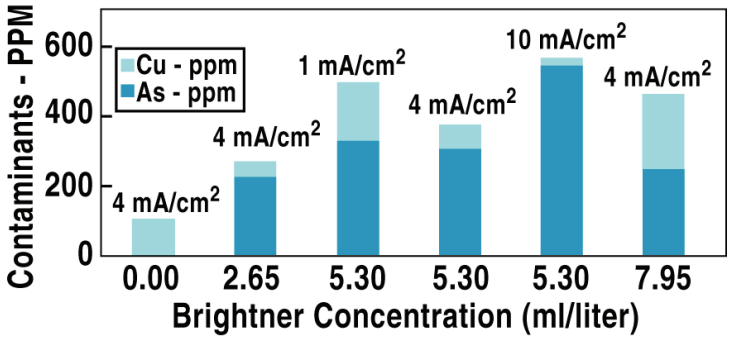

Fig. 3-3. Arsenic and copper contamination concentrations as a function of brightener concentration and plating current density.

The data at 1 mA/cm^2 is puzzling. All of the *RRR*s collapse to a single value of 5.1±0.3, almost independent of brightener concentration. To explain this, the no-brightener point would require 70 nm grains. Why this might occur is not clear, since as already mentioned, grain sizes are reported to increase with decreasing plating current density, and adding brightener further reduces the grain size. Be that as it may, a grain size small enough that it, rather than the impurities, limits the conductivity at 4.2 K would explain the data. While we can interpret out results in terms of the Mayadas and Shatzkes model, corroboration requires measurement of actual grain size in our samples.

3.2. DRILLING OF SMALL HIGH ASPECT RATIO HOLES IN BERYLLIUM SHELLS — A. Forsman, E. Lundgren (GA)

The NIC specification calls for holes that are nominally 5 μm in diameter to be drilled in Be shells whose wall thickness exceeds 150 μm. The specification defines the hole size in terms of a mass defect, stating that no more mass than 125% of a cylindrical 5 μm diameter hole may be removed, not counting a surface that receives the fill tube. The drilling process is therefore comparable to drilling a long thin pipe since the aspect ratio of the hole, the ratio of the depth to the diameter, is higher than 30:1.

Femtosecond lasers have been used to drill these fill holes [3-4], although early attempts produced holes that tended to filament into multiple diverging holes that could eventually encompass a region 30 μm in diameter instead of a single small fill hole. The hole entrances were clean, but the focusing lenses that had been used were very short and had a working distance of a few millimeters and, consequently, were subject to being fouled by debris ejected from the hole during drilling.

A novel nanosecond laser technique was chosen to overcome these limitations. Previously, GA developed a double-pulse format for nanosecond laser ablation [3-5]. This technique used relatively simple laser equipment, produced excellent high aspect ratio holes in diesel fuel injectors, and was implemented using a plano-convex focusing lens having a focal length of 25 mm, which nearly eliminates fouling by the ejected debris. The shells were drilled in a vacuum chamber that was equipped with optical systems for characterizing the laser focal spot and targeting the shell (± 30 μm accuracy), and a XYZ linear motion control system for positioning the shells. The chamber was evacuated to a pressure of less than 200 mTorr during drilling, and the laser focal spot was 5 μm in diameter. The double-pulse laser format was generated by splitting the output beam of a single laser into two beams using a partial reflector, propagating one of the beams through a delay loop that added 20 ns to its propagation time, and then recombining the two beams using another partial reflector. The laser source [3-6] produced 10,000 laser pulses each second, and each pulse was less than 4 ns in duration and contained 150 μJ. A waveplate-polarizer combination was used to reduce the output power. The partial reflectors in the system were chosen so that the primary and secondary pulses in each double pulse pair had approximately equal energies. A high speed shutter system was used to regulate the exposure times.

It was found that high quality holes in Be shells could be produced in less than 1 s using the double-pulse nanosecond technique (Fig. 3-4).

It was discovered that if the laser power was severely reduced, a through hole could not be drilled. If the laser power was too high, the hole diameter increased (Fig. 3-5).

Interactions between the hot ablation plasma and the bore walls are suspected to be the cause of this phenomenon (Fig. 3-6). Therefore, a combination of plasma and material properties may ultimately limit the aspect ratio when laser drilling small holes. If the intensity is too low, then the hole cannot be drilled due to transmission losses and damage thresholds. On the other hand, increasing the laser intensity causes the resultant plasma to ablate additional material from the bore walls as the plasma exits the hole, thereby enlarging the hole.

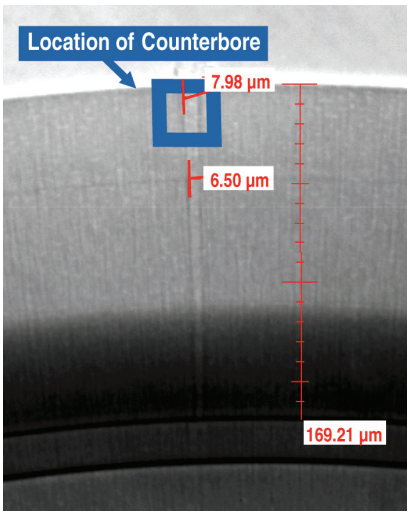

Fig. 3-4. NIC specification hole.

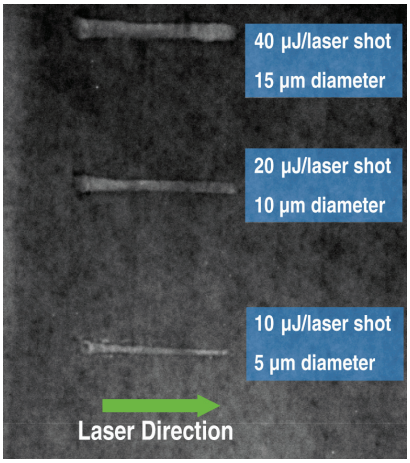

Fig. 3-5. Increasing the laser intensity increases the hole size.

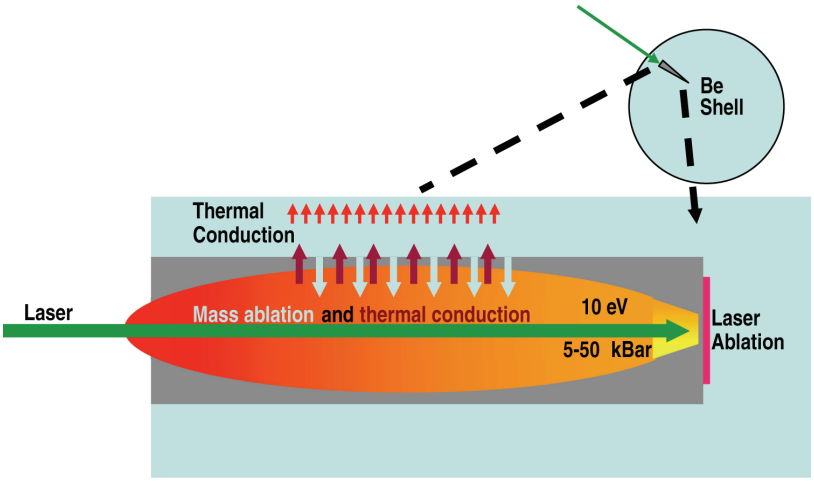

Fig. 3-6. The laser produced plasmas may cause the hole size to increase when the laser intensity increases.

3.3. BERYLLIUM CAPSULE COATING DEVELOPMENT FOR NIF TARGETS — H.W. Xu, L.A. Dixon, K.A. Moreno, A. Nikroo, J.R. Wall, K.P. Youngblood (GA), J.C. Cooley (LANL), C.S. Alford, R.C. Cook, R.E. Hackenberg, S.A. Letts (LLNL)

A graded copper-doped Be capsule is the current NIF point design for ignition in 2010. The point design sets a series of specifications for the capsules to meet, which include coating density, void defect size and volume, outer and inner surface roughness, x-ray optical depth uniformity and impurity levels. Be coatings on spherical surfaces have been developed at LLNL and later at GA for the production of Be capsules. A magnetron sputtering technique was used due to its lower temperature operation and the denser films it produced by energetic species [3-7,3-8]. Previous efforts have focused on improving Be coating density and getting uniform and consistent microstructures. Be coatings were produced by sputtering Be targets onto CH mandrels placed in a pan with bouncing agitation. As pointed out in previous papers [3-9,3-10], Be coatings produced in this way showed a variety of growth modes, such as nodular growth and twisted grain structure, and they typically have low densities. Surface roughness was found to increase with coating thickness. Although the outer surface can be polished to NIF specifications, a smooth growth front surface is desired because it leads to a smooth interface between layers, which may affect optical depth uniformity.

In addition to all of the structure and roughness requirements, the NIF capsule has to be able to hold fuel gas for cryogenic layering. Based on this requirement, a specification was defined for deuterium gas retention half-life of greater than seven days. Be coatings were found to show columnar grains with characteristic defects, such as scattered voids along grain boundaries and fine striation line defects. It is shown that Be coatings with columnar structures have very short gas retention half-lives, which poses a serious challenge for developing usable NIF capsules. One solution is to interrupt the columnar structure with a permeation barrier layer. We developed a permeation barrier layer for Be coating and dramatically improved the gas retention half-life of Be capsules.

3.3.1. Results

In our previous publications, we demonstrated that when using bouncing agitation with a higher coating rate, the film microstructure showed twisted columnar structure with low density. However, when the agitation was changed to rolling and coating at lower deposition power, the microstructure showed uniform columnar structure. Figure 3-7(a) shows scanning electron microscopy (SEM) cross sections of a twisted structure obtained at higher coating power with bouncing agitation and Fig. 3-7(b) shows uniform columnar structure at lower power with rolling agitation. In Fig. 3-7(a), it is seen that the twisted structure shows more directional coating towards the gun directions which is consistent with our sputtering configuration of three guns from different directions. The directional coating causes more shadowing and introduces more voids in the coating on spherical surfaces. The density of the coating was measured to be ~80% of Be bulk density. In Fig. 3-7(b), the columnar structure is uniform and aligned along the radial direction. The uniform structure in all directions suggests that the sputtering beam has become less directional when it reached the mandrel surface because of multiple scattering. Rolling agitation constantly removes larger surface roughness and

helps to stop larger surface roughness growth. The twisted structure at higher coating power suggests that at that condition the sputtering beam mfp is longer, which may be due to gas rarefication by more local heating at higher power. Cu doping in the coating does not change the microstructure in any fashion.

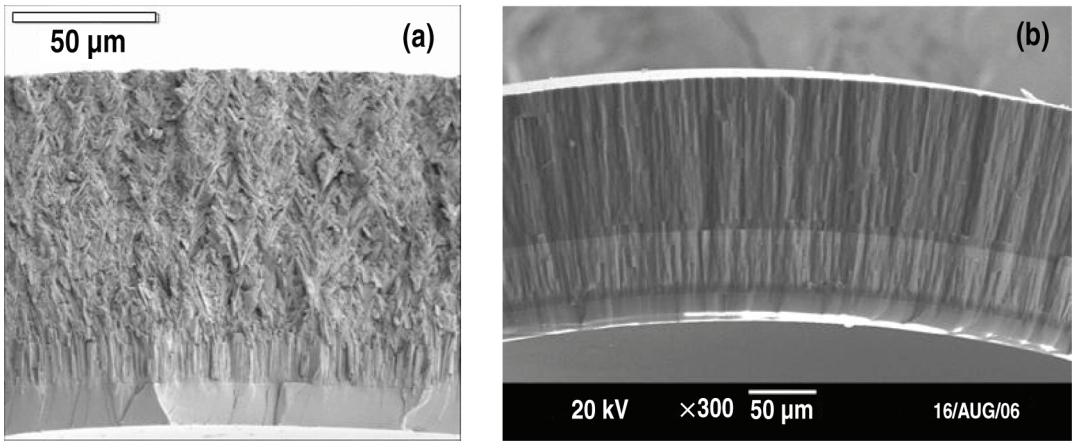

Fig. 3-7. (a) Twisted structure observed at 300 W coating power with bouncing agitation. (b) Columnar structure for a 160 μm coating obtained at 100 W coating power and rolling agitation. The light color region in (b) is a Cu doped layer.

Using TEM, we have compared the defects from low density coatings obtained at higher coating power (300 W) and bouncing agitation with our recent higher density coatings obtained at lower coating power (100 W) and rolling agitation. Figure 3-8(a) shows voids with lateral dimensions larger than 500 nm for coatings of ~80% Be bulk density. Figure 3-8(b) shows small voids with lateral dimensions less than 200 nm for coatings of ~95% Be bulk density. In addition to those scattered voids, some fine intra-granular striation lines were also observed. Quantitative analysis of coating density from TEM analysis has not been accomplished. However, the size of the voids in our latest rolled coated Be coatings at lower coating power meets the NIF requirements for void size, which is 0.1 μm^3 or a lateral dimension of 400–500 nm.

With all the improvements in coating density and uniformity, attempts were made to produce NIF design graded Cu-doped Be shells to understand the precision of coating parameter control. The coating was produced by using three Be guns and one Cu gun with rolling agitation. Figure 3-9 is a comparison of layer thickness and doping level of the shell to the NIF design specification. The NIF specification was targeted for this coating. It is noted that by controlling the gun power and running time, the layer thickness and doping level can be achieved within ~10% of the target value. The deviation from the targeted value can be attributed to small, but acceptable, coating rate variations.

One way of improving shell gas retention half-life is to interrupt the columnar grain growth. During earlier development for NIF targets [3-11–3-13]. B doped Be coatings have been explored to achieve smooth surfaces due to the existence of a glassy phase for the B-Be system at 11–16 at. % B. It was experimentally confirmed that an amorphous glassy layer formed when Be was doped with B

at 11–16 at. % although the layer may be unstable at higher temperatures by transitioning to a nanocrystalline structure. A layer of amorphous Be-B is a good choice for a permeation barrier that interrupts columnar grains of Be coatings because only light elements are involved, which should not significantly change x-ray absorption.

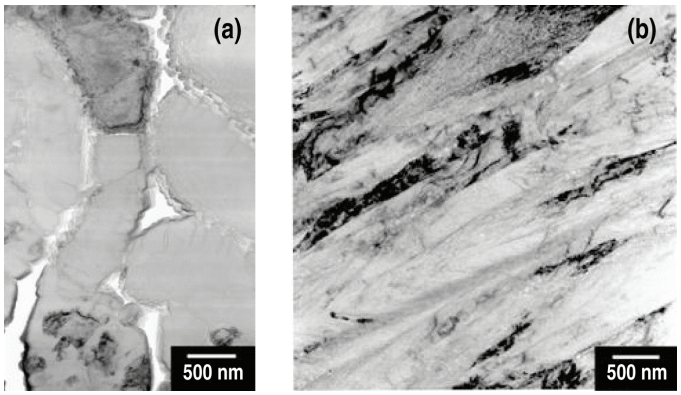

Fig. 3-8. (a) TEM of Be coating at higher coating power with bouncing agitation. Voids > 500 nm in size are shown in this image. (b) Image of Be coating obtained at lower coating power with rolling agitation. The scattered voids still exist in the coating. They are less than 200 nm in size.

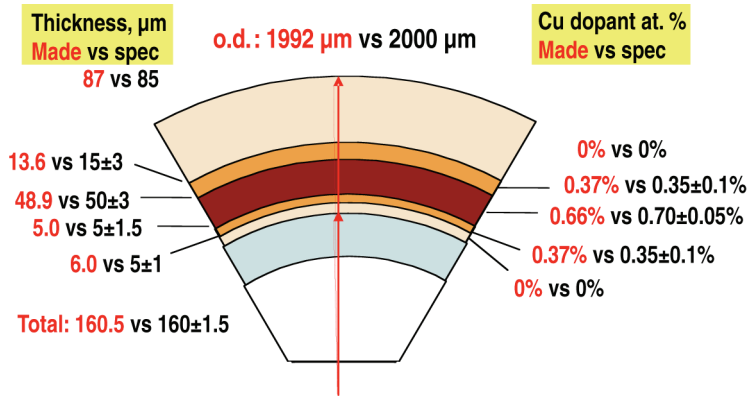

Fig. 3-9. A comparison of the layer thickness and doping levels to NIF specifications.

B-doped Be layers were co-sputtered and the concentration of B in Be was based on the sputtering rates of the two materials measured. On coating the shells, B-doped Be layers were deposited close to the inner surface of the coating because of the surface smoothness. In our experiments, B concentrations from 8% to 21% and layer thicknesses of 0.25–6 μm were tested as permeation barriers. It was found that two 0.25 μm thick layers of doped Be at 11 at. % B and separated by 0.25 μm Be achieved the best results with the longest half-life. Thicker layers of B-doped Be (up to 6 μm) were tested against leakage. The shell half-life was not found to benefit from this thicker permeation barrier. As suggested in literature [3-14,3-15] a diffusion permeation barrier has a critical thickness beyond which the permeation rate will not improve. The defects in the film

become the dominant permeation path. One possible explanation for the poorer performing permeation barrier for thicker B doped Be layers may be due to higher stress in thicker films, which may lead to microcracks and therefore higher leakage.

Figure 3-10(a) shows a comparison of half-life data for pure Be shells, Be shells with thicker B-doped layers (b) and Be shells with two 0.25 μm B-doped Be layers. It was found that for pure Be shells, the majority of the deuterium (D_2) half-lives measured were less than one day. Adding B-doped Be layers increased D_2 half-life. However, significant improvement was observed for Be shells with two 0.25 μm B doped layers. Although there is still some scatter in the measured D_2 half-life data, ~35-40% of shells showed half-lives greater than seven days, which is the current specification. There are ~20% of shells that show half-lives from 30 to 300 days.

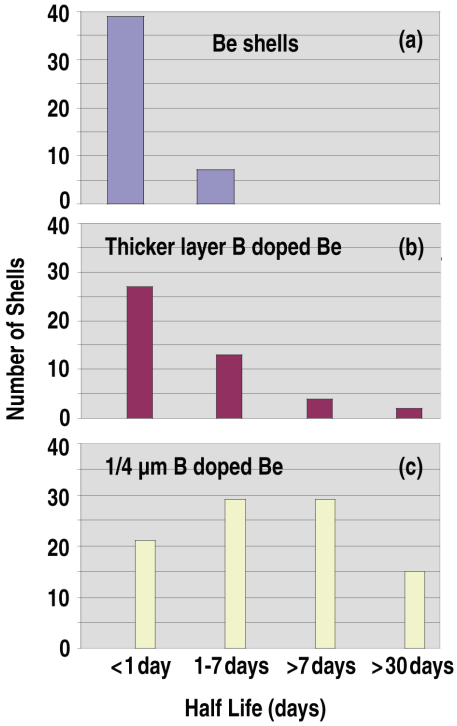

Fig. 3-10. (a) Plots of Be shell D_2 half-life for pure Be shells, (b) Be shells with 0.5–6 μm B doped Be layers, and (c) Be shells with two 0.25 μm B doped Be layers.

Summary for Section 3.3

Be shells with consistent microstructures have been developed for NIF capsule applications. The Be coatings have shown a consistent 95% bulk density, which meets the NIF specification. The voids in the coating meet the 0.1 μm^3 void volume specification. Optical depth uniformity measurements suggest that these Be shells meet the NIF specification on optical depth uniformity. Graded Cu dopant profile of Be shells suggest that the doping level can be controlled within the NIF specification for doping. Incorporation of B-doped Be layers for improving Be shell D_2 gas retention half-life showed some success in achieving a longer D_2 half-life for Be shells. They meet the current seven day D_2 half-life specification at room temperature.

3.4. REMOVAL OF CH MANDRELS FROM SPUTTER COATED CAPSULES FOR NIF TARGETS — K.P. Youngblood, K. Moreno, A. Nikroo, H. Huang, Y.T. Lee (GA), C.S. Alford, S.R. Buckley, S.A. Letts (LLNL)

The current baseline ignition design for the NIF is a graded copper doped Be shell [3-16]. These shells are fabricated using a plasma polymer (CH) shell that is sputter coated with Be [3-17]. To meet current design specifications, the inner mandrel must be completely removed. The inner surface of the Be is then characterized and must meet surface finish specifications. Previous reports on mandrel removal and capsule characterizaion [3-18,3-19] indicated some residue remained on the inner surface of the Be. Additional characterization indicated that high temperatures resulted in blistering

on Be. To refine the temperature protocol, we used the thermogravimetric analysis (TGA) to study the decomposition behavior of the CH polymer shells. We coupled this information together to develop a protocol where the temperature is high enough to remove the mandrel but below the temperature where catastrophic blistering of Be occurs.

3.4.1. Experimental

The initial temperature profile consisted of a temperature ramp from ambient to 200°C at a rate of 5°C/minute. The temperature ramp then slowed to 1°C/minute and a final temperature of 500°C. The system was set to dwell at this temperature for 60 h before cooling to ambient temperature as the furnace turned off. The inner surface of the Be shells that underwent this process was inspected. Radiographic images showed no trace of the mandrel, but shallow angle SEM images showed blistering was present on the inner Be surface. These blisters are caused by a combination of stress and gas diffusion [3-20,3-21] (Fig. 3-11). We hypothesized that reducing the oven temperature might reduce the defects. We used a TGA system to quantitatively verify the temperature and ramp rate required for complete mandrel removal. We measured the mass of the mandrel at various dwell temperatures ranging from 350°C to 600°C. The data confirmed that for plain CH mandrels, a temperature of 400°C was necessary for complete removal. When we used a temperature of 425°C in the furnace, the blistering was not evident.

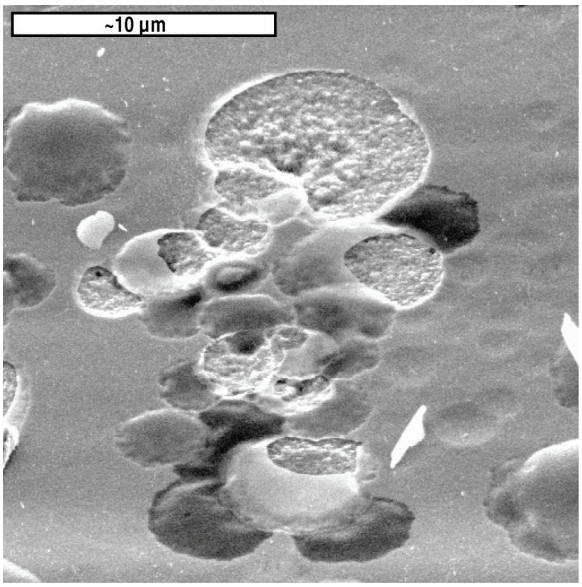

Fig. 3-11. Shallow angle SEM image of the surface finish of Be shell after pyrolysis.

To characterize the blistering, it was necessary to fracture the shell. In addition to qualitative SEM images, RMS data provided a quantitative measurement of the surface. We used interferometry rather than atomic force microscopy to look at the surface because it was necessary to look at a large area to verify that there were not isolated defects. It is not possible to mount a large shard for atomic force microscope (AFM) analysis due to the curvature of the part. A phase shifting diffraction interferometer (Spherical Interferometer) system was developed at LLNL [3-22] and used to characterize these parts (Fig. 3-12). We produced shells that met the required RMS [3-16] on the inner surface using the modified temperature profile.

Two furnace systems were used to conduct these experiments. The first system consisted of a temperature-controlled furnace that housed a tubular pressure vessel. The samples were inserted into this tube. The gas flow consisted of filtered, dried air, which was held at ambient pressure for 30 s

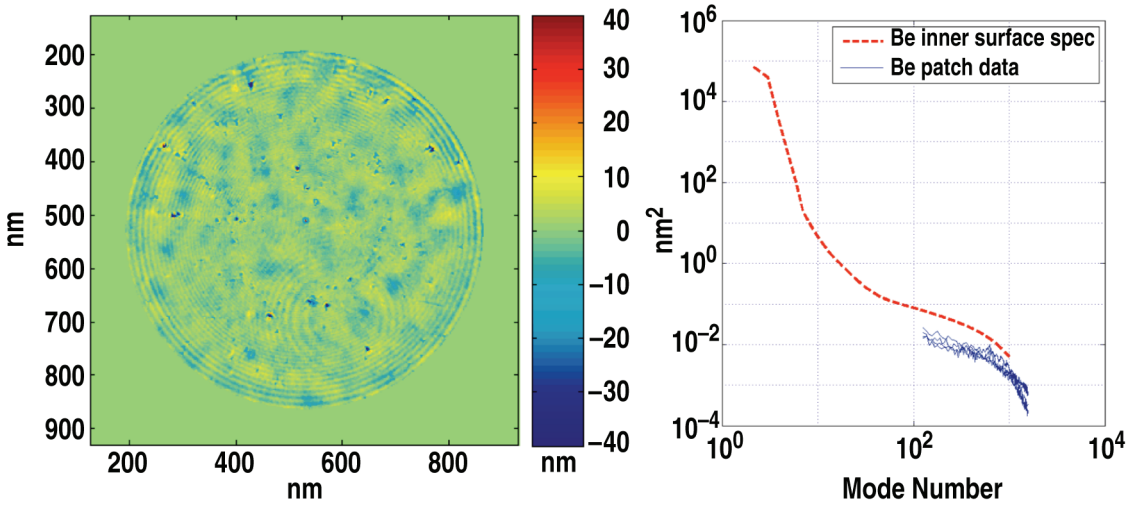

Fig. 3-12. Spherical interferometry of the inner surface of a Be capsule pyrolized at 400°C has verified that shells meet NIF specifications.

then pressure cycled to 60 psi for 30 s; this pattern was repeated throughout the 60 h removal process. The second system did not include pressure cycling; we used a standard muffle furnace that ran the specified temperature profiles in air. When the mandrels were removed in the pressure-cycled system at 400°C, radiography indicated that the interior shell surface was free of residue. However, on shells treated in the muffle furnace that did not have pressure cycling, there were some samples with areas of incomplete mandrel removal (Fig. 3-13). Curiously, EDX indicated that there is oxygen in this residue and suggests that there is a low level of Si or Mg. Ongoing experiments are verifying that pressure cycling will completely remove the mandrel and are attempting to identify the source of this contamination.

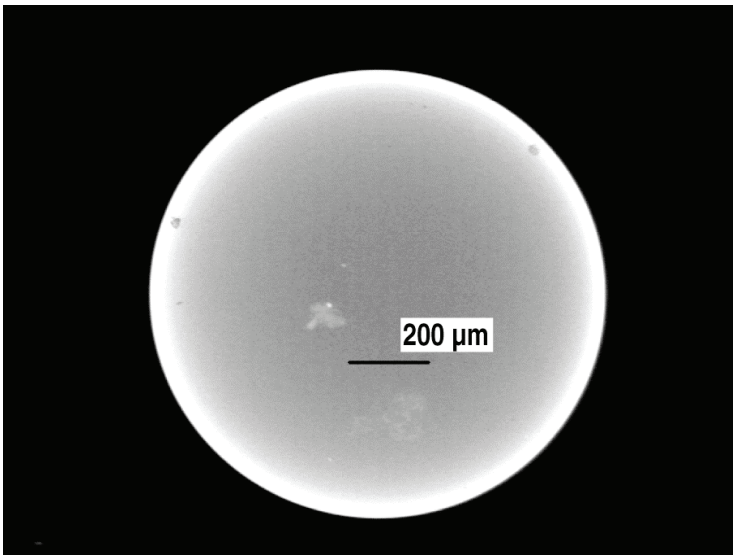

Fig. 3-13. X-Radia image of post-pyrolysis residue in Be shell.

Conclusion for Section 3.4

We developed a method for the removal of a CH mandrel from a sputtered Be coating which resulted in an inner surface finish that meets the requirements of the NIF point design. We are continuing to characterize the shells to verify use of pressure cycling to fully pyrolize the mandrel by installing pressure cycling in the system at GA. We are investigating various methods to avoid the oxygen contamination of the sample during the mandrel removal process.

The authors wish to thank Ed Lindsey of LLNL and Don Wall from GA for SEM images, and Kristie Seagraves of IAP World Services and Charlotte King of LLNL for radiography images.

3.5. PRECISION RADIOGRAPHY SYSTEM — S. Eddinger, H. Huang, R.B. Stephens, A. Nikroo (GA)

We have designed and constructed a system to accurately measure the optical depth fluctuations of a shell to 1 part in 10^4 with 120 μm resolution (Fig. 3-14). This system is based on x-ray radiography and photomultiplier tube (PMT) single-channel counting. X-rays penetrate through a shell and are converted into visible light in a scintillator. We have a system of Nikon lenses (20X and 4X) to collect the maximum amount of light by magnifying the light and matching the numeric aperture of the fiber optics. The visible light travels through fiber optic cables and is counted in the PMT. The shell rotates at 1 rpm and data is collected every 0.1 deg. A shaft encoder maintains the same zero point each rotation. This allows us to add data from the same location every rotation. Interleaving data in this way eliminates systematic error due to x-ray spot drift.

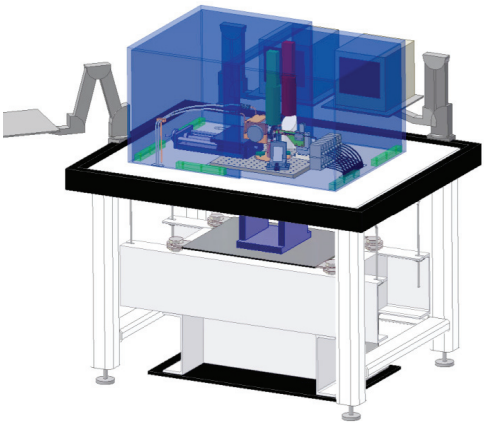

Fig. 3-14. Precision radiography CAD drawing.

Initial testing showed that we were able to eliminate systematic error due to x-ray spot drift, but there were errors due to increases in the vacuum post wobble [Fig. 3-15(a)]. To fix this, we

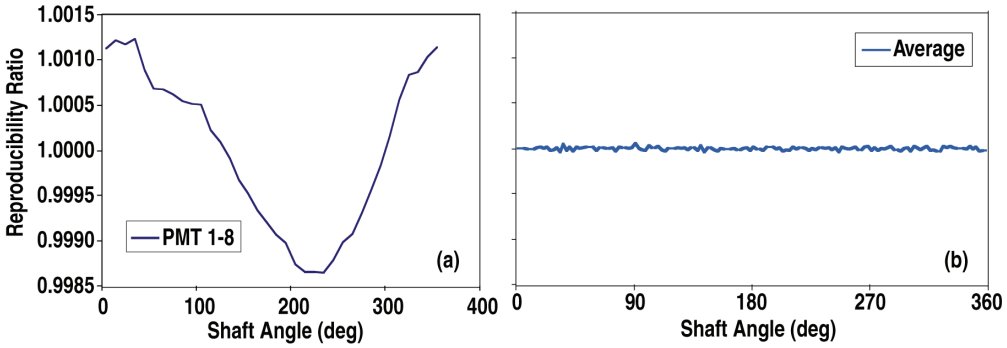

Fig. 3-15. Data initially showed that the system was unstable. With alignment with the capacitance system, we are able to get very reproducible data.

implemented a capacitive detector system that measures distances from the detector to a metal ball located on the vacuum post as the ball rotates (Fig. 3-16). It allows for alignment of the vacuum post to ~ 1 μm off the rotation axis, an order of magnitude better then what can be achieved by optical alignment. By aligning the post to this accuracy, we found that the system remained stable [Fig. 3-15(b)]. Figure 3-17 shows what a good CH shell profile looks like.

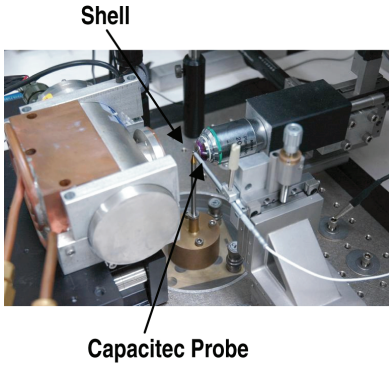

Fig. 3-16. The Capacitec system must be very close to the metal shell to give required sensitivity.

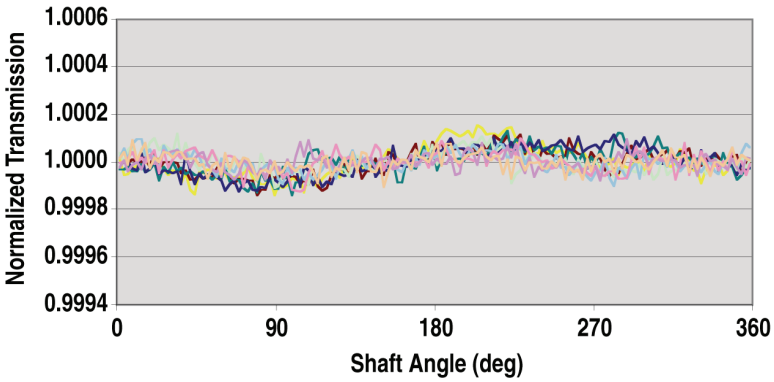

Fig. 3-17. Precision radiography trace of a good CH shell.

To get to 1 part in 10^4 takes five full days of measurement. We need to reduce measurement time to one day to meet the required throughput. Since we have optimized the optics for light collection, we need to design a system with a brighter x-ray source. To minimize blurring, we cannot increase the current significantly (spot size grows with increasing current). We have chosen to purchase a silver anode transmissive tube, which will reduce the distance from the anode to the detector to 6 mm (our old system was 36 mm away). This should increase our flux by a factor of 36 times.

The first transmission tube did not meet the specification. The flux only increased by 10 times and the blurring increased significantly due to a large x-ray spot size. We will soon be receiving the final x-ray tube.

For more information see article, "Precision X-ray Optical Depth Measurements in ICF shells" presented at the 2006 Target Fabrication Specialists' Meeting or contact Sam Eddinger.

3.6. QUANTITATIVE RADIOGRAPHY: FILM MODEL CALIBRATION AND DOPANT/IMPURITY MEASUREMENT IN ICF TARGETS — H. Huang, R.B. Stephens, A. Nikroo, S. Eddinger, K.C. Chen, H.W. Xu, K. Moreno, K.P. Youngblood (GA), M. Skelton (MIT)

Current NIF target designs are built up of variously doped layers which require the radius, the wall thickness and the wall thickness variation of each sublayer to be determined to submicron accuracy. Beryllium is optically opaque which necessitates the use of an x-ray method. We have developed the imaging equipment and analysis techniques needed to make film-based contact

x-radiography quantitative for both dimension and dopant measurements. This section updates recent progress in dopant and impurity measurement [3-23].

3.6.1. Film Model Calibration

The x-ray photon detection in the contact radiography system is highly non-linear and requires a film model to convert grayscale data into dopant or impurity information. The accuracy of the dopant model depends on our knowledge of the x-ray spectrum, its attenuation through the sample and the film response. We directly mapped the spectra of the W-anode x-ray tube with a Si-detector with the x-ray tube voltages between 4 and 30 kV at 1 kV interval, a subset of which is shown in Fig. 3-18. X-ray attenuation curve of every element in the periodic table is readily available from an on-line x-ray database that covers the photon energy range from 30 eV to 30 keV [3-24]. We then obtained the film properties (Fig. 3-19) based on its response after the x-ray spectrum passed through various thicknesses of known materials such as polypropylene. We then checked the accuracy of the film model against physical standards on all elements relevant to the NIF capsule design. We used ultra-high purity Be and BeO flats to validate the measurement of Be with oxygen content varying from 0 to 50 at. % and used a 1–6 μm thick copper step wedge to validate copper dopants in NIF capsules where 0 to 0.75 at. % copper is to be distributed along an ~1000 μm x-ray path length. The use of physical standards allows the film model to be calibrated to < 5% accuracy.

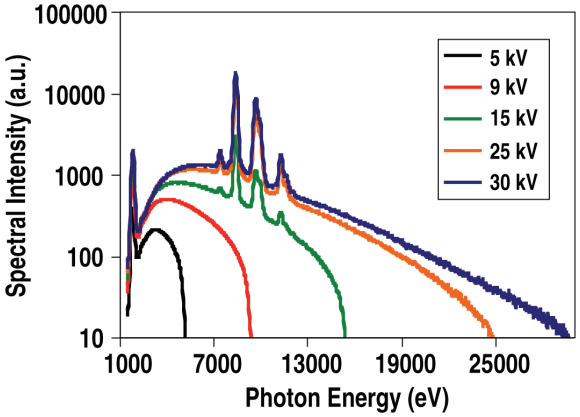

Fig. 3-18. Measured x-ray spectra from a W-anode tube operation between 4 and 30 kV.

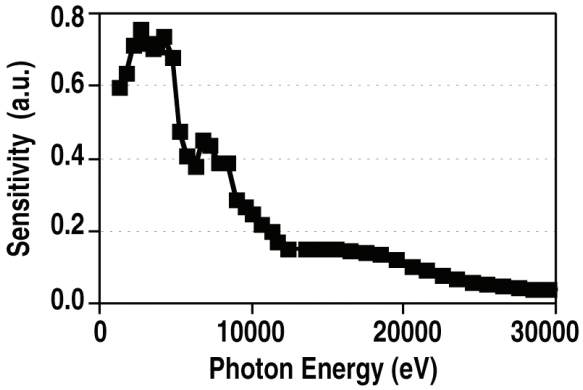

Fig. 3-19. The film response is determined empirically from experiment on step wedge standards.

The random error in dopant measurement is dominated by grayscale variations due to the film processing. A polypropylene step-wedge standard can be used to calibrate out large variations from film plate to film plate. When a higher precision is desired, a PAMS ball standard can be placed in close proximity to the sample (i.e., within the same x-ray fluorescence (XRF) holder) to calibrate out the within-the-film-plate variations. With such a procedure, contact radiography in conjunction with the film model measures the absorption level of a sample to an accuracy of ± 5% and repeatability of ± 2%. This translates into different measurement sensitivities for different elements. For example, we can measure oxygen to an accuracy of ± 0.4 at. % and copper to ± 0.02 at. %.

3.6.2. Applications

Quantitative radiography allows atomic percent of impurity elements to be evaluated on the basis of absorption increase. The new NIF impurity specification lumps oxygen with other trace elements and is given a total allowance of 30% absorption increase, which greatly simplifies production measurement. The new specification has several advantages:

1. Allows non-destructive measurement of the sample to be shot, rather than the sputtering target.
2. The measurement has the same Z^2 scaling factor as that in implosion. Therefore, what is not seen is irrelevant to the implosion performance.
3. The extremely difficult to measure oxygen profile can now be calculated to ~0.4 at. % accuracy.

The oxygen profile as a function of depth can be calculated from the shell radial profiles before and after Be shell pyrolysis [Fig. 3-20]. The average oxygen pickup can be validated by weight gain measurement, and the presence of the oxygen gradient can be validated by EDX measurement on cross-sectioned samples. The agreement between the methods is typically ~ 10% of the reported oxygen values. The non-destructive oxygen profiling capability provides valuable process development feedback.

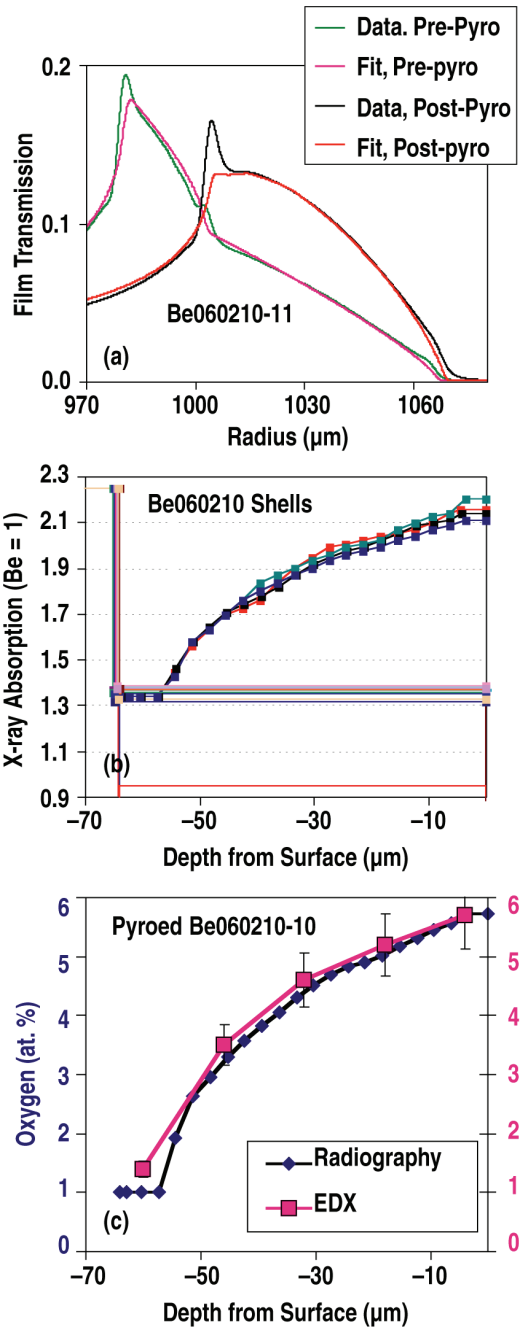

Fig. 3-20. (a) Film transmission profile. (b) X-ray absorption profile. (c) Oxygen profile. The oxygen profile (c) is determined from the absorption profile (b) which in turn is determined from the shell radial profile (a) measured from the film plate. The average oxygen increase before and after pyrolysis can be validated by weight measurement. The non-uniform distribution of oxygen can be validated by EDX measurement on cross-sectioned samples. In both cases, the agreement is with 10% of the reported values.

Summary for Section 3.6

Film-based contact radiography has matured into a production worthy tool for NIF capsule metrology. We have established a versatile film model to convert grayscale measurement on a film plate into dopant and impurity profiles to guide process development work in Be capsule fabrication.

3.7. QUANTITATIVE RADIOGRAPHY: SUBMICRON DIMENSION CALIBRATION AND ICF TARGET CHARACTERIZATION — H. Huang, R.B. Stephens, A. Nikroo, S. Eddinger, K.C. Chen, H.W. Xu, K. Moreno (GA), B. Kozioziemski (LLNL)

Current NIF target designs are built up of variously doped layers which require the radius, the wall thickness and the wall thickness variation of each sublayer to be determined to submicron accuracy. Beryllium is optically opaque which necessitates the use of an X-ray method. We have developed the imaging equipment and analysis techniques needed to make film-based contact x-radiography quantitative for both dimension and dopant measurements. This section updates recent progress in dimension measurement, including the error mechanisms and the mitigation method in order to achieve sub-micron accuracy.

3.7.1. Error Mechanisms in Dimension Measurement

Contact radiography is sometimes referred to as X-ray shadowgraphy, which implies that the x-ray photons travel in straight rays and that the shadow resembles the 3D objects in two dimensions. Both assumptions fail at a submicron level. There are three effects that cause discrepancy between the shadow image and the shell itself: (1) projection magnification, (2) tilted projection, and (3) phase contrast. The point projection geometry magnifies the shell diameter by ~ 2 μm for NIF sized shells, whereas tilted projection elongates the shadow in the radial direction from the film plate center. In our apparatus with a source-detector distance L ~1 m, a 40 mm offset R leads to a 1.7 μm elongation. The effect goes up with R^2 therefore it is only noticeable when the shell is far from the film plate center. For both projection magnification and tilting, the effects are proportional to the dimension measured. Consequentially, they affect the shell shape and diameter values, but do not measurably affect the wall thickness values. Phase contrast, on the other hand, disproportionally affects the wall thickness measurement.

3.7.2. Fresnel Modeling of Phase Contrast Effect

Differential phase delay when x-ray photons propagate on either side of an interface between two dissimilar materials leads to greatly enhanced interface contrast; the phenomenon is known as phase contrast. Phase contrast affects dimension measurement in two different ways: (1) it shifts the apparent positions of the interface, and (2) it blurs up the interface structure to make a precise determination difficult.

Phase contrast can be quantitatively modeled based on Fresnel propagation of the x-ray radiation [3-25–3-30]. We conducted a polychromatic simulation using a Fresnel model previously validated in the study of cryogenic ice layers. Figure 3-21 is the radial profile of an ideal case where we have assumed virtually no penumbra blurring and a detector with near infinite resolution. We then take into account real-life effects such as (1) x-ray source blurring, (2) microscope objective lens transfer function, (3) CCD pixel size, (4) film exposure etc.; which lead to simulated shell radial profiles that

are broadened from the ideal case [Fig. 3-22(a)]. The second derivative curves highlight the surfaces/interfaces and allow the locations to be measured to ± 0.2 μm precision [Fig. 3-22(b)].

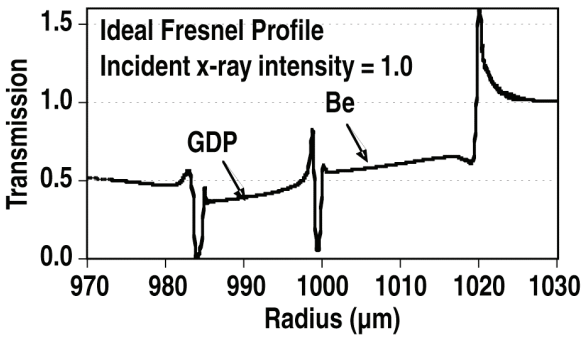

Fig. 3-21. The radial profile of x-ray transmission intensity through a 20 μm CH mandrel with 15 μm Be coating. Sharp spikes in transmission intensity at the interfaces are the hallmark of phase contrast. Note the intensity just outside the shell is more than 100% transmission due to diffraction effects.

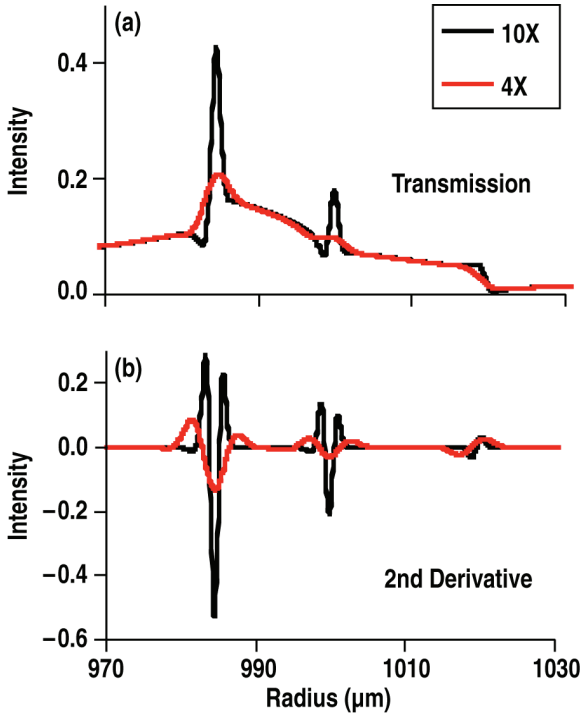

Fig. 3-22. (a) Transmission radial profile. (b) Second derivative of the transmission radial profile. Simulated radial transmission profile and the second derivative profile of a 15 μm CH mandrel coated with 20 μm Be. The second derivative highlights the surfaces/interfaces and makes it easier to identify their locations.

A systematic study of various types of Be/CH shells allowed us to obtain calibration factors to make the measurement accurate by constructing a simple look-up table to correct the phase contrast offsets in dimension measurement. We found that, to an accuracy of ~ ± 0.1 μm, the phase contrast offset does not change with Be coating thickness nor does it change with the oxygen contamination level that occurs during CH pyrolysis. The exterior and interior surfaces of Be and CH shells also behave similarly.

3.7.3. Validation

Radiography measurement, corrected for the effects described in the previous sections, provide dimension measurement accuracy well below 1 μm. An accuracy of ± 0.1 μm in the wall thickness variation profile was validated by our wallmapper system on CH shells (Fig. 3-23). An accuracy of ± 0.5 μm in diameter measurement and of < ± 0.2 μm in out-of-round (OOR) were validated on NIST-traceable Cr-steel balls. The ability of the contact radiography method to measure shell wall sublayer interfaces and the interior surfaces is invaluable to the ICF program. The capability was neatly demonstrated on CH shells (for UR/LLE) with mode-5 micro-machined patterns transferred to the interior surface (Fig. 3-24).

Conclusions for Section 3.7

Lens distortion, projection magnification, tilted projection and phase contrast are the major error mechanisms in radiographic-based dimension measurement. With proper calibration, radiography is capable of characterizing ICF

capsule dimensions with sub-micron accuracy. Specifically, the diameter can be measured to ± 0.5 μm, the shape can be measured to ± 0.2 μm, the wall thickness can be measured to ± 0.3 μm, and the wall thickness variation can be measured to ± 0.1 μm.

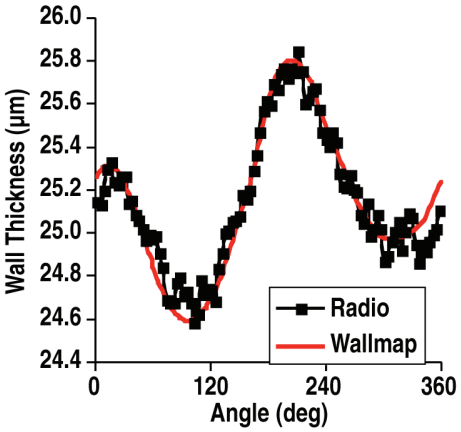

Fig. 3-23. Radiography measurement agrees with wallmapper measurement for CH shell wall thickness profile.

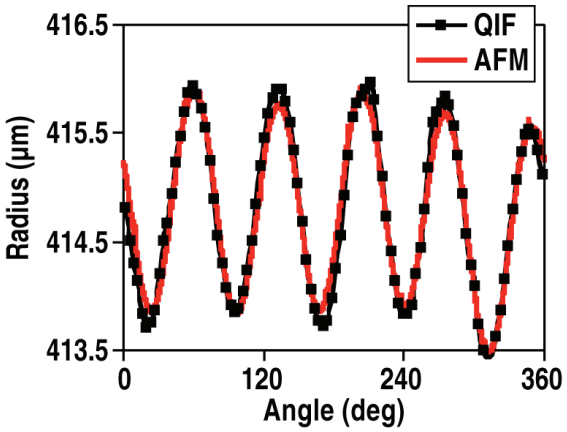

Fig. 3-24. Radiographic analysis of a "Mode 5" CH shell highlights the method's capability in measuring the interior surface shape.

3.8. UPDATE ON DEVELOPMENT OF DEPLETED URANIUM AND GOLD COCKTAIL HOHLRAUMS — H. Wilkens, D. Wall, J. Wall, A. Nikroo (GA), N. Hein (UCSD)

Fusion ignition experiments at the NIF are planned to begin with the indirect drive configuration. Although the x-ray drive symmetry is maximized in this configuration, energy is lost in the conversion process due to x-ray penetration into the hohlraum wall. To minimize this loss, high-Z material is incorporated into the traditional gold hohlraum to increase the efficiency of the laser to x-ray energy conversion by making the wall more opaque to the x-rays. Higher opacity translates to more x-ray re-emission, providing an energy margin for ignition on NIF.

The current specifications, outlined in the "Rev1" table of requirements for NIF ignition point design released from LLNL in September, 2006, state that the 5.1 mm diameter hohlraum can be comprised of at least a 7 μm-thick "cocktail" layer, composed of 75 at. % depleted uranium, 25 at. % gold, with the requirement of < 5 at. % oxygen in the bulk. The gold layer lining the hohlraum interior, which is needed to protect the U from oxidation, can be no more than 0.5 μm thick, and the thick gold capping layer on the exterior of the hohlraum must be >10 μm. This outer gold capping layer works to protect the depleted uranium from corrosion and gives the hohlraum the structural integrity required for target assembly and subsequent handling.

Three major production steps define the cocktail hohlraum fabrication process: coating cocktail material onto a mold, etching the mold without damaging the coating, and protecting the depleted uranium in the free-standing hohlraum from oxidation. The success of the later process sets the shelf-life. A cartoon of the production steps is shown in Fig. 3-25.

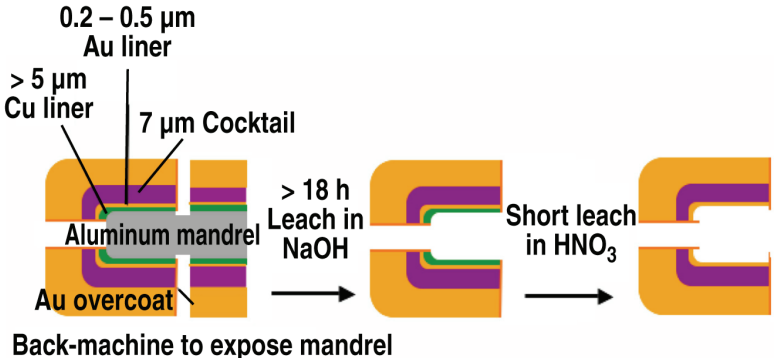

Fig. 3-25. Description of current fabrication process of cocktail hohlraums. Starting with a Cu-lined Al mandrel, the Au liner is electroplated then the cocktail multi-layers are sputtered onto the metal mold. After gold is sputtered then electroplated over the cocktail multi-layers, the mandrel is back-machined to expose the underlying Al mandrel. The exposed edges are then sealed in electroplated Au, after which the Al mandrel is leached in sodium hydroxide. Finally, the thin Cu liner is removed in nitric acid, leaving a free-standing cocktail hohlraum.

In the coating step, multi-layers of depleted uranium and gold are sputtered onto a metal half-hohlraum-shaped mold, or mandrel, by indexing the rotating mandrel in front of separate DU and Au sources. The challenge of the coating step is to produce low-stress cocktail coatings, which is now done with a > 90% yield on metal mandrels. The outer structural layer of gold is done by electroplating. The material is back-machined away at the laser entry hole and back edge both to define the final shape of the hohlraum, as well as to expose the underlying mandrel to the etchant chemicals. The exposed cocktail is sealed in electroplated gold before the etching steps.

Etching out the mandrel to leave an intact hohlraum half has proved to be difficult in practice. The etchant chemicals attack the depleted uranium, causing oxidation that is unacceptable for two reasons. First, from a fabrication point of view, the DU lattice expands significantly during oxidation, which results in severe structural damage to the hohlraum. Second, from a target physics consideration, the presence of oxygen increases the ionization heat capacity of the hohlraum wall, effectively canceling the efficiency gains associated with incorporating DU into a Au hohlraum. The solution to the etching problem has been to incorporate a hybrid mandrel made of aluminum coated with a thin (~5 μm) copper liner. The copper liner protects the cocktail during the > 18 h etch in NaOH to remove the aluminum mandrel. The copper liner is then removed in nitric acid, typically in less than 5 minutes, which minimizes the time that the uranium is exposed to the harmful etchant. The yield of free-standing cocktail hohlraums is currently 40%, though some parts still suffer minimal oxidation damage. Experiments are ongoing to increase this yield.

Within hours to days of a successful etch, it is observed that the 0.5 μm thick electroplated gold liner starts to crack along the interior of the hohlraum barrel. The shelf-life is qualitatively defined by the appearance of these cracks since once they appear, irreparable damage to the DU via oxidation is inevitable. Cracking is initially induced by corrosion of the depleted uranium by nitric acid.

Reducing the exposure time limits the amount of time that the harmful etchant has to seep into micro-pores or pinholes in the Au liner, or into breaks in the electroplated seal at the back-machined edges. This is the reason that the yield has increased from 0% to 40% with the use of the thin copper liner over the Al mandrel as compared to a long etch of a full copper mandrel. Experimental results using transmission electron microscopy, done in collaboration with Jason Cooley at LANL, show that the Au liner is not inherently porous, but this work does not rule out micro-pores caused by contaminants such as dust. The lab space in which the cocktail hohlraums are produced is being converted to a Class 10,000 clean room to mitigate this possibility. Collaborative work is also under way with Suhas Bhandarkar, Evan Mapoles, and Jeff Atherton at LLNL to quantitatively understand how internal stresses in the films, induced thermally and during sputter deposition, can be balanced to improve the structural integrity of the cocktail hohlraums.

The fabrication of a full NIF-scale hohlraum half has been demonstrated, meeting the NIF specifications for dimensions, composition, Au liner thickness and low oxygen content (Fig. 3-26). The first demonstration, made in April 2006, fulfilled the level 3 DOE reporting milestone due the middle of May 2006. The shelf life of the hohlraum halves, currently on the order of several days, will have to be improved to meet the target fabrication requirements for NIF. The minimum targeted shelf-life is on the order of 6 weeks since this is approximately the amount of time that will be required to assemble the full NIF target package. Once the cocktail hohlraum shelf-life is improved, the qualitative definition of the shelf-life currently used will be replaced with a quantitative analysis of the cocktail multi-layers by Auger electron depth-profiling spectroscopy, which allows for the composition to be measured as a function of depth into the multi-layers. The maximum oxygen composition of 5 at. % allowed by the NIF specifications will then be the defining metric.

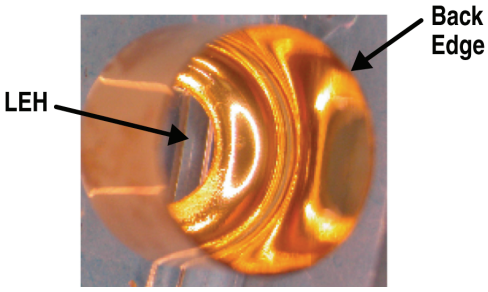

Fig. 3-26. A photographic image of a pristine, free-standing cocktail hohlraum half is shown after the final etching step. This hohlraum half has an inner diameter of 5.1 mm.

Due to the installation of a second GA-designed and built sputter deposition system, work to fabricate OMEGA-scale cocktail hohlraums continues in parallel with the NIF-scale experiments outlined above. The procurement of a micro-machining lathe dedicated to the cocktail hohlraum work has further increased our research and development progress.

3.9. REDUCTION OF ISOLATED DEFECTS ON Ge-DOPED CH CAPSULES TO BELOW IGNITION SPECIFICATIONS — K.C. Chen, Y.T. Lee, H. Huang, J. Gibson, A. Nikroo (GA), M.A. Johnson, E. Mapoles (LLNL)

We demonstrated control of Ge doping levels, layer thickness and met the inner wall smoothness in CH capsules in a previous report [3-31]. The goal this year was to meet all CH capsule specifications. We focused on the isolated feature specification since it is the only major specification

remaining to be demonstrated. The isolated feature specification, shown in Fig. 3-27, defines the permissible number and dimensions of large isolated surface defects over the entire capsule surface in three regions [3-32]. The capsules cannot have any isolated feature with a size above the top region in Fig. 3-27 to ensure the final perturbation on the fuel is small at peak velocity.

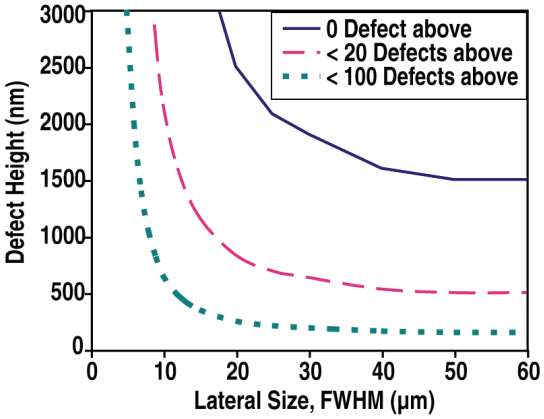

Fig. 3-27. The NIF isolated feature specification defines the allowed number and dimensions of isolated defect features.

To date, thick-walled capsules often have a few large isolated domes that render the capsule out of the isolated feature specification. These large domes have been attributed to various origins, including surface chemistry and microscopic defects on the mandrel, abrasion damage from mechanical agitation, and deposition parameters [3-33–3-36]. Methods of in-process and post-process polishing to eliminate isolated domes are being tried [3-37,3-38]. We observed that some large domes have distinct dark-colored origins which indicated possible particulate contamination. The particulate contamination inside the coater chamber was investigated.

3.9.1. Experiments

We examined movable items inside the coater chamber as potential particulate contamination sources including: (1) plasma tube changes, (2) assembling the upper and lower coater chambers, (3) pan screw attachment, and (4) motions resulting from solenoid tapping that is needed for capsule agitation. Freshly cleaved smooth mica pieces (2.5 × 2.5 cm) were used as mandrel surrogates for particulate contamination studies to eliminate the uncertainty of whether the dome source is from the mandrel. The central 1 cm^2 areas of mica pieces were scanned for large domes with a WYKO interferometer.

A rotation setup with a 10 deg tilt pan was specifically built without a tapper to coat NIF capsules. The layer thicknesses, Ge doping levels, and wall uniformity were measured from quantitative contact radiographs, as described before [3-23,3-31]. The isolated defects on the CH capsules were characterized with an AFM spheremapper and the spherical phase-shifting diffractive interferometer (PSDI) developed at LLNL [3-39,3-40]. A threshold of 50 nm was chosen so that only dome heights larger than 50 nm were counted. Equatorial bands of several capsules from three coating runs were first measured and then hemisphere measurements were carried out as a precision positioning device became available.

3.9.2. Results

Identification of Particulate Contamination Sources from Mica Experiments. The results of particulate contamination studies using mica substrates are shown in Table 3-1. From left to right, the

first and the second experiments were done without energizing the tapping solenoid. All experiments had two plasma tube changes. A 20 μm CH layer was deposited after each tube change to grow the particulates into visible domes. The first experiment paid little attention to the tube insertion practice. The second experiment was done by carefully inserting freshly cleaned plasma tubes, plus it included a 2-h coating run to anchor any imperceptible particulates before a mica piece was introduced.

Table 3-1
Mica Experiments

40 h Coating Unless Noted	**Tapper Turned OFF**		**Tapper Turned ON**		**Tapper Covered**
Mica experiment	Regular tube change	+ 2 h pre-coat	+ 2 h pre-coat	+ 2 h pre-coat + 88 h	+ 2 h pre-coat
Run 1	12	4	17	37	1
Run 2	10	6	22		0
Run 3	9				0
Average domes =	10	5	20	37	1

The next two experiments tested the effect of solenoid tapping. Both tapper-on experiments have more domes than the tapper-off experiments. The dome count roughly doubled in an 88-h run as compared to a 40-h run. These two experiments clearly revealed the tapping solenoid was a particulate contamination source. The last experiment had the tapper covered and the dome count was drastically reduced. Comparing the results of the second and the fifth experiments, we concluded that the solenoid tapper, even without being energized, contributed particulates into the coating chamber during the vacuum pump down. The particulates are from the wear of the barrel liner against the plunger (Fig. 3-28). The particulate size ranges from tens of nanometers to tens of micrometers. The particulate is plastic in nature. From the radiograph images, we did not see evidence of any metallic particulates from the pan screw attachment.

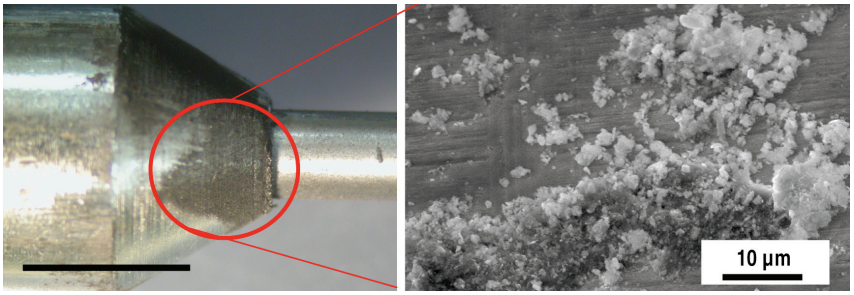

Fig. 3-28. Particulate stain on solenoid plunger from the wear of the solenoid (a). The SEM micrograph shows the particulate size ranges from nanometers to micrometers (b).

Reduction of isolated defects of germanium-doped capsules using rolling. We used the rotation agitation setup (without tapper) to coat the capsules. The optical photograph of the capsules clearly

shows the reduction of large domes when the tapping solenoid was removed as compared to the photo of tapped capsule to the left [Fig. 3-29(a)]. The AFM power spectra are below the NIF surface modal power spectrum standard and RMS values of high modes (>11) are in the range of 3–6 nm [Fig. 3-29(b)].

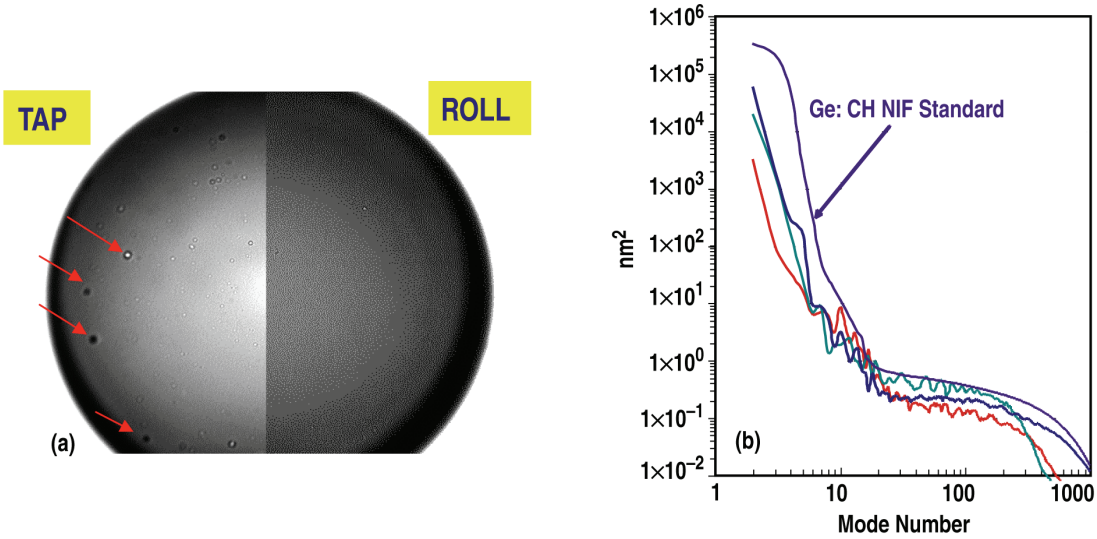

Fig. 3-29. (a) NIF-thickness capsules coated using tapping agitation (left) and rolling agitation (right). The rolled capsule shows reduction of large domes. (b) Three average AFM power spectra of three NIF-thickness rolled capsules.

Conclusions for Section 3.9

Large domes on capsule surfaces originated from particulate contamination from the wear of a tapping solenoid used to agitate the capsules. When the tapping solenoid was removed and a new rotation agitation setup was used, full thickness NIF capsules were produced having fewer isolated defects and meeting the power spectra standard.

Several batches of Ge-doped CH capsules made by rolling agitation met the NIF layer thicknesses, Ge-doping levels, and total wall thickness specifications. The number and size of the isolated defects on the surface of the rolled capsules, characterized with spherical phase-shifting diffractive interferometry, also met the NIF isolated defect specification.

NIC X-RAY DRIVE TARGET PRODUCTION

3.10. DETERMINISTIC FABRICATION AND CHARACTERIZATION OF FILL TUBE SURROGATE TARGETS FOR OMEGA EXPERIMENTS USING A POLYMER STALK — A.Q.L. Nguyen, E.L. Alfonso, D.G. Czechowicz (GA)

Fill tubes, or stalks, on capsules are needed for implosion experiments on OMEGA to study how the size of a fill tube perturbation affects implosion symmetry. We fabricated stalks composed of a low-Z plastic with hydrodynamic properties similar to a fill tube and attached them to ~ 500 μm diameter polymer capsules, scaled to ignition designs for NIF [3-41]. The capsules had an inner Ti-doped layer for the purpose of imaging the x-rays expected from the hydrodynamic jet produced by the stalk [3-42,3-43]. Stalk diameters needed ranged from 10 to 30 μm with corresponding fillet diameters and lengths indicated in Table 3-2. A deterministic fabrication technique was developed to control process parameters and produce stalks within specifications.

Table 3-2
Specifications Required for a Series of Surrogate Fill Tube Targets

Fillet Diameter	Stalk Diameter	Length
25 ± 5 μm	10 ± 3 μm	100 ± 20 μm
37 ± 7 μm	17 ± 3 μm	100 ± 20 μm
50 ± 5 μm	25 ± 3 μm	100 ± 20 μm
60 ± 5 μm	30 ± 3 μm	100 ± 20 μm
Offset angle of stalk: Surface normal ± 3 deg		

3.10.1. Experimental

In our initial attempts to make stalks, we melted PAMS crystals on a heated gold-coated glass slide. We held a capsule with a vacuum chuck and touched it to the melted PAMS to draw a fiber that solidified upon cooling [3-44]. Achieving uniform and reproducible results was difficult because of the inconsistent molten PAMS source and the need for constant realignment of capsule and polymer. Consequently, the yield was less than 20% for the first required fillet diameters of 25 μm.

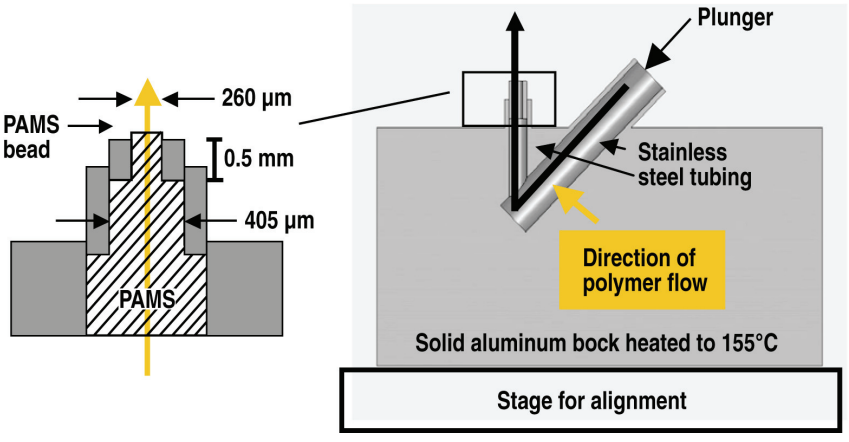

Fig. 3-30. Cross sectional view of polymer reservoir. The PAMS bead replaced the polymer melt on the glass slide.

A heated reservoir was designed to produce a controlled polymer supply. Figure 3-30 shows a cross sectional view of the reservoir. Stainless steel tubing was inserted and soldered into a solid aluminum cylinder in contact with a heated aluminum block mounted on a micrometer controlled stage. PAMS crystals

were inserted into the system through the larger tube and, upon melting, were displaced with a plunger forming a polymer bead at the opening of the smaller tube.

The selection of the PAMS molecular weight (MW) was important in fabricating stalks for two reasons. First, MW is related to viscosity that affects taper control and uniform spreading of the fillet. When the melted polymer is too fluid, the stalk suffers from excessive tapering and does not solidify completely as it tapers causing the stalk to curl when pulled away from the molten PAMS bead. Second, different MW PAMS have different melt temperatures and strength. We found that stalks made with PAMS having MW < 4000 were too fragile, whereas stalks made with MW > 4000 required melt temperatures $\geq 200°C$ that would deform the CH capsule. Ultimately, 4000 MW PAMS was found to be most suitable at 155°C.

We also developed a precision assembly station with a high-resolution viewing system. A schematic of the viewing system in Fig. 3-31 shows an overlaid grid on the monitor with 5 μm increments that define the resolution when the capsule and bead are viewed at highest magnification. The monitor and XYZ-stage manipulator are used to orient the capsule normal to the PAMS bead. To make the stalk, the capsule is dipped into the reservoir of molten PAMS. Fillet diameters are controlled by the depth of the capsules as they are dipped into the reservoir, whereas taper and stalk diameters are controlled by the pulling rate.

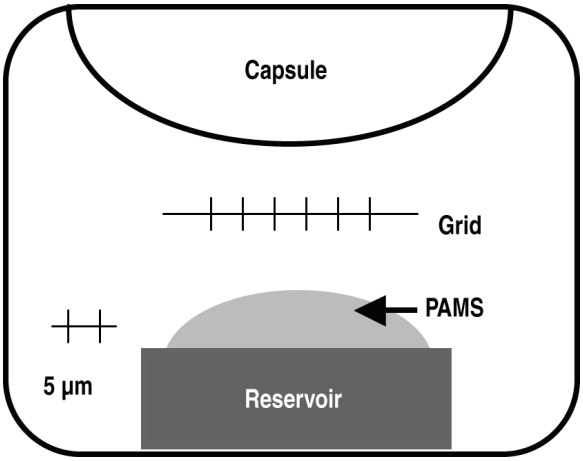

Fig. 3-31. Schematic of stalk pulling viewing system. Capsule is brought into view over the polymer bead. Fillet diameter and stalk diameter are determined using the overlaid grid.

After the stalk is made, it is cut to length using a special capsule holder and blade assembly. A well was machined into an aluminum SEM mount to hold the capsule securely during cutting. A hole was drilled at the base of the well through which a vacuum could be drawn to hold the shell as illustrated in Fig. 3-32. The capsule and mount were transferred to a non-vacuum holder on the assembly and viewing station. In addition, an OASIS® feather blade was substituted into the micromanipulator. The stalk was laid flat with the blade positioned directly over the

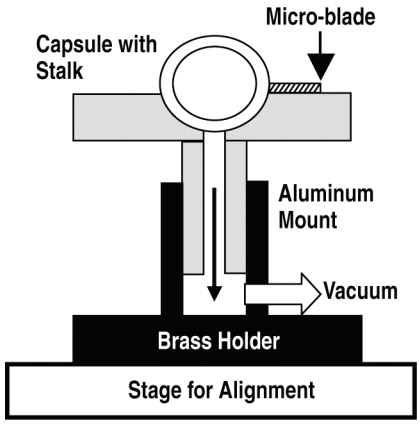

Fig. 3-32. Mount fitted into vacuum holder to secure capsule for stalk cutting. The microblade was controlled with the XYZ-axis micromanipulator used for stalk pulling.

fillet; translated 100 μm with the digital micrometer stage; and then cut with the blade to within ± 10 μm of the desired length.

After trimming the stalk, the capsule was mounted onto Gel-Pak® and positioned so that the stalk was viewable by the measuring microscope and normal to the capsule surface. To confirm the uniformity of the fillet and stalk, and to measure any angle in the stalk tip resulting from cutting, the capsule was rotated 90 deg for additional measurements and 45 deg upwards for imaging.

Conclusion for Section 3.10

A deterministic technique to fabricate polymer stalks was developed and used to successfully produce a series of surrogate fill tube targets for hydrodynamic studies at OMEGA. The polymer reservoir and pulling technique increased the yield of in-spec surrogate fill tube targets from 20% to greater than 75%. OMEGA experimental results indicated that a stalk diameter of less than 10 μm did not affect the implosion [3-45]. The heated reservoir and polymer pulling techniques were also adapted for fabricating monolithic fill tube (MFT) targets [3-46]. We implemented improvements and achieved an accuracy of ± 3 μm for the stalk length using Excimer laser cutting.

3.11. FABRICATION AND CHARACTERIZATION OF BERYLLIUM RAYLEIGH-TAYLOR TARGETS FOR OMEGA EXPERIMENTS — K.A. Moreno, H.W. Xu, A. Nikroo, H. Huang, J.E. Knipping, J. Kaae, E. Giraldez (GA), J. Fong (UCSD)

One of the targets for ignition at the NIF uses a graded copper-doped Be capsule (Fig. 3-33) [3-41,3-47]. A rippled flat target containing a mixture of Be and copper is used to measure Rayleigh-Taylor instability in ICF experiments. The perturbations of a flat are relatively easy to characterize. The specifications of the flats are shown in Table 3-3.

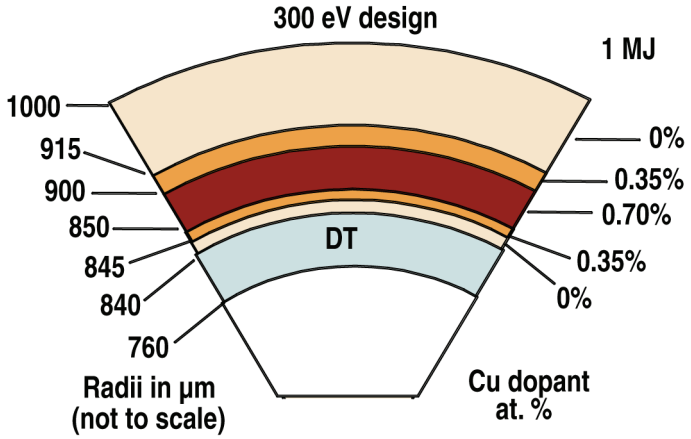

Fig. 3-33. The NIF specification of the graded copper doped, 2 mm o.d. × 160 μm wall, Be capsule. The chemical composition of the layers is shown above [3-47].

Table 3-3
Specifications and Characterization Techniques
of the Be Rayleigh-Taylor Flats

	Characteristic	Specification	Characterization Technique
A	Thickness	4–50 ± 5 μm, flat to ≤ 1 μm	Interferometric microscopy
B	Morphology	Similar to Be shells	Scanning electron microscopy of cross section
C	Wavelength	50 ± 1 μm	Interferometric microscopy
D	Amplitude	0.25 ± 0.03 μm	Interferometric microscopy
E	No ripple side, surface finish	< 200 nm rms	Interferometric microscopy
F	Chemical Composition	Be doped with 2–3 at. % Cu, measured to ±10%	X-ray fluorescence and contact radiography
G	Density	Known to within < 3%	Correlation of Cu at. % with known samples, floating

3.11.1. Fabrication of the Flats

We coated the Be onto aluminum or copper molds with machined features having the required wavelength and amplitude as shown in Fig. 3-34.

While developing the process, it became clear that aluminum would be a more reliable substrate, as the difference in the coefficient of thermal expansion (CTE) between Be (11.3) and copper (16.5), proved to be too great [3-9]. Subsequent delamination due to CTE mismatch made it impossible to polish uniformly or get an accurate starting thickness. Also, the nitric acid, which is used to etch the copper substrate, posed a threat to the copper in the Be-RT flat.

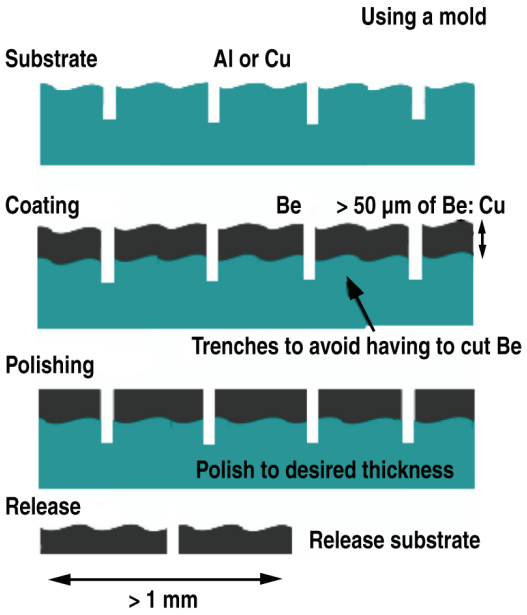

Fig. 3-34. Mold technique: (1) Begin with a substrate machined with the required ripples, (2) overcoat with Be and Cu, (3) polish to required thickness, and (4) release Be:Cu flats by etching away substrate.

The sputter deposition included three Be sources and one copper source [3-9]. The copper source was moved closer than it is typically positioned when fabricating the NIF specification capsules to obtain the higher Cu at. % that was required for this experiment. The substrate with 60–70 μm of Be:Cu was polished down to the required thicknesses. The free-standing Be rippled flats were then characterized to verify that the specifications outlined in Table 3-3 were met.

3.11.2. Characterization of the Flats

(A) Thickness. White light interferometry was used to accurately (± 0.2 μm) measure the thickness of each Be rippled flat using a tripod technique [3-48]. The high opacity of the Be flat obviates optical transmission diagnostics.

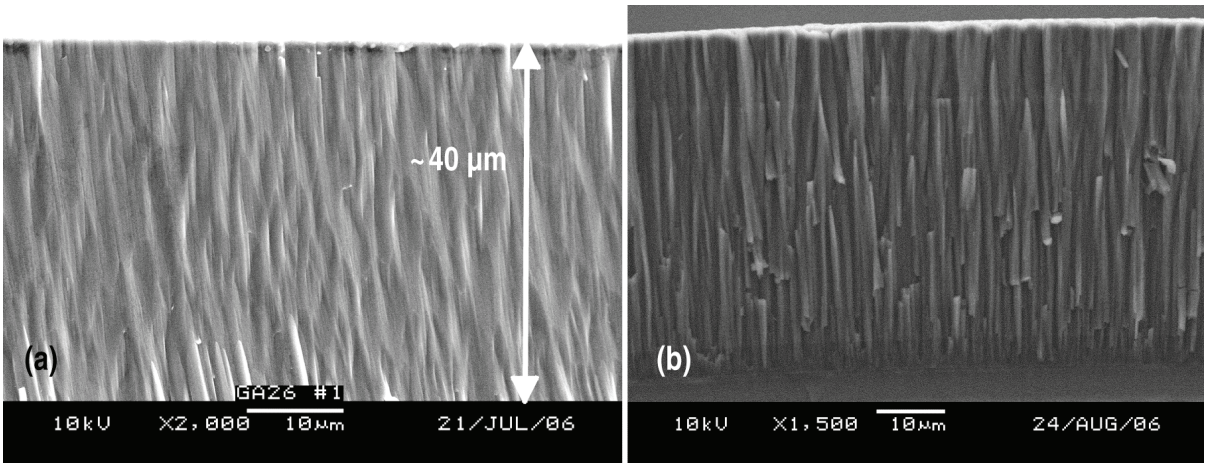

Fig. 3-35. (a) An SEM image of the cross section of Be rippled flat after breaking. (b) An SEM image of a cross section of a NIF spec shell after breaking.

(B) Morphology. In order for the Raleigh-Taylor experiment to be relevant, the grain structure of the flat needed to be similar to that in a NIF ignition capsule. In these capsules, a columnar grain structure is observed by SEM [3-48]. A very similar grain structure was seen in the SEM image of the Be rippled flat and the NIF ignition capsules, as shown in Fig. 3-35.

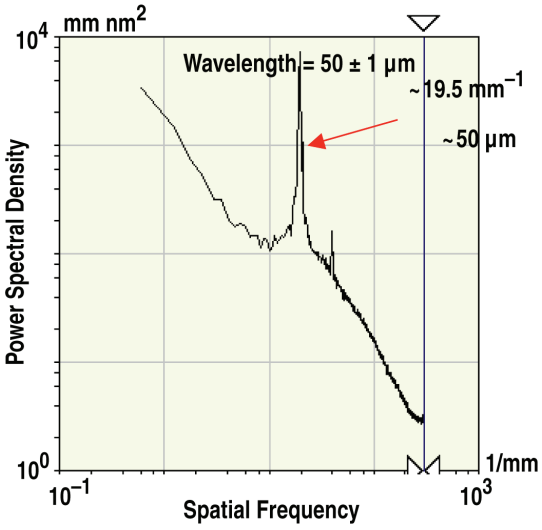

Fig. 3-36. Spatial frequency of a typical wavelength (50 μm) seen in a Be Rayleigh Taylor flat.

(C) Wavelength/Amplitude and (D) Non-Rippled Side Surface Finish. A WYKO surface profiler was used to measure the wavelength and amplitude of the ripple pattern in the surface of the free-standing flat. The wavelength measured on the rippled side is 50 ± 0.2 μm, as shown in Fig. 3-36. The surface finish of the non-rippled surface was measured to be between 140-180 nm, well within specification.

(E) Copper Atomic Percent. Each individual flat was analyzed for Cu concentration using XRF and quantitative contact radiography [3-23,3-49]. The copper atomic percent ranged from 1.5-3.0. The two methods agreed to within 10%, which met the specification for the accuracy of the copper atomic

percent. This variation in the copper atomic percent is believed to be due to the positioning of the substrate during coating.

(F) Density of Sample. In order to determine the densities of our samples, a comparison was made with Be copper standards [3-50]. The density of these standards was measured by adjusting mixtures of dibromopropane and carbon tetrachloride until the standards were neutrally buoyant in the mixtures. Once the proper mixtures were found, the solutions were analyzed with a densitometer to determine the densities. We used the copper atomic percent measured by XRF to compare our samples with the standards to determine the densities. These densities were verified by floating surrogate flats in the same manner as the standards and agreed to within 5%.

Conclusion for Section 3.11

Rippled copper-doped Be flats were successfully fabricated and characterized for Rayleigh-Taylor experiments on the OMEGA laser. A mold was used to form the required ripple on one side and to produce the proper sized free-standing flat. Beryllium and copper were co-sputtered to obtain the required chemical composition. This sputtered material was then polished down to the appropriate thickness and released by etching away the mold. The free-standing flats were then characterized to verify that they met the specifications required by the Rayleigh-Taylor experiment. All of the specifications were met except for the amplitude of the rippled side, which could have been adjusted by the machining of the mold.

3.12. INVESTIGATIONS TO REMOVE DOMES FROM PLASTIC SHELLS BY POLISHING — D. Czechowicz, D. Steinman, E. Castillo (GA), C. Chen (UCSD), J. Dorman (UCLA)

A problem often observed for thick wall plastic ICF capsules is the presence of surface domes formed during the fabrication process. These domes can adversely affect target performance and thereby compromise ICF experiments. We have been successful in applying mechanical polishing to remove isolated surface domes from thick wall (~ 50 μm) 2 mm GDP shells during a preliminary investigation.

3.12.1. Experimental

A counter-rotating lap polisher similar in design to the device used for polishing Be capsules [3-51] was used in our work to remove domes from GDP shells. The shells were polished using diamond polishing paper of 0.1, 0.5 and 1 μm grit size.

The background surface roughness for the polished shells was dramatically improved with final values typically around 10 nm RMS as measured by WYKO surface profiles. Figure 3-37 presents our three-step polishing sequence showing the removal of a large 100 μm wide × 5 μm tall identifiable dome found on a 2 mm GDP shell. The surface profiles of Fig. 3-37 correspond to (a) the pre-polish dome shape, (b) the first polish dome shape, (c) the second polish dome shape, and (d) the third polish dome shape.

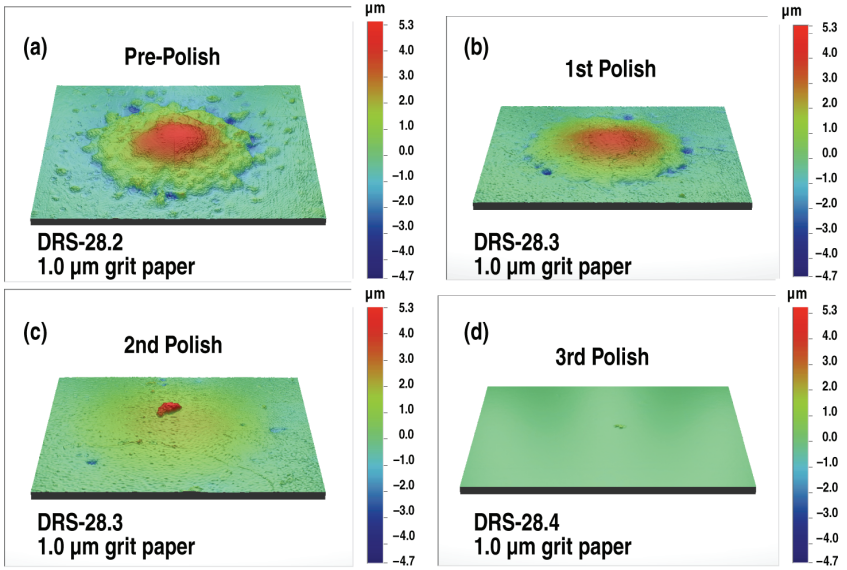

Fig. 3-37. WYKO surface profile data showing removal of identifiable GDP dome after three polishing runs.

Figure 3-38 shows plots of the dome height, dome diameter, and background surface roughness for the pre-polish surface profile and for the profiles after each successive polishing step. Observed is the complete removal of the large dome and a decrease in background surface roughness to a final value of < 10 nm RMS.

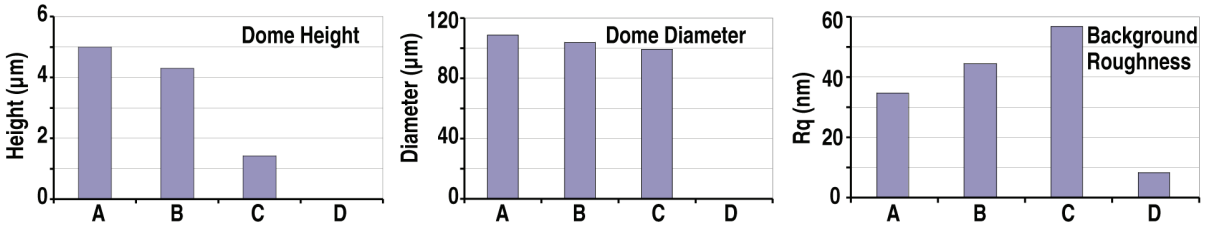

Fig. 3-38. Characterization values for dome height, dome diameter, and background roughness during removal of identifiable dome.

A polishing sequence was also examined using AFM spheremap data for a similar 2 mm GDP shell after three successive polishing steps. Power spectra for the pre-polished shell and after each successive polishing step are presented in Fig. 3-39.

Presented in Fig. 3-40 are changes observed in surface modes as a function of polishing time for the shell. The data indicates that a two-step polishing approach was able to produce a significant improvement in the power spectrum above mode 10. A third polishing step for this shell showed no further improvement in surface modes and an actual increase in values for modes less than 10.

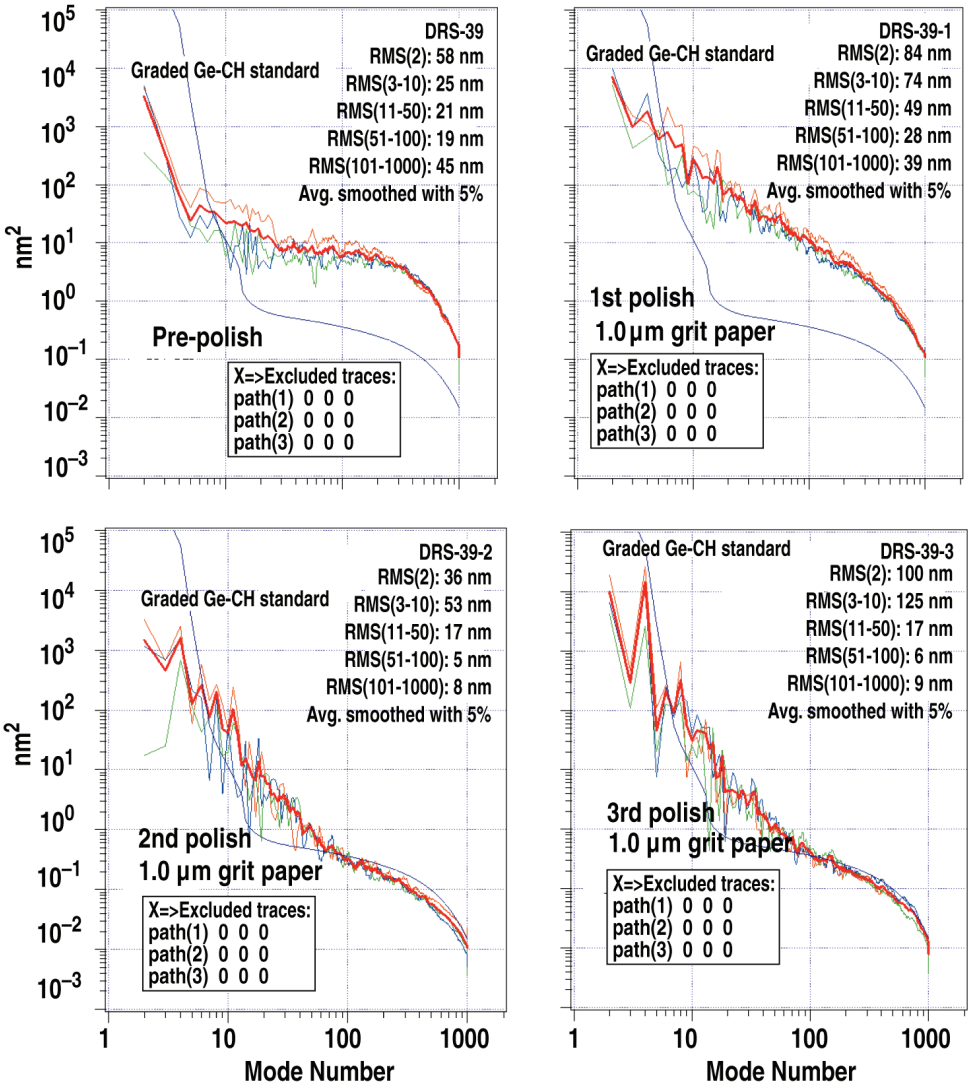

Fig. 3-39. AFM power spectrum for same 2 mm GDP shell before and after three successive polishing steps.

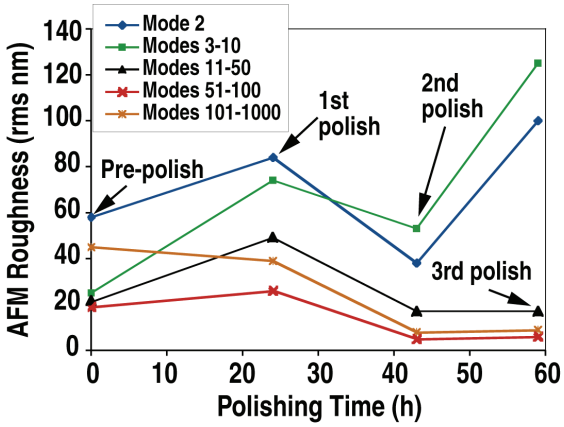

Fig. 3-40. Changes observed in power modes as a function of polishing time for the same 2 mm GDP shell.

Conclusions for Section 3.12

Our investigation demonstrated that mechanical polishing removes domes from GDP shells. Based on preliminary spheremap data, further polishing development is needed to reduce AFM low and mid-power modes for shells. Polishing of otherwise target quality GDP shells that have domes could be a future treatment for NIF capsules, particularly for shells with large isolated surface features.

3.13. NEW DEVELOPMENTS IN Si-GDP TO GLASS SHELLS — RESIDUAL GASES, GAS FILLING AND TAILORED HALF-LIVES — M.L. Hoppe, D.A. Steinman (GA)

The method for producing glass shells from Si-GDP has been presented previously [3-52,3-53]. Recent advances in making glass shells by this process include: ability to fill shells with a noble gas; adjusting permeability to better meet desired target characteristics; and a reduction in trapped residual gases and carbon generated during the conversion of the Si-GDP to glass.

3.13.1. Experimental

All beginning PAMS shell mandrels were made by microencapsulation [3-54]. The PAMS shells were roll coated in a plasma polymerization system based on a helical resonator and piezo bouncer described by previous authors [3-36]. Tetramethyl silane (TMS), trans-2-butene (T_2B) and hydrogen were used as feed-stock gases for the plasma coater. The PAMS mandrel was removed after the Si-GDP coating step was completed in a controlled heating process in which the temperature was slowly ramped to 300°C under nitrogen (or Ar) to decompose and volatilize the PAMS polymer.

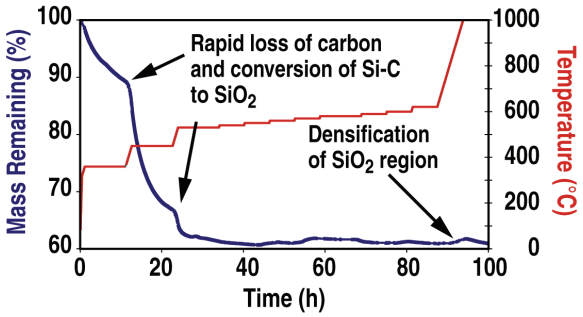

Fig. 3-41. TGA shows the percent mass remaining as a function of time and temperature during the conversion of Si-GDP to glass.

TGA of the conversion of the Si-GDP to SiO_2 is shown in (Fig. 3-41).

Inspection of the TGA spectrum reveals the temperature region around 450°C is where rapid conversion of the carbon and hydrogen into CO_2 and water with concomitant formation of SiO_2 occurs. It is also observed that if the Si-GDP is heated to temperatures nearing 600°C before this conversion process is complete the resulting shells are black in color due to appreciable carbon content in the glass. Based on TGA results, which show a relatively rapid conversion rate at 450°C, this temperature was chosen as the optimum for the conversion of Si-GDP to SiO_2.

Although the removal of carbon and apparently the pickup of oxygen is essentially complete by 600°C, the glass shell at that temperature is not yet at full density. The shells generally shrink another percent or two in diameter (without loss of mass) when heated to 1000°C. Also, the permeation properties of the final shells vary depending on the final temperature and hold time.

Permeation experiments were conducted using D_2. The deuterium gas was permeated into the glass mandrels by heating them in a sealed, pressurized vessel to 260°C. The out-gassing rate (at room temperature) of D_2 was monitored by interferometry or by mass spectrometry. Shells on occasion were crushed in our shell crushing station to accurately determine total internal pressure, residual gas content, and the corresponding half-life as well.

3.13.2. Results and Discussion

The only variables we can adjust, to control the final properties of the glass shells (color and permeability) and residual gas content, are the temperature ramp/soak profile and Si-GDP to glass pyrolysis atmosphere. We have not yet tried adjusting the O_2 pressure in the pyrolysis oven during the conversion process but instead have focused on making adjustments in the temperature ramp/soak profile.

Color (Carbon Contamination). Thermogravimetric data on the conversion of Si-GDP to SiO_2 (Fig. 3-41) indicates that the mass of the sample does not change significantly after ~580°C. This agrees well with the observation that in order to make clear, non-colored, glass shells the conversion of Si-GDP to SiO_2 must be essentially complete before 600°C is reached. If the Si-GDP shells are heated too rapidly in air to 600°C the resulting shells can be anywhere from light brown to opaque and black after the high temperature densification step (sintering from 600–900°C). This is presumed to be due to incomplete combustion of the carbon present in the Si-GDP and resulting incorporation into the densified glass.

The effect of residual carbon on shell properties, such as strength and permeability, has not been systematically investigated yet. However, the colored glass shells that have been measured for deuterium half-life have a somewhat higher permeability (shorter deuterium half-life) than corresponding colorless glass shells.

We have been adjusting the pyrolysis profile based on our TGA results by increasing the hold time at 450°C. Generally, if we hold the shell long enough at 450°C in an oxygen containing environment we will obtain colorless glass shells after the high temperature densification step.

Residual Gas Pressure and Composition. Up until five years ago, we only had the capability to measure gas pressure inside a capsule by crushing it while immersed in a viscous fluid (glycerin typically). This technique, while generally not used anymore, does have the advantage of providing visual evidence in the form of bubbles from which the total gas pressure inside the capsule can be easily determined. For glass shells made from the Si-GDP to glass process, the entrapped gas generally consists of a mixture of CO and CO_2. Figure 3-42 shows the residual gas bubbles from a glass shell that was crushed while immersed in glycerin along with a typical mass spectrum of the entrapped gas inside glass shells made by this process.

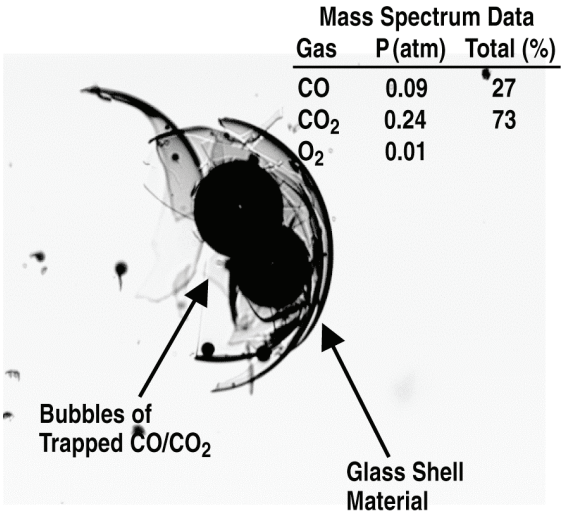

Fig. 3-42. Glass shell crushed under glycerin showing entrapped gas remaining from the pyrolysis process.

About five years ago, we constructed a shell crusher station that allowed us to more easily and more accurately measure high pressure fills. The shell crusher station consisted of a small, calibrated volume connected to a turbo pump and an MKS 10 Torr high precision Baratron gauge. The internal gas pressure of a shell is determined by crushing it inside the calibrated volume and measuring the resulting pressure rise in the system using the gas law $P_1V_1 = P_2V_2$ and correcting for non-ideal gas behavior as necessary. We recently attached a mass spectrometer to the shell crushing station which allows us to determine composition of the gas(es) in addition to the total pressure.

Minimizing the total amount of residual gas present inside a glass shell generally follows the minimization of the color. This makes sense since oxygen needs to permeate inside the shell during the pyrolysis in order to oxidize the carbon. If oxygen can permeate, then the gases formed (CO, CO_2 and water) should be able to permeate out. Table 3-4 shows the results of experiments to minimize the total residual gas content. We have been able to produce shells with total residual gas content of < 0.1 atm.

Table 3-4
Residual Gas is Minimized by Increasing Hold Time at 450°C Prior to Sintering at 940°C

Shell o.d. (μm)	Shell wall (μm)	Pyro Time at 450°C (h)	Residual CO (atm)	Residual CO_2 (atm)	Total (atm)
1082	5	60	0.01	0.18	0.19
1123	5	60	0.02	0.17	0.18
1126	5	60	0.02	0.15	0.17
1106	5	100	0.01	0.04	0.04
1115	5	100	0.01	0.04	0.04

Permeation. The literature value for the permeability constant K for deuterium through amorphous silica is 2.67×10^{-20} (mol•m)/(m^2•s•Pa) [3-55]. The permeability constant (K) for deuterium found previously for drop-tower produced glass mandrels is 3.0×10^{-20} [3-56]. Generally, the deuterium permeation constant K of shells made by this process, when sintered to full density at 940°C, is also consistent with the accepted literature value. However, K can also be made to vary significantly resulting in much higher permeability if desired. This allows the deuterium half-life to be better

tailored to the occasional experiment where the full density half-life is too short to allow for target handling and processing time but too long for practical filling of the target after assembly. Measurement of the deuterium half-life and corresponding K values for a series of shells sintered to different final temperatures are shown in Table 3-5.

Table 3-5
Permeability of Si-GDP Produced Glass Shells at Various Sintering Temperatures

o.d. (μm)	Wall (μm)	K (mol•m)/(m^{2}sPa)	Sintering Temperaure (°C)	DD Half-Life (days)
~250	8	2.3×10^{-20}	940	50
~250	8	8.5×10^{-20}	920	11
~250	8	5.2×10^{-19}	820	1.8

Literature value for deuterium through SiO_2 is 2.7×10^{-20}.

Future Development. Diamond shells have been identified as potentially useful for ICF targets because of their very high strength, attractive density and low atomic number. We have discovered it is possible to pyrolyze Si-GDP mandrels to 900°C in an oxygen free atmosphere resulting in shiny, black shells as shown in Fig. 3-43.

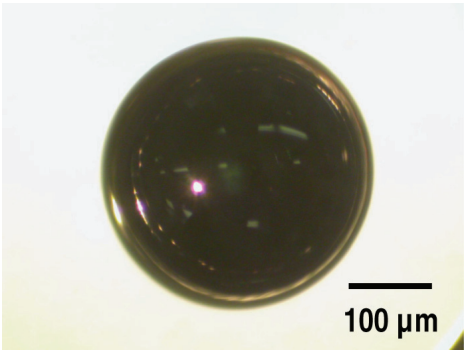

Fig. 3-43. High carbon shells (~20% Si/80% C) — lower Z than glass, stronger and less permeable than plastic (dense carbon like).

Based on the final shell mass and assuming there is no significant loss of silicon during the pyrolysis, we estimate that this shell is 20%Si and 80%C. These shells may potentially be of interest because they are possibly intermediate in properties between glass and diamond. The shells are somewhat higher Z than diamond but lower average Z than glass and appear to be relatively easy to make and should be free of residual trapped gas(es) since they are pyrolzed in vacuum. We intend to investigate the permeation and strength properties of some shells produced in this method to determine if they have potential for use as ICF targets.

In another development, while it previously has not been possible to manufacture ≥ 2 mm diameter glass shells with very thin walls (≤ 5 μm), generally due to destruction of the mandrel during the PAMS pyrolysis step, we have successfully made a glass shell 2150 μm in diameter with 3.3 μm wall thickness (Fig. 3-44) by laser drilling a ~ 15 μm hole into the precursor Si-GDP shell prior to the PAMS removal step. The hole provides a pathway for ready removal of the PAMS during pyrolysis, instead of having the gaseous PAMS diffuse through the thin Si-GDP layer. The reduced internal pressure results in intact Si-GDP mandrels. The advantages of having the small hole in the glass shell

is it assures there are no residual gases and allows for any type of gas fill using fill tubes or fill and plug techniques. We will fabricate more of these shells as time allows to determine how well they maintain sphericity and surface finish.

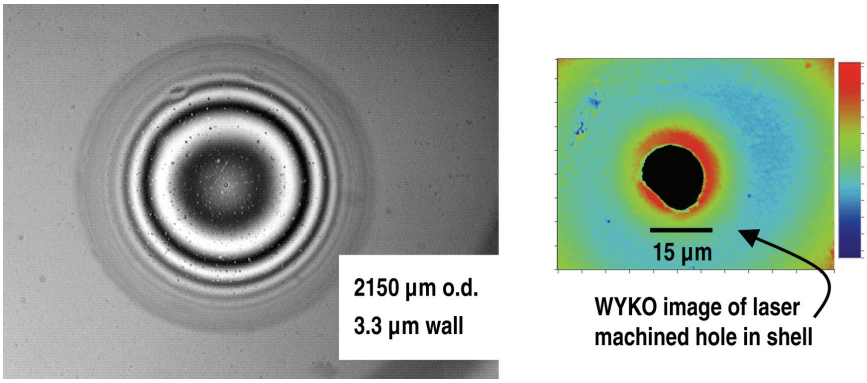

Fig. 3-44. Drill and fill development: Interferometric image of large, thin-walled glass shell with small hole — no residual gas; tailored gas fills; very high aspect ratio.

3.14. DEVELOPMENT OF A GDP COATER ENABLING INCREASED PRODUCTION — B.A. Vermillion, J.T. Bousquet, R.E. Andrews, M. Thi, M. Hoppe, E.R. Castillo, A. Nikroo, D.G. Goodin (GA)

We are developing a GDP coating system to enable large scale capsule production into the hundreds or thousands. Our concept is a horizontal rotary configuration, an evolution from a first-generation fluidized bed system. Pictured in Fig. 3-45 is a simplified schematic. We utilize two MKS mass flow controllers for the precursor (T_2B) and etching gases (H_2) with nominal mass flow rates for the T_2B and H_2 at 0.4 and 10 sccm, respectively.

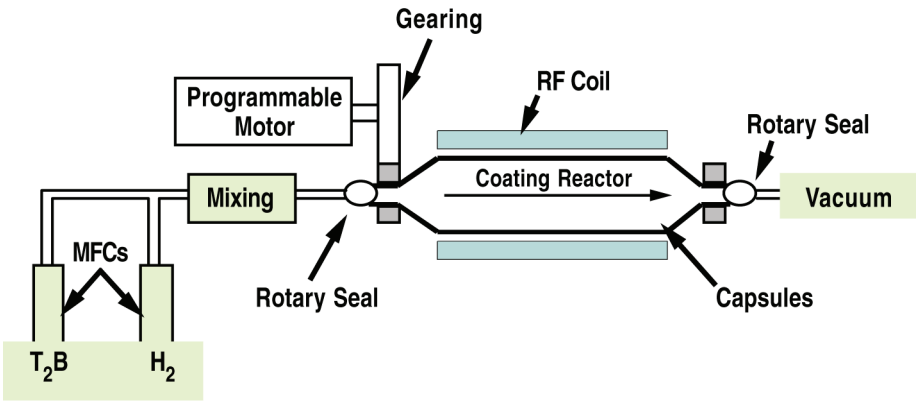

Fig. 3-45. Schematic of rotary coater. Gas flow is from left to right.

The coating chamber itself is a 5 in. diameter, 20 in. long glass reactor rotated by a programmable motion motor. The plasma is generated by a custom designed RF coil operating at 35 MHz and approximately 25 W. The coil is currently located in the middle third of the reactor but its position can be modified upstream or downstream of center. Figure 3-46 shows a picture of the system with the plasma activated.

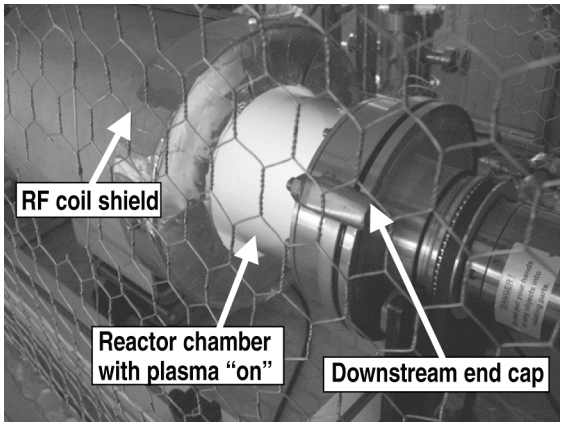

Fig. 3-46. The glass reactor chamber with the plasma "on".

Currently, we employ an intermittent rotation scheme with 30 s dwell times followed by a slow, 5 s long, quarter revolution of the chamber to reduce capsule to capsule collisions. Additionally, we introduced a system utilizing a piezoelectric motor to tap the glass periodically to prevent capsules from sticking to the reactor walls due to static. At this agitation rate the coated capsules' measured $4\pi\Delta$ wall is less than 0.5 μm for the rotary coater system, comparable to GDP coater runs. AFM measurements utilizing the Spheremapper system at GA indicate that we have achieved NIF CH smoothness specifications for 3 out of 5 capsules sampled from a 400 count capsule batch, a key benchmark for successful coatings. Figure 3-47 is a summary of AFMs for five 2 mm PAMS mandrels from the 400 count batch coated to 10 μm thickness in the new system.

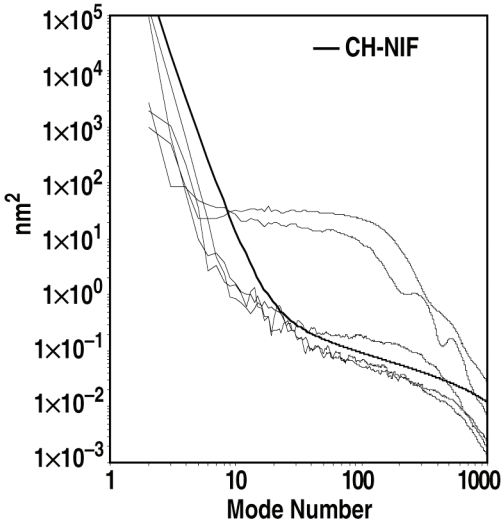

Fig. 3-47. Five AFMs from 400 count rotary coater batch. Three of five are acceptable compared to smoothness specification of CH-NIF.

We have successfully maintained capsule-to-capsule wall uniformity with larger batches in the rotary coater to within ±10% of the mean wall thickness (typical specification for current GDP coaters is ± 5%). We believe the slight increase in wall thickness variation in the larger batch results from the reduced coating rates to be found in the middle of the reactor.

We produced gas tight coatings on both full density plastic and foam capsules with the rotary coater. We coated 2 mm diameter PAMS mandrels with GDP in the rotary coater and achieved gas tight coatings with a 27 min Ar half-life, confirmed with an XRF half-life measurement technique, nominal for this material and size of capsule. Additionally, we successfully applied a gas tight coating with a 4 min Ar half-life on smaller RF low density foam capsules, once again nominal for this material and size capsule.

To further improve surface finish, we intend to reduce rotation and tapping frequency until the coatings begin to show increased non-concentricity and OOR, thereby establishing minimum agitation parameters that maximize surface smoothness. To further reduce capsule-to-capsule wall thickness non-uniformity, we intend to add fins to the inner wall of the reactor tube to roll the capsules up and down stream through the reactor chamber thereby averaging the time capsules spend in different coating rate regions of the reactor. We intend to perform combustion analysis to indicate whether we are achieving coatings similar in carbon to hydrogen ratio to those produced in current GDP systems. This will provide feedback for modifying precursor to etching gas flow rates to improve buckle and burst strength of the GDP capsules, as well as to optimize gas flows to increase GDP coating rates.

NIC DIRECT DRIVE TARGET DEVELOPMENT

3.15. MONOLITHIC FILL-TUBE TARGET DEVELOPMENT UPDATE — E.L. Alfonso, A.Q.L. Nguyen, D.G. Czechowicz, J. Crippen (GA)

A fill tube on an ICF capsule is the approach to fuel loading for near-term cryogenic shots because it allows for elimination of cryogenic transport and increases the choice of ablator. The interference to high-quality implosions will be minimized if perturbations on the capsule surface are minimized. Simulations have shown that for ~1 mm o.d. capsules, the fill tube requirement is a diameter of 10-20 μm [3-57]. We have fabricated a plastic capsule with a MFT with a diameter of less than 15 μm. Because the fill tube is integrated during the fabrication of the capsule, no attachment on the capsule is necessary during assembly. Thus, the glue joint to the source of fill gas is hundreds of microns off the capsule surface and perturbations are reduced. Also, capsule fabrication is a batch process — many capsules can be produced at once. This article details the fabrication and characterization of the MFT capsule. Polymer MFT capsules with outer diameters of 0.9 and 3.1 mm with wall thickness of ~ 4 and ~15 μm, respectively, have been produced. The MFT capsules are attached to a supplementary fill tube to the gas source. The targets are inspected, characterized, and tested for gas retention.

3.15.1. FABRICATION OF THE MONOLITHIC FILL TUBE CAPSULE

The well-documented process of depositing plasma polymer onto a depolymerizable PAMS mandrel was used to make the MFT capsules [3-36]. The difference to make MFT capsules from the standard case is the addition of a PAMS stalk (or "tail") on the mandrel [3-44]. Because the plasma polymer replicates features on the mandrel, the initial size and shape of the attached PAMS tail determines the size and shape of the fill tube on the MFT capsule (accounting for the plasma polymer coating thickness). We have built an assembly station to produce these PAMS tail mandrels. It consists of a multi-view microscope system and XYZ-micromanipulator which positions the PAMS shell over a heated reservoir. Melted PAMS is forced to flow through the nozzle tip of the reservoir. As the PAMS shell is briefly touched to the melt and pulled away, a small tail forms on the shell and quickly solidifies, as shown in Fig. 3-48. This process is well described elsewhere in this issue [3-58]. The assembly system allows control of the stalk diameter and length (which can also be

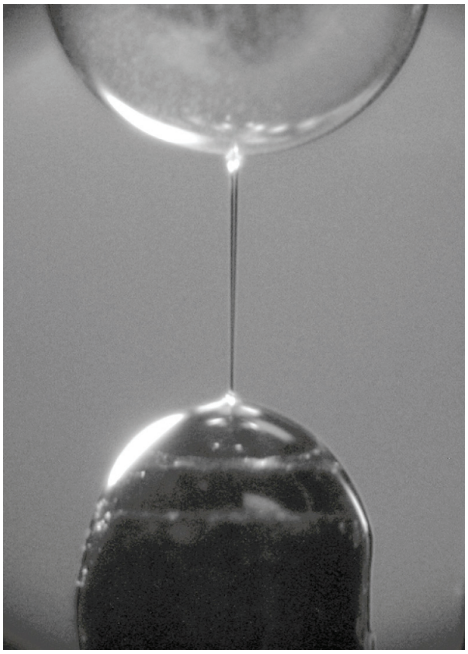

Fig. 3-48. Magnified view of PAMS "tail" formation from the melt onto PAMS mandrel (top of photo). The tail quickly solidifies into a solid stalk.

trimmed to desired length). A PAMS tail mandrel is shown in Fig. 3-49. Mandrels with tail diameter less than 10 μm and length greater than 100 μm are regularly produced.

Fig. 3-49. An 11 μm diam PAMS stalk attached to the mandrel.

PAMS tail mandrels of the appropriate size are chosen with the desired tail diameter and length. We have used both 0.9 and 3.1-mm-o.d. mandrels, nominal sizes for OMEGA and NIF, respectively. Typically, 40 mandrels comprise one coating batch for 0.9-mm-o.d. capsules, while 7 are used for 3-mm-o.d. capsules. The batch of mandrels is placed in a bounce pan to agitate the mandrels during plasma polymer coating to produce a uniform wall thickness. The plasma polymer-coated shells are pyrolyzed in a nitrogen atmosphere to remove the PAMS. The resultant plasma polymer capsule has a hollow fill tube remaining on the surface. An SEM image of the fill tube on an MFT capsule is shown in Fig. 3-50.

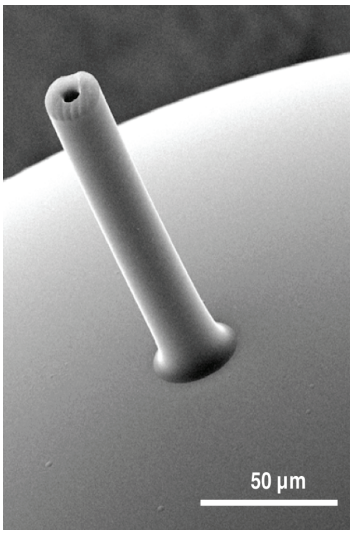

Fig. 3-50. SEM image of the fill tube on an MFT capsule. Fill tube: ~15 μm diam, ~100 μm long. Capsule: 0.9 mm diam, 4 μm thick.

When purely spherical mandrels are used in the plasma polymer process, a large yield of shells (>75%) with wall nonuniformity of less than 0.5 μm are produced. However, MFT capsules are found to have greater wall nonuniformity under typical coating conditions. It is presumed that the tail on the mandrel prevents true random motion. Wall-map traces of a capsule (0.9 mm o.d., 4 μm wall) around the orbit including the fill tube and around the equator (with the fill tube at the pole) are shown in Fig. 3-51. Clearly, a P1 nonuniformity exists in the former trace due to the fill tube effects during coating. The capsule is uniform in the longitudinal trace. The thin side of the capsule is always on the opposite pole of the fill tube. Because the tail down position is the least likely position during coating, the fill tube's opposite side rarely faces the plasma polymer source directly. To overcome this effect, MFT capsules were produced in smaller batches and with increased amplitude of the bounce pan to allow greater mandrel motion. The effects of those changes are presented in a scatter plot of the wall non-uniformity by batch, shown in Fig. 3-52. By reducing batch size and increasing agitation, about 40% of capsules have nonuniformity less than 0.5 μm. The tail length also contributes to the nonuniformity in wall thickness. As expected, longer tails have more restricted motion during coating and lead to greater nonuniformity, while shorter tails have better uniformity. It is desired to have MFTs greater than 100 μm to make assembly easier, however. Generally speaking, a reasonable yield of MFT capsule with wall thickness nonuniformity levels near those of capsules starting from purely spherical mandrels can be produced. Surfaces were inspected via WYKO interferometry on capsules fabricated with increased agitation. No increase in roughness was detected.

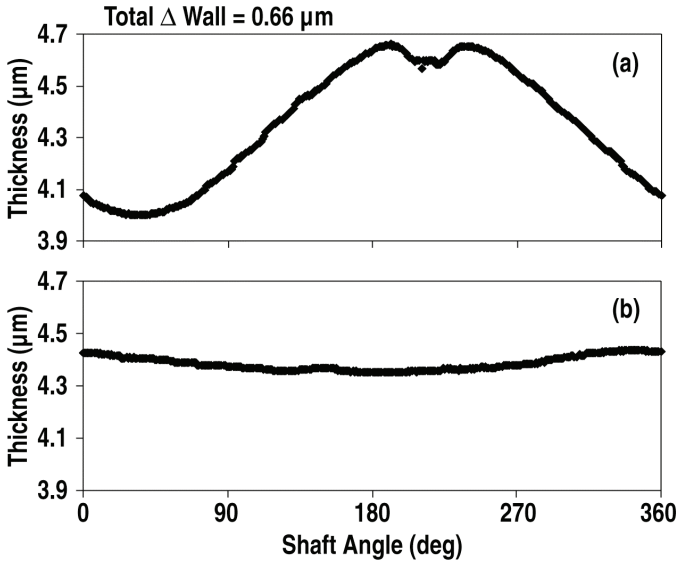

Fig. 3-51. Wall-map traces around MFT capsule (0.9 mm o.d., 4 μm wall): (a) in the orbit including the fill tube (the kink in the data points is due to the fill tube) and (b) around the capsule equator with the fill tube at the pole. The nonuniformity in fill tube orbit is ~ 0.7 μm and in the equator is ~ 0.1 μm.

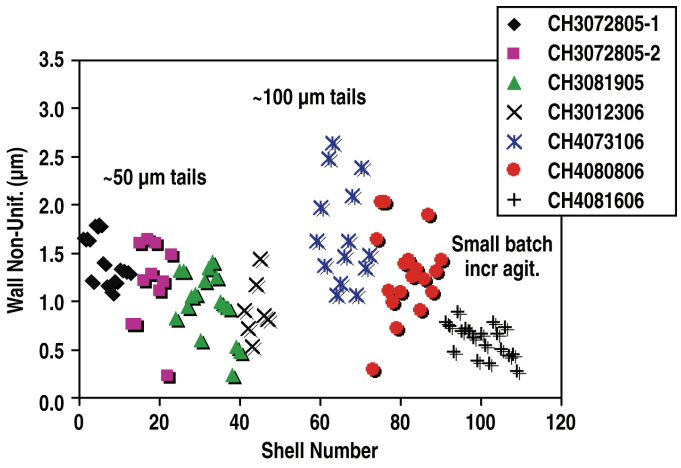

Fig. 3-52. Wall nonuniformity for various MFT capsules. Shorter fill tubes lead to smaller nonuniformities. The uniformity is improved by reducing the batch size to 20 mandrels and increasing the agitation during coating.

3.15.2. Assembly and Gas Testing of the Target

The fill tube on the MFT capsule is nominally 100 μm long. This capsule is attached at the tip of the MFT to a longer supplementary fill tube that can connect to a gas source. Polymer fill tubes were chosen due to their flexibility and low-Z content. A polyimide (PI) fill tube (10-20 μm o.d.) was made from ~1 mm o.d. polyimide hollow tube [3-59]. The open end of the hollow tube is glued into a stainless steel tube brazed into a VCR vacuum fitting. The polyimide fill tubes are inspected and laser-trimmed to mate with the opening of the MFT capsule. The polyimide fill tube tip and MFT capsule are aligned with the assembly station to ensure a dry fit. A UV-curing adhesive was applied minimally around the fill tube-shell joint with a micro-applicator and cured. The glue spot is a few microns in diameter on the outside of the tube, but this perturbation is far removed from the capsule surface. An example of the attachment joint of a 3.1 mm o.d. capsule is shown in Fig. 3-53.

After the MFT capsule is assembled with the supplementary polyimide fill tube, it is tested for gas retention. Common failure modes are cracks in the capsule or joints causing leakage, and accidental plugging of the hole during assembly preventing flow. To test the target, the source end of the fill tube is attached to a pressure vessel containing Ar. We have adapted the Kevex Omicron XRF system to allow pass-through of the gas fill line. After evacuating the shell and XRF system, Ar is allowed to flow into the MFT capsule. The x-ray source is focused on the MFT capsule and the XRF due to Ar is recorded. Several areas around the shell and its environment are probed to verify the fill gas is inside the capsule.

3.15.3. Conclusion

Plasma polymer capsules have been fabricated with a MFT with 10-20 μm diam. The technique to fabricate the fill tube employed a depolymerizable stalk on the mandrel. The capsules were 0.9 mm o.d. with a ~ 4 μm wall and 3.1 mm o.d. with a ~15 μm wall. A wall nonuniformity of less than 0.5 μm could be achieved. The MFT capsules were attached to flexible supplemental polyimide fill tubes to a gas source. The shells were examined for gas retention and were confirmed to be gas tight.

Fig. 3-53. A 3.1-mm-o.d. MFT capsule attached to the supplemental polyimide fill tube. The glue joint is ~100 μm from the capsule surface.

3.16. IMPROVING THE WALL UNIFORMITY OF RESORCINOL FORMALDEHYDE FOAM SHELLS BY MODIFYING EMULSION COMPONENTS — R.R. Paguio, M. Thi, J.F. Hund, A. Nikroo, S. Paguio, R. Luo, A.L. Greenwood (GA), M. Takagi (LLNL), O. Acenas (CSU-Long Beach), S. Chowdhury (UCSD)

Foam shells are used for direct drive ICF experiments on the OMEGA facility at the UR/LLE and will be used in future experiments on the NIF. The shells needed for OMEGA experiments have diameters of ~850–900 μm which are scaled down versions of the targets that are required for high gain wetted foam direct drive ignition designs on NIF [3-60]. Cryogenic targets require a wall thickness of 50-100 μm, a non-concentricity of ≤ 5%, with a foam density of 30-150 mg/cc. The room temperature foam shell surrogates, mimicking the D_2 or DT ice layer need to have a wall thickness of 80-120 μm and a foam density of 180-250 mg/cc. These targets are designed to reduce the need for difficult to field cryogenic shots with the foam serving to simulate the cryogenic fuel layer.

Because the foam material is porous, the foam shell by itself cannot hold the required fill gas (D_2 or DT). For wetted cryogenic foam shells to hold a fill gas, a pinhole free permeation barrier is overcoated around the shell. For room temperature surrogates an additional coating of 1000Å of aluminum is added to assist in gas retention [3-61].

RF was chosen as the foam material because of its transparency, allowing for routine optical characterization. The optical transparency is due to the characteristically small pores (~ 0.10 μm) of the RF aerogel, first developed by Pekala, et al. [3-62]. The fabrication of RF foam shells was later developed by Lambert, et al. [3-63]. Due to the fragile nature of the foam shell preform, this work only achieved a yield of ~33% for intact shells. We extended this work by transforming the process into a repeatable, reliable, high yield production process to fabricate intact shells with a yield of over 90% [3-64–3-66]. We have also been able to develop the required pinhole-free permeation barrier in order for these shells to hold the required fill gas (DT or D_2) by overcoating the shells with a GDP by chemical vapor deposition (CVD) [3-64–3-66]. This process was achieved for both standard density RF (SDRF) foam shells which have a foam density of ~100 mg/cc and high density RF (HDRF) foam shells which have a foam density that can range from 180-200 mg/cc [3-65,3-66].

3.16.1. Experimental

RF foam shells were fabricated by using the triple orifice droplet generator [3-63–3-66]. The triple orifice droplet generator method allows precise control of shell diameters and wall thickness, so that a large quantity of similar shells of a specified size can be made [3-63–3-70]. In our standard baseline process, the droplet generator creates shells by a double emulsion of an inner oil (O1), aerogel/foam precursor (W1), and an outer oil (O2). A diagram of this fabrication process is shown in Fig. 3-54.

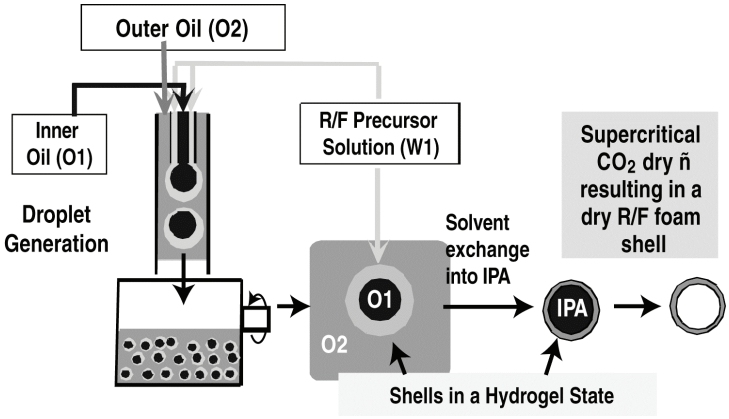

Fig. 3-54. Diagram illustrating RF foam shell fabrication by the microencapsulation process using a triple orifice droplet generator.

Several polymer additives were investigated in order to modify the interfacial tension of the RF emulsion system. The polymer additives were screened by first testing their compatibility with the O2 solution. If the polymer was compatible with the solution, the polymer additive was then tested on how it effected the interfacial tension of the RF emulsion system. The interfacial tension of the emulsion system was measured by an interfacial tensiometer (Future Digital Scientific Model OCA-15) which measures the interfacial tension by the pendent drop method [3-71].

The dried shells are over-coated with a pinhole-free gas permeation barrier. GDP was chosen as the permeation barrier for these shells [3-64–3-66]. GDP was overcoated on the shell by CVD. The barrier is tested for gas retention by permeation filling the shells with 900 Torr of Ar and tracking the Ar content versus time using XRF.

3.16.2. Results and Discussion

IFT of Current Process. This investigation of the interfacial tension of the RF emulsion system and how it could play a role in the wall uniformity of the RF shells is an extension of our previous work on full density polymer shells made from PAMS [3-68,3-69]. Before modifying the interfacial tension of the RF emulsion system, the current RF emulsion system was measured and compared with other shell systems that are fabricated by the microencapsulation process using a droplet generator. We compared the current RF emulsion to PAMS shells and DVB foam shells [3-65,3-70]. The DVB and PAMS shells have a higher yield of shells that meet the NC specification than the RF foam shells. This is illustrated in Fig. 3-55, which shows that the IFT of the PAMS and DVB shells is 16–28 times higher than the RF shells. The results also show that a higher IFT leads to a greater yield of shells that meet the NC specification.

The RF emulsion system for the standard process was also investigated for specific components in the emulsion system that caused the IFT to be low. The component that was found to be the culprit

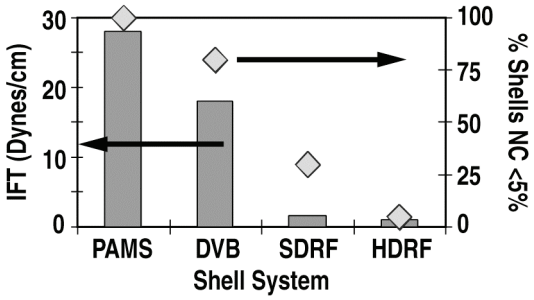

Fig. 3-55. Comparing the interfacial tension (bars) and the yield of shells that meet the NC specification (diamonds) for other shell systems and the traditional HDRF and SDRF fabrication process. This graph empirically shows that IFT can influence the concentricity of the shells.

was the span 80. Span 80 is the surfactant in the O2 solution that helps prevent the RF foam shells from being tacky and agglomerating with one another. Lowering the span 80 concentration or removing it will cause the RF shells to agglomerate, resulting in a yield of no intact shells. This led us to investigate other additives that could replace the span 80. These other additives must increase the IFT of the RF emulsion system as well as prevent the RF shells from agglomerating.

Increasing the IFT of the RF Emulsion System. Several polymer additives were investigated as possible replacements for the span 80 with a styrene-butadiene-styrene (SBS) polymer being found to be most promising. The SBS was found to be compatible with the O2 solution and increased the IFT of the RF emulsion system from 1 to 21 dynes/cm. From these results, RF foam shells were fabricated with 0.60% SBS replacing the Span 80 in the O2 solution — we will refer to this as modification 1.

The shells fabricated from modification 1 were able to survive through the curing step in which the shells are in the hydrogel stage in isopropyl alcohol (IPA) at high yields with no agglomeration. The shells visually appeared to have better wall uniformity than the shells fabricated with the standard process. But when the shells were dried in the CPD, the shells agglomerated. We then tried fabricating shells with modification 1 and added the span 80 at different times during the curing step, but the shells still agglomerated with each other after the shells were dried in the CPD. This led to the fabrication of RF shells with 0.60 wt% SBS and 0.10% Span 80 in the O_2 solution which we will refer to as modification 2. The IFT of the RF emulsion system with this modification was 4 dynes/cm, which was still higher than the standard emulsion system at 1 dyne/cm. Though this IFT increase was not as dramatic as modification 1, a visual improvement on the wall uniformity of these shells occurred when they were in their hydrogel state in IPA and compared to shells fabricated with the standard process. Shells fabricated by modification 2 did not agglomerate with each other when dried in the CPD. The shells looked very similar to the standard RF shells when dried. HDRF and SDRF RF shells fabricated using modification 2 were measured for NC. The yield of shells that met the NC specification increased from 30-90% for SDRF shells. For HDRF, the yield was improved from <5% to 25%. Theses results are shown in Fig. 3-56. Besides improving the concentricity of the shells, their sphericity was also improved which was what the IFT has been shown to effect in theory. Shell sphericity is defined in terms of OOR (where, OOR = max radius – min radius). The OOR was improved from 4 to 1 μm by using this method.

Overcoat and Gas Retention. In addition to having a good NC, these RF shells are required to hold a fill gas. These shells were successfully coated with 3-4 μm of GDP by CVD, similar to the standard RF foam shell fabrication process. Approximately 24% of the shells overcoated with GDP were gas

retentive, this is a lower yield when compared to the traditional HDRF and SDRF shells which are ~50% gas retentive. More gas testing must still be done to confirm these results. Future work will include improving the gas retention of these SBS-modified RF shells.

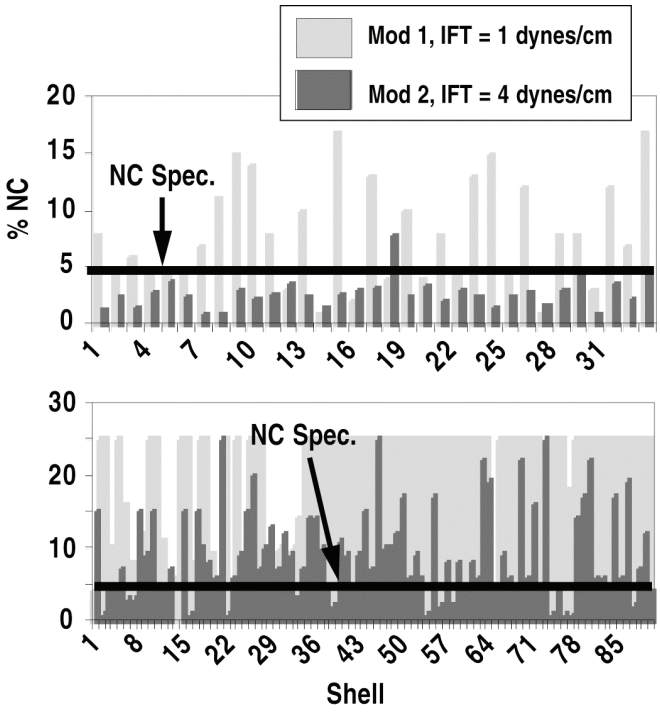

Fig. 3-56. The NC of SDRF and HDRF shells fabricated with the traditional modification 1 process (IFT of 1 dynes/cm) and modification 2 (IFT of 4 dynes/cm). By increasing the IFT from 1 to 4 dynes/cm the yield of shells that meet the NC specification dramatically improves.

Conclusion for Section 3.16

The IFT for both low and high density RF foam shell systems were increased by adding the SBS polymer to the O2 solution. This led to a process to fabricate more concentric RF foam shells that meet the NC specification. By implementing this modification, the yield of shells that met the target specification for NC in SDRF foam shells improved from 30% to 90%, and in HDRF foam shells the yield improved from <5% to ~25%. Though there is no scientific theory on how IFT affects the NC of these shells, these results empirically show that the IFT influences the shell concentricity. In the future, we will focus on improving the gas retention of the shells fabricated with this process.

3.17. FABRICATION AND CHARACTERIZATION OF ALUMINUM OXIDE AEROGEL BACKLIGHTER TARGETS — J.F. Hund, C.A. Frederick, A. Nikroo, A.L. Greenwood, W. Luo (GA), J. McElfresh (UCSD)

Aluminum is one of several elements of interest as a backlighter for ICF and related high energy density physics experiments. In this work, low density (50 to 400 mg/cc) aluminum oxide aerogels were fabricated for a series of short pulse backlighter experiments. These experiments are an ongoing series by researchers at the University of Rochester to study the effect of target density on emission intensity. In order to assure reproducible plasma characteristics from shot to shot, it is important that the pores be small for porous material compared to the wavelength of the incident laser radiation.

The classic method in literature for producing alumina aerogel is the Yoldas method [3-72] in which aluminum sec-butoxide is used as the precursor. Recently, epoxides were used as catalysts for sol gel reactions [3-73] and were chosen as the synthesis method for these targets.

3.17.1. Experimental

Flat, thin alumina aerogels were fabricated as shown in Fig. 3-57. The aerogels were cast from a solution of water and ethanol (50%vol/vol) and aluminum chloride hexahydrate. An excess of propylene oxide was then added to catalyze gelation. The solution was subsequently poured into a container with molds made from quartz slides as shown in Fig. 3-58. The solution was allowed to gel under dry N_2 for 24 h. Ethanol was added on top of the solid gel and allowed to cure for 24 h. The gels were then solvent exchanged into isopropanol to remove the remaining water and unrelated precursor materials in the gels. The gels were then dried with supercritical CO_2.

Fig. 3-57. Picture of a ~100 mg/cc alumina aerogel of 0.7 mm thickness.

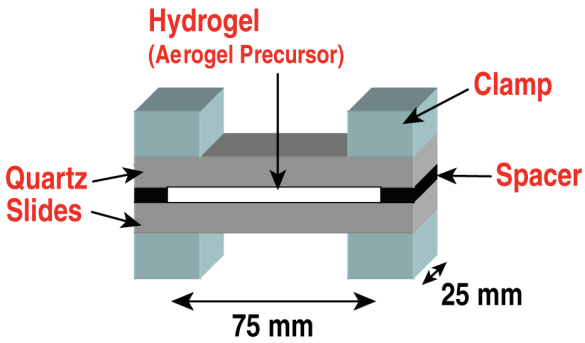

Fig. 3-58. Diagram of mold used in casting the 0.7 mm thick alumina aerogel targets. The targets were cut to the correct lateral dimensions after removal from the mold.

3.17.2. Results and Discussion

It was found that the density could be controlled from 25 to 200 mg/cc by adjusting the aluminum chloride concentration (Fig. 3-59). The density was limited at the lower limit by the inability of the solution to fully solidify during the gelation (below concentrations of ~ 0.1 moles/L). This led to gels that would not retain their shape after separating from the mold. At a concentration of 0.1 mole/L, the gel was soft and shrank more than the gels made with higher concentrations. At the higher concentrations, there was a linear relationship between density and amount of aluminum chloride added. For concentrations higher than ~ 2 moles/L, a practical limit was reached due to the difficulty of dissolving all the aluminum chloride in the starting solution.

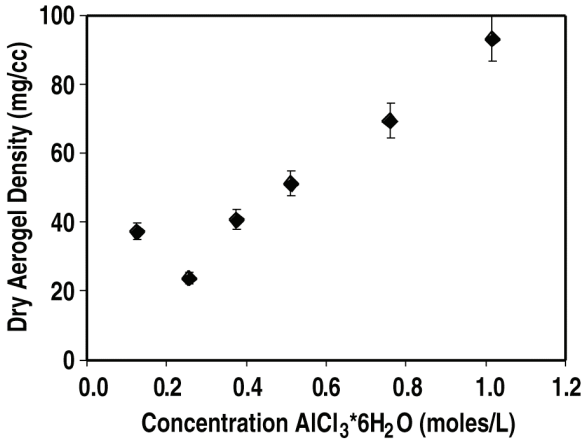

Fig. 3-59. Starting concentration of aluminum chloride in precursor solution and density of the final dry aerogel.

The density can also be increased post process by heat treating the dry aerogels (Fig. 3-60). By heating under dry N_2, the alumina aerogel shrinks and increases in density while retaining its basic shape. During this process, water is also lost from the aerogel. As fabricated before heat treatment,

the aerogel contains 39% water. At 800°C, all the water of the alumina (hydrate) aerogel is evolved from the sample (Fig. 3-61). Understanding both the shrinkage and water loss enables estimation of the elemental aluminum content that can then be verified via XRF of elemental analysis.

The aerogels fabricated have a small pore structure on the order of 1 to 10 nm as shown by SEM (Fig. 3-62). N_2 adsorption data confirms this, with a large number of pores ~ 3 nm in size. Due to the optical transparency of the aerogels fabricated, few if any pores exist above 1 μm in size.

Conclusion for Section 3.17

Alumina aerogels were successfully fabricated and characterized at 600 to 1000 μm thickness. We were able to produce a range of densities from 25 to 400 mg/cc. Future work will continue on expanding the range of densities, improving the surface finish, and investigating supercritical drying in other solvents besides CO_2.

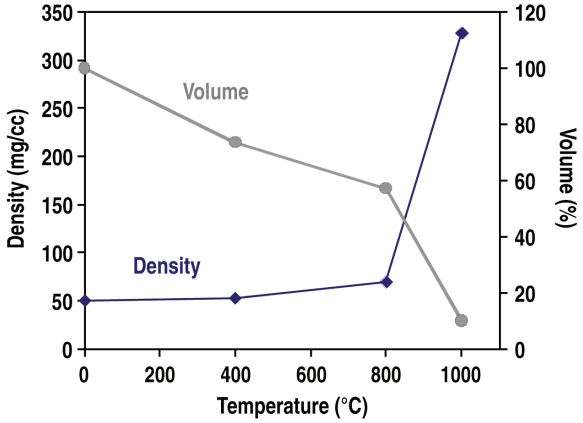

Fig. 3-60. Density versus heating conditions. By heating the alumina aerogel, higher densities can be achieved.

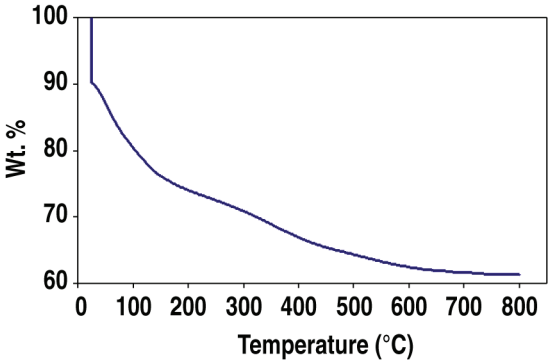

Fig. 3-61. Weight versus temperature from TGA. A dramatic weight loss is seen at low temperatures corresponding to loss of adsorbed water. At higher temperatures, water that is chemically bonded is released.

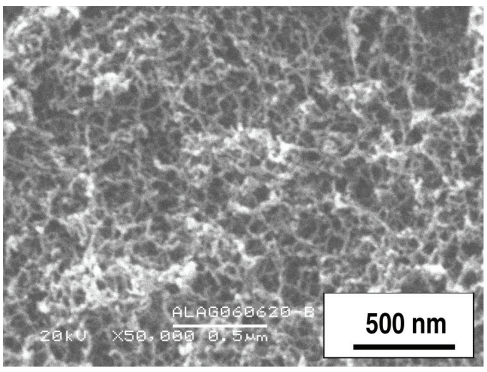

Fig. 3-62. SEM of alumina aerogel.

SNL TARGET DEVELOPMENT AND PRODUCTION

3.18. FABRICATION OF MULTIPLE FILL TUBE TARGETS FOR SANDIA NATIONAL LABORATORY — C.A. Frederick, C. Back, A. Nikroo (GA), M. Takagi (LLNL)

The NIF capsule design will use fill tubes to allow for DT filling [3-74]. Fill tubes introduce hydrodynamic perturbations on capsule implosions and were modeled with computer simulations.

Fill tube perturbation experiments were designed for the Z-Pinch facility at SNL. The design called for a 2 mm diameter, 80-μm thick CH capsule. The outer 40 μm layer was to be doped with 1 at. % germanium to increase contrast during experiments. Capsules with three and four fill tubes 90 deg apart on the equatorial plane were designed to maximize data per shot, allow for the best comparison of data, and to study the radiation shadowing effects caused by varying diameter and composition of fill tubes.

3.18.1. Fabrication

Holes were laser drilled in 2 mm o.d., 80 μm thick capsules using a 248 nm excimer laser with 5 axis stage control [3-31,3-33,3-75]. Figure 3-63 shows x-ray images of typical laser drilled holes. The holes appear to be "trumpet" shaped, wider on the shell surface then tapering to a constant diameter.

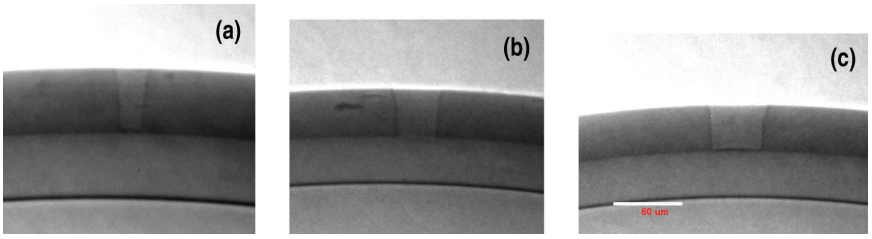

Fig. 3-63. X-ray images of three holes laser drilled through a capsule's Ge-GDP outer layer down to the un-doped GDP layer at 40 μm depth.

CH and SiO_2 fill tubes were fabricated for the experiments. The SiO_2 fill tubes were made using a commercial capillary puller and 20 μl pipettes. The CH fill tubes were fabricated with a modified glass capillary puller using Aurum® thermoplastic tubing. Once the CH fill tubes were pulled, they were cut with the excimer laser to the desired length.

A specially designed fill tube assembly station was used to attach the fill tubes to the capsules. Figure 3-64 is a schematic and picture of the assembly station. To fabricate these targets, a pin vise holding the mounting stalk with shell was held with an XYZ manipulator and a fill tube was held in a second manipulator. The shell was positioned with the hole positioned on the apex. Epoxy was applied to the fill tube tip which was then positioned normal to the shell surface and inserted into the

hole. Once inserted into the hole, the fill tube was manipulated so that it was normal to the surface of the shell. Then the epoxy was cured with uv light. Figure 3-65 shows two fully assembled targets.

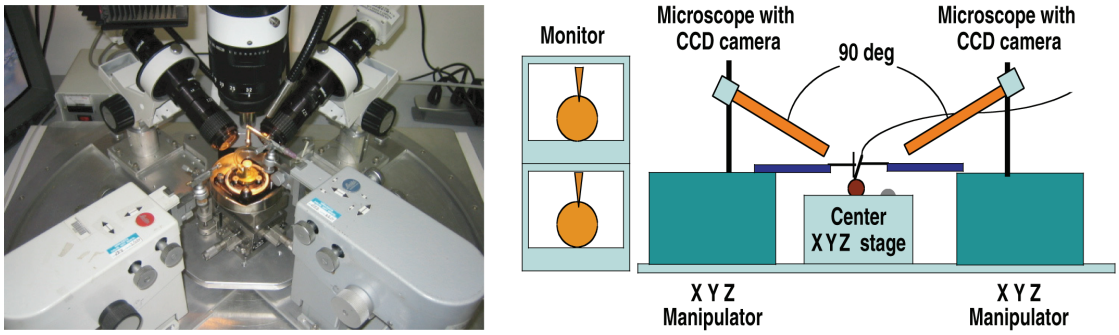

Fig. 3-64. A picture and schematic of the assembly station setup used to attach the fill tubes to the shells.

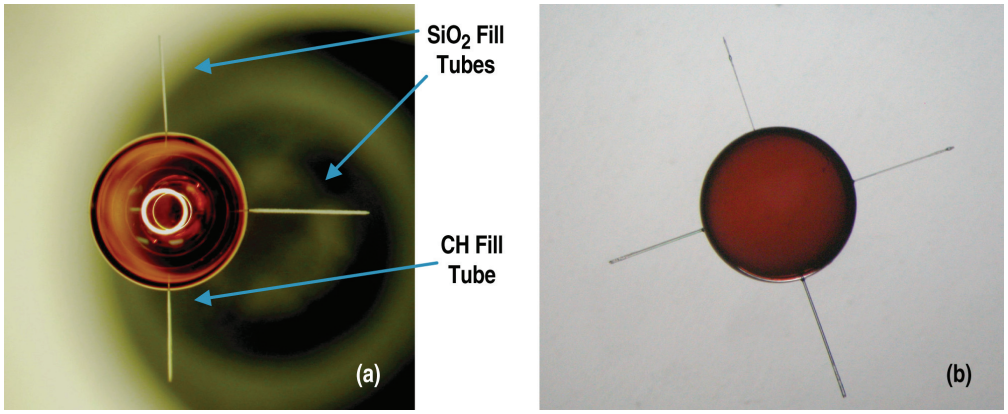

Fig. 3-65. (a) A three-tube target with both constant diameter CH and SiO_2 fill tubes attached. (b) A four tube (all SiO_2) target with varying tube diameters.

Fully assembled targets were characterized using optical and x-ray microscopy for fill tube length, diameter, glue fillet height and diameter. X-ray characterization, as shown in Fig. 3-66, revealed internal details of the targets such as fill tube insertion depth and fill tube wall thickness.

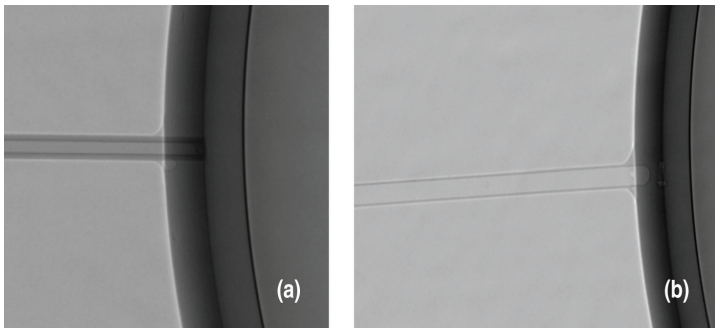

Fig. 3-66. (a) X-ray image of a SiO_2 fill tube attachment. (b) X-ray image of a CH fill tube attachment. Note different wall thickness and x-ray absorption of the SiO_2 and CH fill tubes.

Conclusion for Section 3.18

Fourteen different multiple fill tube targets were fabricated for experiments at SNL. Four SiO_2 fill tubes with diameters ranging from 10 to 45 μm were attached to one group of capsules. Three and four fill tube targets with constant diameters but varying composition of CH and SiO_2 were also fabricated. The Z-pinch experimental results provided important data for comparison to simulations and for their implication on NIF capsules with fill tubes.

3.19. FABRICATION OF PRESSURIZED 2 mm Be TARGETS FOR ICF EXPERIMENTS — E.H. Lundgren, A.C. Forsman, M.L. Hoppe, K.A. Moreno, A. Nikroo (GA)

We developed a method for laser drilling micro fill holes in 2 mm Be capsules, pressurizing them with deuterium and diagnostic gas (Ar) and resealing them. This is accomplished using a diode-pumped, Nd:YAG laser configured to perform double-pulse machining as described in Section 3.2 [3-5]. Be shells coated on a polymer mandrel are placed on a horizontal mount attached to micron resolution, motorized XYZ linear stages located inside a laser drilling vacuum chamber, and pumped down to < 200 mTorr. The shells are accurately traversed to the focal point of the focusing lens and subsequently drilled. The focal spot is a diffraction limited 5 μm spot. For laser drilling, the focal spot needs to be ± 20 μm from the middle of the shell wall.

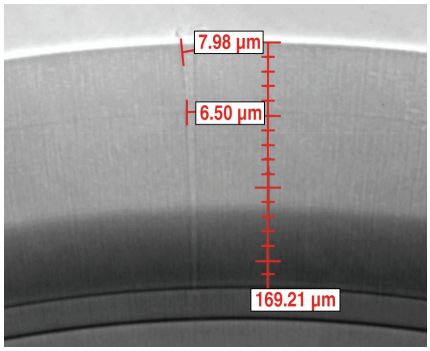

Fig. 3-67. X-Radia image of laser drilled hole in ~ 2 mm o.d. × ~ 170 μm wall Be/Be-Cu/GDP shell.

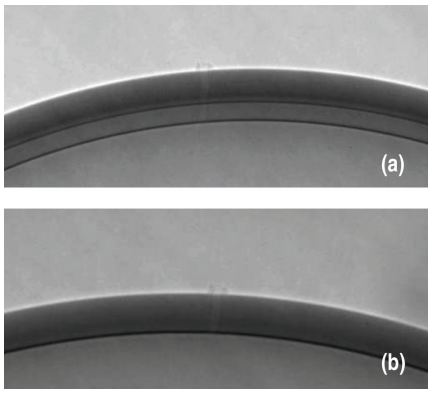

Fig. 3-68. (a) X-Radia image of a 2 mm shell with ~ 25 μm Be coating on a ~ 14 μm GDP mandrel after laser drilling. (b) The same shell with the GDP mandrel removed after pyrolysis for ~ 60 h at ~ 425°C.

Due to the varying thicknesses and material dopants in the Be coatings [3-76], drilling time and energy must be altered to ensure a through-hole is created as well as to avoid back-wall damage and larger hole diameters. On most holes, a soft start procedure is used to help minimize the entrance hole diameter. This procedure consists of firing a burst of laser pulses at reduced power before drilling with a longer burst of pulses at full power. Typical parameters for drilling 160-μm thick NIF shells are: soft start at 50 mW for 10 ms, main drilling burst at 400 mW for 250 ms. Hole characterization is accomplished using the X-Radia x-ray transmission microscope system. A radiographic image of a laser drilled hole is shown in Fig. 3-67.

Once the Be-coated GDP shells are laser drilled, they are placed in a furnace and baked in air to remove the polymer mandrel [3-19]. After the pyrolysis is complete, x-radiography is used to verify mandrel removal (Fig. 3-68).

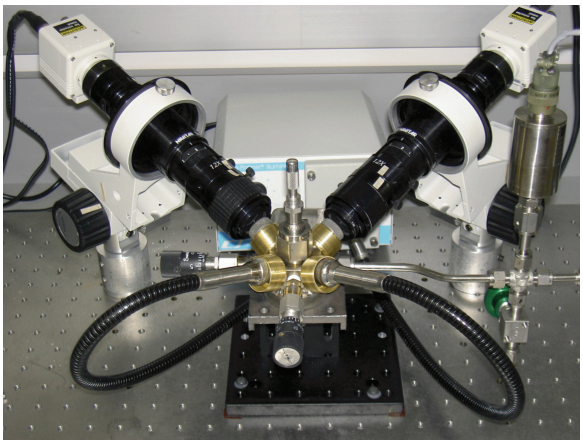

Fig. 3-69. Be shell pressure-sealing chamber.

For ICF experiments on NIF, capsules need to be pressurized and sealed with hydrogen isotopes and diagnostic gases. A five-way valve was modified and engineered into a pressure-sealing chamber, shown in Fig. 3-69, which was pressure tested for up to ~ 35 atm fill. A Be shell with laser-drilled hole facing up is held on a base-plate located at the bottom of the sealing chamber. The base-plate can be traversed in the X, Y and Z directions using modified metering valves as manipulators. Four viewports are located 90 deg apart, two for microscope cameras and two for lighting the chamber interior. After pressurizing the chamber and shell with the appropriate gas mixture, uv glue is applied to the shell through a ~ 120 μm diameter metal tube attached to a manipulator in the top of the chamber.

Once uv glue is applied to the fill-hole, uv light is introduced through the viewports to polymerize the glue and entrap the gas fill. Hundreds of shells have been sealed with the system with a very high success rate. Measurements from both non-destructive (mass spectroscopy and XRF) and destructive (burst testing) techniques have confirmed that the shells hold the desired gas fills [3-77].

3.20. CHARACTERIZATION OF EMBEDDED SPHERES IN OPAQUE FOAMS — K.K. Dannenberg, D.G. Schroen, C.A. Frederick, E.M. Giraldez, C.A. Back (GA), C.O. Russell, R.R. Holt, W.J. Krych (Schafer)

Astrophysical jets were traditionally observed and studied through telescopes. Recently, these phenomena were studied in computer simulations and scaled laser experiments. The current experiments utilized embedded spheres in opaque foams to mimic an astrophysical jet encountering a molecular cloud. In order to compare the simulation to the experiment, the sphere center must be built accurately and characterized to ± 50 μm with respect to the center of the drive region.

Repeatable fabrication of sphere-embedded foams is challenging due to shrinking that occurs during the drying phase of foam casting. Because precise sphere placement is not achievable during foam fabrication, the foam must be characterized before assembly. It is also difficult to optically diagnose the sphere location to the required specification, so the assembled target must be radiographed as well.

For assembly, placement of the center of the sphere must be within 50 μm of the requested build. The build and characterization can be completed with the use of two radiography systems, X-Radia and a Manson source located at SNL. The fabrication and characterization of this complex target are discussed below.

3.20.1. Fabrication of Sphere Embedded Foam

Fabrication of the sphere-embedded foam target is challenging. The specifications for the cylindrical foam are approximately 6 mm in length with an outer diameter of 4 mm. The center of the sphere is located 350 ± 50 μm radially from the center and 925 ± 50 μm from the cylindrical end surface.

To accomplish this, a pre-casting assembly was made (Fig. 3-70) comprised of a machined end cap with a hole drilled into it to support a 100 μm stalk. The cap also has a cut out which serves as a fiducial for radiographic metrology. After insertion, the 100 μm stalk was trimmed to the correct length (±10 μm of the desired length) and the CH sphere was glued in place. A glass sleeve was then placed around the assembly, meeting with an edge of the end cap.

The RF solution was mixed and poured into the completed assemblies; placed in vacuum for about 20 to 25 min to remove air; then cured for 48 h. Following, the assemblies were placed in isopropanol alcohol and chemicals were exchanged for one week. The wet foam was then released from the glass sleeve and remained attached to the end cap. The wet foam was pristine, and the specifications for sphere location were maintained. The foam was then critically dried. In this phase of fabrication, the foam changes dimensionally. The changes can be as large as the specified tolerances. These changes necessitate post fabrication measurements of each target.

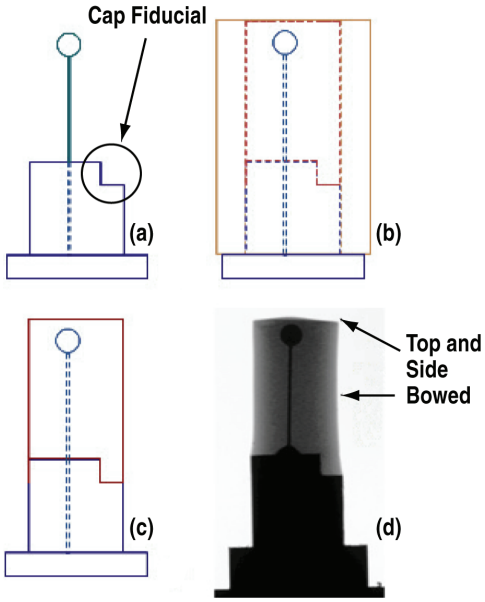

Fig. 3-70. (a) The support stalk and sphere were mounted into the cap. (b) The foam was cast into the glass sleeve placed around cap base. (c) The wet foam was released and specifications were maintained. (d) The foam shrunk during the drying phase.

3.20.2. Foam Characterization

For three quarters of the targets, the final build required that the center of the sphere be located 350 ± 50 μm radially offset from the jet axis and 925 ± 50 μm offset from the titanium washer. In order for this to be accomplished, the sphere location, within each foam, must be known to ± 25 μm.

Backlighting the foams enabled optical measurements of the sphere, but the sphere center was difficult to diagnose. Optically the sphere location can be characterized to ± 40 μm. Radiography was required for more precise characterization.

Two radiography systems were used to quantify the sphere location before and after fabrication. Initially, the X-Radia machine at GA in San Diego, was used. The X-Radia machine produced 25 keV over a 30 s period to provide quick images with lower contrast. These images were useful during

initial screening to ensure foam integrity. These images were difficult to use for further characterization because quantification of the sphere location with respect to the foam edge was needed, and the edges of the foam were difficult to identify. Next a Manson source at SNL, producing 5 keV broadband energies over a five-minute period, was used to provide good contrast imaging of the targets. The three features needed for sphere location quantification (the sphere, the cap fiducial and the foam edge) were easily viewed (Fig. 3-71). The fiducial in the cap was aligned edge on in the radiography system and a five-minute exposure was taken. Following, the target was rotated 90 deg and a second five-minute exposure was taken. The two orthogonal views allow for sphere quantification measurements to approximately ± 26 μm.

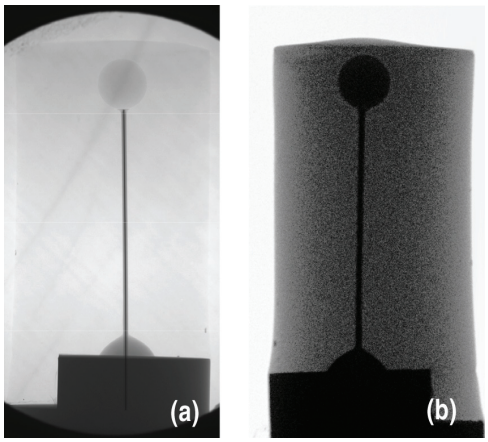

Fig. 3-71. (a) X-Radia image of ~ 6 mm tall foam target. (b) SNL Manson source image of the target.

3.20.3. Target Assembly

To quantify the needed parameters for assembly, four images at 45 deg increments were taken on the Manson source at SNL. The radiographic images were then imported into a CAD software package and the individual foams were modeled. Once the foams were modeled, they were exported to an overlay that was displayed on the assembly station viewing system. The targets were then built to specification by aligning the component with the CAD image on the screen. The final target was then radiographed once more and the sphere location was quantified to ± 26 μm with respect to the jet drive region (Fig. 3-72).

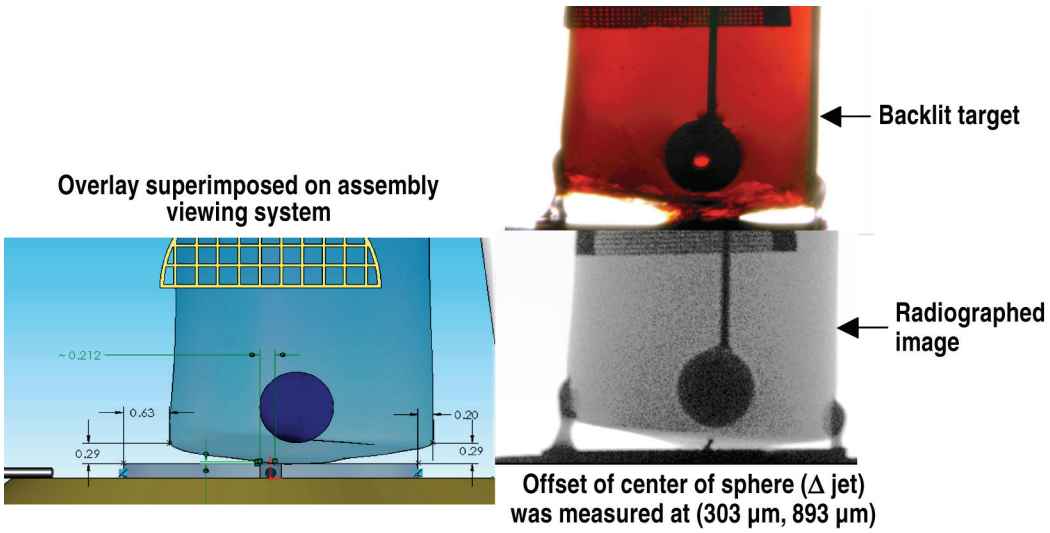

Fig. 3-72. Jet source and sphere center were simultaneously positioned and measured using CAD overlay acquired from radiography images. The assembly was completed and the offset was measured to a ± 26 μm accuracy.

Conclusions for Section 3.20

Quantification of the sphere location with respect to the jet drive source was needed to provide feedback for computer simulation comparisons. Precision characterization for sphere embedded foams was achieved using radiography and CAD overlays. Radiography was required for the characterization of these targets for two reasons: target integrity validation and sphere quantification. The X-Radia machine at GA allowed for the foam/sphere integrity assessment. The Manson source at SNL enabled the quantification of the sphere location with respect to the jet drive source. In the future, we would like to pursue completing this characterization with high-resolution x-ray imaging (similar to X-Radia) at lower energies.

DEVELOPMENT AT SCHAFER

3.21. PLANAR TARGET DELIVERIES AND DEVELOPMENT — K. Shillito (Schafer)

Schafer provided planar target deliveries to UR/LLE throughout FY06 and provided targets on this contract to NRL for a small portion of the year. Targets consisted of cast polymer films, machined components with surface features such as sine wave patterns and low density foam components from the RF, carbonized resorcinol formaldehyde (CRF), DVB, PS and silica aerogel foam systems. Our group continues to provide extensive support to our customers both in routine targets and completely new target design requests. In spite of short lead times and tightening specifications, we were able to meet all target requests on time.

We continue to provide the standard Nike targets. These targets consist of flat or patterned polystyrene, planar RF foam thin films, patterned RF foam, planar DVB foam and several required coatings. We also developed gas bag target techniques that satisfied requests in a short time frame. Per UR/LLE requirements, we provided thin aerogel "foils" and polyimide windows over LEHs on hohlraums.

Many of the standard targets specifications have been tightened. The standard cryogenic target mount (CTM) target for NRL with polyimide and a micro-machined step plate was improved through various micromachining techniques and the addition of a Precitech diamond turning lathe to our facility that greatly enhances our capabilities. Combining advances in machining with improved assembly, we were able to improve the standard specification considerably from 3 to 1 μm/mm.

Foam support for both UR/LLE and NRL included delivery of targets as well as development of new and unique designs and processes to achieve better quality and more uniform foams. The foams produced include DVB flat films, RF flat films, RF rippled films and targets that include RF with a polystyrene film. Recent developments include chemical surface modification on substrates to prevent cast foam films from sticking. This eliminated cracking and surface damage to the foam and produced very uniform and flat films. Other development areas include making RF films thinner than previously available and making flat CRF films.

We delivered polyimide gas bag targets. They were fabricated by attaching a spin coated 0.5 μm polyimide film to 3 mm diameter precision machined washers. A fill tube was attached to the washer that allowed the gas bags to be filled in the target chamber. This developmental effort was accomplished in just under three months.

All assemblies were done in a Class 100 clean environment, where the hallways and rooms are also held to a Class 10,000 cleanliness level. We assembled polystyrene hemi-shells onto 15 um Kevlar fibers as shown in Fig. 3-73, and also attached polyimide windows to the LEH of Au hohlraums shown in Fig. 3-74.

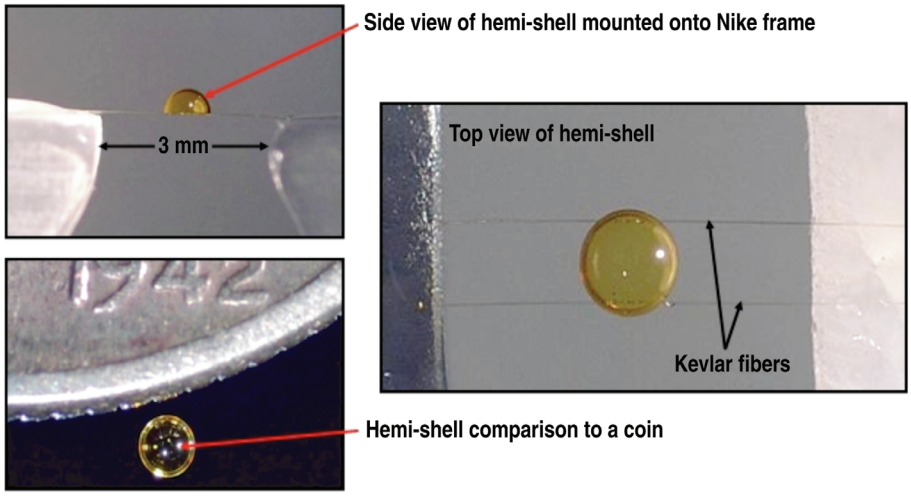

Fig. 3-73. Hemi-shells are mounted to 15 μm diameter Kevlar fibers.

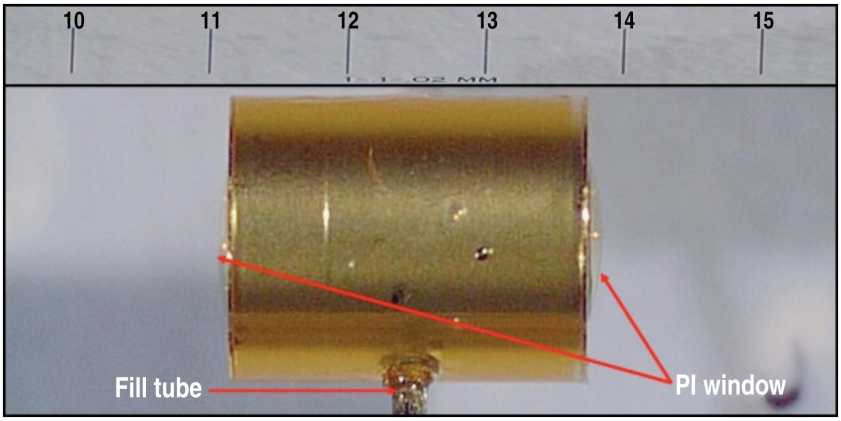

Fig. 3-74. Hohlraum with 0.6 μm polyimide (PI) windows mounted on each laser entrance hole and backfilled with 15 psi of nitrogen gas. The polyimide films are produced at Schafer.

Figure 3-75 displays a view through the hohlraum laser entrance hole exhibiting the clarity of a 0.6 μm polyimide film.

An example of one of the gas bag targets that we developed and delivered is shown in Fig. 3-76. Time for development to delivery of this type target was approximately three months.

Some of our target requests involved assembling double foils where one foil was smooth and the other had a machined sine wave pattern then both separated by a 75 μm air gap. This target is shown in Fig. 3-77.

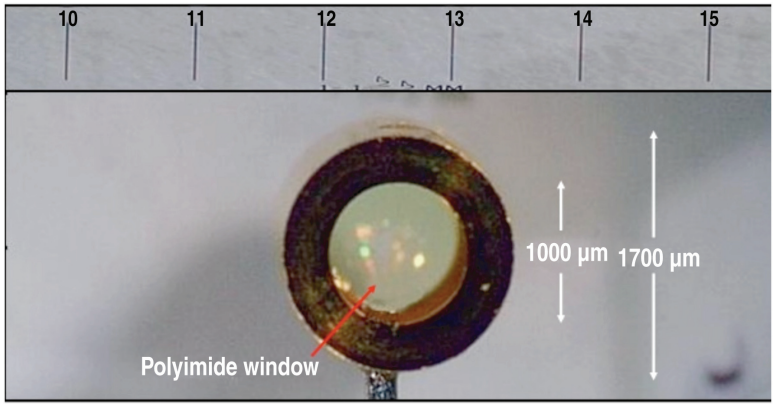

Fig. 3-75. View through the Au hohlraum laser entrance hole showing the clarity of a 0.6 μm polyimide film.

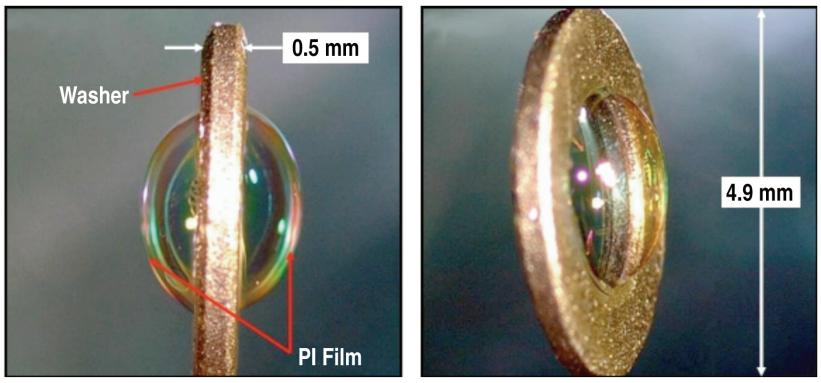

Fig. 3-76. A 0.5-μm thick polyimide film is attached to both sides of a washer with a fill-tube connected to the bottom of the washer. Photos show gas bag holding 15 psi.

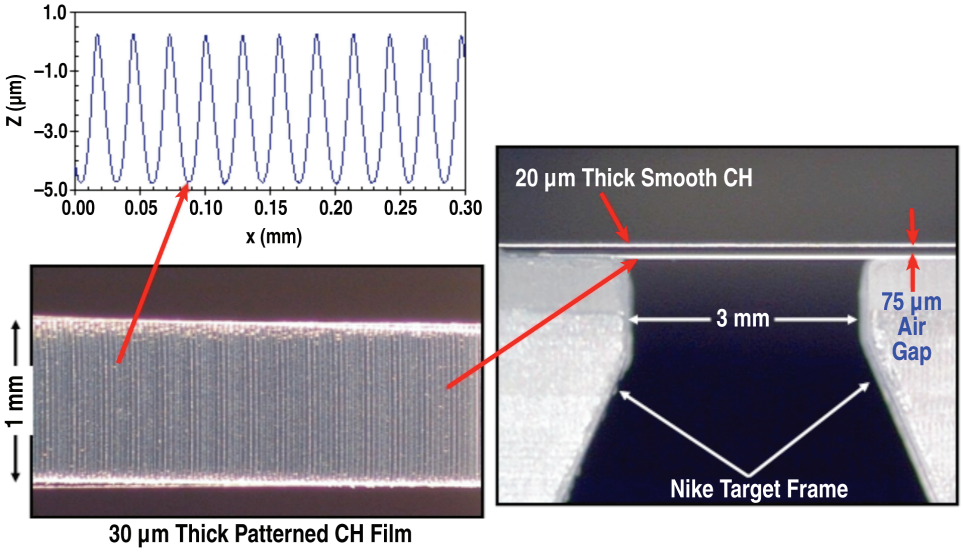

Fig. 3-77. Double foil targets. Two foil targets from both smooth and diamond-turned cast polystyrene foils.

3.22. A DUAL DENSITY FOAM ANNULUS — D.G. Schroen (GA), R. Holt (SCHAFER)

Sandia has begun experiments to test the theory that the Z-Pinch machine can generate three shaped pulses appropriate for hot spot ignition of high yield ICF capsules. Experiments by Mike Cuneo have demonstrated a reproducible and tunable foot pulse (a first shock) produced by the interaction of the outer and inner wire arrays. A second shock is produced by the inner array collision with a central foam target. The third shock is produced by stagnation of the inner array at axis [3-78].

The second shock is expected to be tunable by adjusting the foam radius and density. To test that theory, Mike Cuneo requested a foam annulus with two areas of different density. The densities requested were 8.9 and 13.4 mg/cc, with the tolerance of ±10%. In addition, the ratio of the two density regions had to be maintained (1:1.5). The two sections were to be joined without glue. The foam was requested to be 11 mm tall, 7.2 mm in diameter with an inner diameter of 4 mm. The foam type was specified to be poly 4-methyl-1-pentene (TPX).

TPX is routinely used in Z experiments for very pragmatic reasons. It casts well to net shape, has a density range of 2 to 250 mg/cm^3, and can be produced in as little as three days. The foam is created by dissolving the polymer in cyclohexane, pouring the solution into a mold, degassing the solution, freezing the solution, trimming off any excess solution from the mold, and lastly, removing the solvent by freeze drying. To make the annulus foam, we used a five-piece mold (Fig. 3-78).

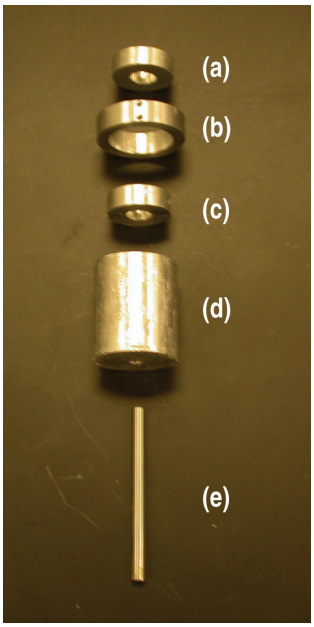

Fig. 3-78. The five piece mold. (a) The first inner ring sets the outside diameter and height of one of the two density regions. (b) The outer ring is an alignment ring that holds the two inner rings together. (c) The second inner ring sets the o.d. and height of the second density region. (d) The base holds the second inner ring and the gauge pin slides through the base to align to both inner rings. The long length of the base is required to hold the gauge pin straight. (e) The gauge pin sets the internal diameter of the annulus.

To cast the foam, the pin and second inner ring are put on the base. The assembly is cooled on a cold plate held at about -25°C. The high-density solution is added inside the inner ring and the whole assembly is placed in a -25°C freezer. The outer ring and other inner ring are also placed in the freezer at this time. After the solution has completely frozen, the assembly is removed and the solution is trimmed to the height of the inner ring. The outer ring and other inner ring are added to the assembly and the low-density solution is added. The assembly is placed back into the freezer. After the second solution is frozen, it is also trimmed. The gauge pin is removed and the assembly is placed into a freeze drier. A resultant foam is shown in Fig. 3-79.

To characterize the foams, we have a custom radiography system. It is composed of a Manson source with a vanadium target, a vacuum sample chamber and a CCD detector. All of our TPX samples are analyzed under vacuum because the foam has very little x-ray absorption as it is composed of CH_2 and is typically very low density (2 to 20 mg/cm^3). A typical characterization looks

for density variations. For this foam, the analysis had to be more detailed. The radiograph had to determine the densities of the two areas. The Manson source is not stable from run to run, so a standard was created. It was composed of 10 steps of 11-μm thick polypropylene film obtained from Goodfellow. Radiographs of the standard and a foam target are shown in Fig. 3-80.

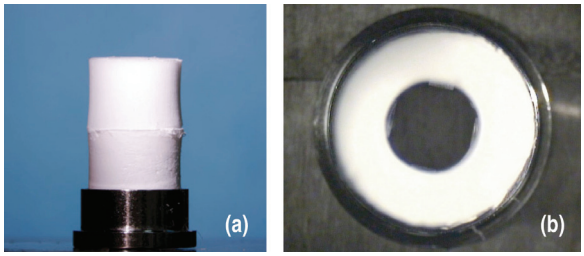

Fig. 3-79. (a) Side view and (b) top view of the foam from shot 1712 on the Z machine. The densities of the two sections were 14.2 and 9.9 mg/cm^3.

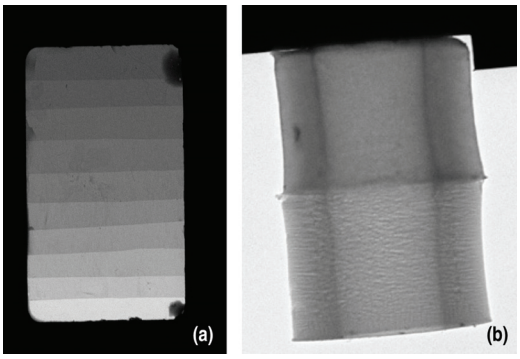

Fig. 3-80. (a) A typical radiograph of the 10 step CH_2 standard. (b) The radiograph of the foam shown in Fig. 3-79.

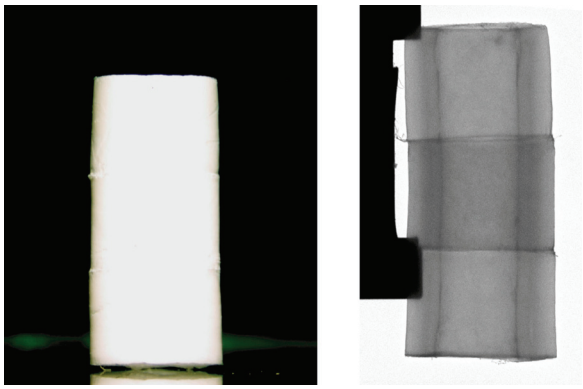

Fig. 3-81. A side view optically and radiographically of the three section foam annulus. The foam is 15.5 mm tall, 7 mm o.d., and 4 mm i.d.

To calibrate the x-ray absorption the CCD counts from each step of the standard were determined and plotted. Then the absorptions of the thin strip in the center of the two sections of the annulus radiograph were plotted. This determined the equivalent film thickness of the two densities and their ratio. The foam was weighed and measured to obtain the total volume and density, the two component densities were calculated from the absorption ratio and volume of the two sections. To confirm density uniformity, the foam was rotated 90 deg and a second radiograph was taken.

The fabrication experiments were deemed a success, and it was requested that a three density annulus should be prototyped for experiments on ZR. We modified the process slightly by (1) adding another inner ring and outer alignment ring, (2) using only the cold plate to freeze the TPX solution and (3) by monitoring the temperature of the mold using an IR camera. By adding the TPX solutions when the mold was 10°C, we were able to cast the foam with more uniform seams. There is a slight shift to the side between the three foam sections; we expect to correct this by carefully tightening the set screws in the outer alignment ring. The three-section foam annulus created is shown in Fig. 3-81.

We feel that this prototype foam demonstrates that we can produce an annulus with three distinct density regions. We will attempt to make the foam to the correct dimensions for ZR when they become known.

References for Section 3

[3-1] F. Elsner, Fusion Technol. **35**(2), 81 (1999).

[3-2] M. Paunovic and M. Schlesinger, *Fundamentals of Electroplating Deposition,* 2nd ed., (Wiley Interscience, 2006).

[3-3] A.F. Mayadas and M. Shatzkes, Phys. Rev. B **1**, 1382 (1970).

[3-4] J.P. Armstrong et al., Fusion Sci. Technol. **49**, 822 (2006).

[3-5] A.C. Forsman, P.S. Banks, M.D. Perry, et al., J. Appl. Phys. **98**, 033302 (2005).

[3-6] Sierra 532, manufactured by the Commercial Lasers Group of General Atomics.

[3-7] R.J. Burt, S.F. Meyer, and E.J. Hsieh, "Radio Frequency Magnetron Sputtering of Thick Film Amorphous Beryllium," J. Vac. Sci. Technol. **17**, 407 (1980).

[3-8] R. McEachern, C. Alford, R. Cook, D. Makowcki, and R. Wallace, "Sputter-Deposited Be Ablators for NIF Target Capsules," Fusion Technol. **31**, 435 (1997).

[3-9] H.W. Xu, A. Nikroo, J.R. Wall, R. Doerner, M. Baldwin, and J.H. Yu, "Be Coating on Spherical Surface for NIF Target Development," Fusion Sci. Technol. **49**, 778 (2006).

[3-10] M. McElfresh, J. Gunther, C. Alford, et al., "Fabrication of Beryllium Capsules with Copper-Doped Layers for NIF Targets: A Progress Report," Fusion Sci. Technol. **49**, 786 (2006).

[3-11] A.F. Jankowski, M.A. Wall, and T.G. Nieh, "Crystallization of Beryllium-Boron Metallic Glasses," J. Non-Crystalline Solids **317**, 129 (2003).

[3-12] A.F. Jankowski, M.A. Wall, and T.G. Nieh, "Synthesis and Thermal Stability of Amorphous Be-B-X Alloy Coatings," J. Non-Crystalline Solids **351**, 900 (2005).

[3-13] A.F. Jankowski, M.A. Wall, A.W. Van Buuren, et al., "From Nanocrystalline to Amorphous Structure in Beryllium-Based Coatings," Acta Materialia **50**, 4791 (2002).

[3-14] M. Schaepkens, T.W. Kim, A.G. Erlat, M. Yan, K.W. Flanagan, C.M. Heller, and P.A. McConnelee, "Ultrahigh Barrier Coating Deposition on Polycarbonate Substrates," J. Vac. Sci. Technol. A **22**, 1716 (2004).

[3-15] G.L. Graff, R.E. Williford, and P.E. Burrows, "Mechanisms of Vapor Permeation through Multilayer Barrier Films: Lag Time Versus Equilibrium Permeation," J. Appl. Phys. **96**, 1840 (2004).

[3-16] S. Haan, et al., "Ignition Point Design Requirements for Be Capsule in Gas-Filled Hohlraum," 2005.

[3-17] H.W. Xu, et al., "Beryllium Capsule Coating Development for NIF Targets," presentation for the 17th Annual Target Fabrication Specialists' Meeting, San Diego, California, 2006.

[3-18] S.A. Letts, et al., "Removal of the Inner CH Mandrel Using Pyrolysis," presentation for the 16th Target Fabrication Specialists' Meeting, Scottsdale, Arizona, 2005.

[3-19] R.C. Cook, S.A. Letts, S.R. Buckley, E. Fearon, "Pyrolytic Removal of the Plastic Mandrel from Sputtered Beryllium Shells," Fusion Sci. Technol. **49**(4), 802 (2006).

[3-20] G. Ervin, et al., "Catastrophic Oxidation of Beryllium Metal," J. Nucl. Mater. **12**(1), 30 (1964).

[3-21] W.B. Jepson, et al., "Some Topographical Observations on the Oxidation of Beryllium," J. Nucl. Mater. **10**(3), 224 (1963).

[3-22] R.C. Montesanti, et al., "Phase Shifting Diffraction Interferometer for Inspecting NIF Ignition Target Shells," presentation for the 17th Annual Target Fabrication Specialists' Meeting, San Diego, California, 2006.

[3-23] H. Huang, R.B. Stephens, S.A. Eddinger, et al., "Non-destructive Quantitative Dopant Profiling Technique by Contact Radiography," Fusion Sci. Technol. **49**(4), 650 (2006).

[3-24] http://www.cxro.lbl.gov/optical_constants/atten2.html

[3-25] A. Snigirev, I. Snigireva, V. Kohn, S. Kuznetsov, and I. Schelokov, "On the Possibilities of X-ray Phase Contrast Microimaging by Coherent High-Energy Synchrotron Radiation," Rev. Sci. Instrum. **66**, 5486 (1995).

[3-26] S.C. Mayo, P.R. Miller, S.W. Wilkins, et al., "Quantitative X-ray Projection Microscopy; Phase-Contrast and Multi-Spectral Imaging," J. Microscopy **207**, 79 (2002).

[3-27] D.S. Montgomery, A. Nobile, and P.J. Walsh, "Characterization of National Ignition Facility Cryogenic Beryllium Capsules using X-ray Phase Contrast Imaging," Rev. Sci. Instrum. **75**, 3986 (2004).

[3-28] S.W. Wilkins, T.E. Gureyev, D. Gao, A. Pogany, and A.W. Stevenson, "Phase-Contrast Imaging using Polychromatic Hard X-rays," Nature **384**, 335 (1996).

[3-29] A. Pogany, D. Gao, S. W. Wilkins, "Contrast and Resolution in Imaging with a Microfocus X-ray Source." Rev. Sci. Instrum. **68**, 2774 (1997).

[3-30] T.E. Gureyev, S.W. Wilkins, "On X-ray Phase Imaging with a Point Source," J. Opt. Soc. Am. A **15**, 579 (1998).

[3-31] K.C. Chen, R.C. Cook, H. Huang, S.A. Letts, and A. Nikroo, "Fabrication of Graded Germanium-Doped CH Shells," Fusion Sci. Technol. **49**, 750 (2006).

[3-32] S.W. Haan, T. Dittrich, G. Strobel, et al., "Update on Ignition Target Fabrication Specifications," Fusion Sci. Technol. **41**, 164 (2002).

[3-33] A. Nikroo, J. Bousquet, R. Cook, et al., "Progress in 2 mm Glow Discharge Polymer Mandrel Development for NIF," Fusion Sci. Technol. **45**, 165 (1994).

[3-34] A. Nikroo and D. Woodhouse, "Bounce Coating Induced Domes on Glow Discharge Polymer Coated Shells," Fusion Sci. Technol. **35**, 202 (1999).

[3-35] M. Theobald, B. Dumay, C. Chicanne, et al., "Roughness Optimization at High Modes for GDP CH_x Microshells," Fusion Sci. Technol. **45**, 176 (1994).

[3-36] S.A. Letts, D.W. Myers, and L.A. Witt, "Ultrasmooth Plasma Polymerized Coatings for Laser Fusion Targets," J. Vac. Sci. Technol. **19**, 739 (1981).

[3-37] M. Theobald, C. Chicanne, J. Barnouin, E. Peche and P. Baclet, "Gas Etching to Obtain Germanium Doped CH_x Microshells Compatible with the Laser Megajoule Target Specifications," Fusion Sci. Technol. **49**, 757 (2006).

[3-38] D. Czechowicz, D. Steinman, C. Chen and J. Dorman, "Investigations to Remove Domes from Plastic Shells by Polishing" Proc. 17th Target Fabrication Specialists' Meeting, San Diego, California, 2006, to be published in Fusion Sci. Technol.

[3-39] G.E. Sommargren, D.W. Phillion, M.A. Johnson, et al., "100-Picometer Interferometry for EUVL," Proc. SPIE **4688**, 316 (2002).

[3-40] J.L. Klingmann and G.E. Sommargren, "Sub-Nanometer Interferometry and Precison Turning for Large Optical Fabrication," Lawrence Livermore National Laboratories Report UCRL-JC-134052 (1999).

[3-41] S.W. Haan, et al., "Update on Specifications for NIF Ignition Targets, and Their Rollup into an Error Budget," Fusion Sci. Technol. **49**(4), 553 (2006).

[3-42] N. Izumi, et al., "Experimental Study of Fill-Tube Hydrodynamic Effects on Implosions Using Capsules with Plastic Stalks," presented at the 47th Annual Meeting of the Division of Plasma Physics, Denver, Colorado, 2005.

[3-43] D.G. Czechowicz, et al., "Development of Fill Tube Surrogate Targets for Hydrodynamic Experiments," Proc. 17th Target Fabrication Specialists' Meeting, San Diego, California, 2006, to be published in Fusion Sci. Technol.

[3-44] J. Burmann, et al., "One Piece Capsule/Fill Tube Assemblies," presented at the 12th Target Fabrication Specialists' Meeting, Jackson Hole, Wyoming, 403 (1998).

[3-45] N. Izumi, et al., "Experimental Study of Fill-Tube Hydrodynamic Effects on Implosions Using Capsules with Plastic Stalks," presented at the 48th Annual Meeting of the Division of Plasma Physics, Philadelphia, Pennsylvania, 2006.

[3-46] E.L. Alfonso, et al., "Monolithic Fill Tube Fabrication," Proc. 17th Target Fabrication Specialists' Meeting, San Diego, California, 2006, to be published in Fusion Sci. Technol.

[3-47] D.C. Wilson, P.A. Bradley, N.M. Hoffman, et al., "The Development and Advantages of Beryllium Capsules for the National Ignition Facility," Phys. Plasmas **5**, 1953 (1998).

[3-48] D.A. Steinman, R.B. Stephens, and M.L. Hoppe, "A Novel Technique for Precisely Measuring the Thickness of Witness Plates," Fusion Technol. **49**, 635 (2006).

[3-49] E. Lifshin, *X-ray Characterization of Materials* (Wiley-VCH, New York, 1999).

[3-50] J. Cooley, private communication (2005)

[3-51] M. Hoppe and E. Castillo, "Polishing of Beryllium Capsules to Meet NIF Specifications," J. Phys. IV (Paris) **133**, 895 (2006).

[3-52] M.L. Hoppe,, "Large Glass Shells from GDP Shells," Fusion Technol. **38**, 42 (2000).

[3-53] M.L. Hoppe,, "Recent Developments in Making Glass Shells from Silicon Doped GDP Shells," Fusion Technol. **41**, 234 (2002).

[3-54] S.A. Letts, E.M. Fearon, S.R. Buckley, et al., "Fabrication of Polymer Shells Using a Decomposable Mandrel," Fusion Technol. **28**, 1797 (1995).

[3-55] R.H. Deremus, *Glass Science* (Wiley, New York, 1973) Ch. 8.

[3-56] W.J. Miller, KMSF Semi-Annual Technical Report (1989) pp. 34-38.

[3-57] J. Edwards, Phys. Plasmas **12**, 056318-1 (2005).

[3-58] A.Q.L. Nguyen and E.L. Alfonso, "Deterministic Fabrication and Characterization of Fill Tube Surrogate Targets for OMEGA Experiments Using a Polymer Stalk," presented at the 17th Target Fabrication Specialists' Meeting, San Diego, California, October 1-5, 2006.

[3-59] M. Takagi, C. Frederick, A. Nikroo, R. Cook, K. Saito, "Fabrication and Attachment of Polyimide Fill Tubes to Plastic NIF Capsules," presented at the 16th Target Fabrication Specialists' Meeting, San Diego, California, 2006.

[3-60] S. Skupsky, et al., "Advance Direct-Drive Target Designs for NIF," Proc. 3rd Intl. Conf. on Inertial Fusion Sciences and Applications, 2003 (American Nuclear Society Inc., La Grange Park, IL, 2004) pp. 61-64.

[3-61] M. Bonino, et al., "Retention of D_2 and DT in Plastic Shell Targets Using Thin Aluminum Layers," Proc. 11th Annual Target Fabrication Specialists' Meeting, Orcas Island, Washington, 1996.

[3-62] R.W. Pekala, et al., "Organic Aerogels from the Polycondensation of Resorcinol with Formaldehyde," J. Mater. Sci. **24**, 3221 (1989).

[3-63] S.M. Lambert, et al., "Fabrication of Low-Density Foam Shells from Resorcinol-Formaldehyde Aerogel," J. Appl. Polymer Sci. **65**, 2111 (1997).

[3-64] A. Nikroo, D. Czechowicz, R. Paguio, A.L. Greenwood, M. Takagi, "Fabrication and Properties of Overcoated Resorcinol-Formaldehyde Shells for OMEGA Experiments," Fusion Technol. **45**, 84 (2004).

[3-65] R.R Paguio, et al., "Fabrication Capabilities for Spherical Foam Targets used in ICF Experiments," Proc. 21st IEEE/NPSS Symp. on Fusion Engineering, Knoxville, Tennessee, 2005.

[3-66] R.R. Paguio, et al., "Fabrication of Modified Density and Tin Doped Resorcinol Formaldehyde Foam Shells and Beads for Direct Drive Experiments," Polymeric Materials: Sci. and Engin. **95**, 872 (2006).

[3-67] B.W. McQuillian, A. Nikroo, D.A. Steinman, et al., "The PAMS/GDP Process for Production of ICF Target Mandrels," Proc. 11th Annual Target Fabrication Specialists' Meeting, Orcas Island, Washington, 1996; Fusion Technol. 381 (1997).

[3-68] M. Takagi, R. Cook, R. Stephens, J. Gibson, S. Paguio, "Decreasing Out-of-Round in Poly(α-Methylstyrene) Mandrels by Increasing interfacial Tension," Fusion Technol. **38**(1), 46 (2001).

[3-69] R.R. Paguio, S.P. Paguio, C.A. Frederick, A. Nikroo, O. Acenas, "Improving the Yield of Target Quality OMEGA Sized PAMS Mandrels by Modifying Emulsion Components," Fusion Technol. **49**(4), 743 (2006).

[3-70] R.R. Paguio et al., "Fabrication and Overcoating of Divinylbenzene Foam Shells Using Dual Initiators," J. Appl. Polymer Sci. **101**(4), 2523 (2006).

[3-71] B. Song, et al., "Determination of Interfacial Tension from the Profile of a Pendant Drop Using Computer-Aided Image Processing," J. Colloid and Interface Sci. **184**, 77 (1996).

[3-72] B.E. Yoldas, J. Mater. Sci. **10**, 1856 (1975).

[3-73] T.F. Baumann, et al., Chem. Mater. **17**, 395 (2005).

[3-74] G.H. Miller, E.I. Moses, C.R. Wuest, "The National Ignition Facility," Opt. Engin. **43**, 2481 (2004).

[3-75] M. Takagi, et al., "Development of Deuterated Polystyrene Shells for Laser by Means of a Matched Emulsion Method," Vac. Sci Technol. A **9**, 2145 (1991).

[3-76] A. Nikroo, K.C. Chen, M.L. Hoppe, et al., "Progress Towards Fabrication of Graded Doped Beryllium and CH Capsules for the National Ignition Facility," Phys. Plasmas **13**, 056302 (2006).

[3-77] E.L. Alfonso, J.S. Jaquez, A. Nikroo, "Using Mass-Spectrometry to Characterize Permeation Half-Life of ICF Targets," Fusion Sci. Technol. **49**, 773 (2006).

[3-78] M. Cuneo, R. Vesey, D. Sinars, et al., "Demonstration of Radiation Pulse Shaping with Nested-Tungsten-Wire-Array Z Pinches for High-Yield Inertial Confinement Fusion," Phys. Rev. Lett. **95**(18) 185001 (2005).

4. PUBLICATIONS

Items with GA/Schafer efforts supported by the contract for Target Component Fabrication and Technology Development Support are marked with an asterisk.

4.1. List of Publications

Back, C.A., Hurricane, O.A., Hammer, J.H., Castor, J.I., Maclaren, S.A., Landen, O.L., Rosen, M.D., "Radially-Resolved Measurements of the Effect of Boundary Walls in Radiation Transport Experiments," Bull. Am. Phys. Soc. **50**, 108 (2005).

Back, C.A., Kilkenny, J.D., et al., "Underdense Radiation Sources: Moving Towards Longer Wavelengths," Proc. Intl. Fusion Sciences and Applications, Biarritz, France, 2005; J. Phys. IV France **133**, 1173 (2006).

Back, C.A., et al., "Absolute Time-Resolved Emission of Non-Local Thermodynamic Equilibrium L-Shell Spectra from Ti-Doped Aerogels," J. Quant. Spectrosc. Radiat. Transfer **99**, 21 (2006).

Bernat, T.P., et al., "Ignition Target Fabrication and Fielding of the National Ingition Facility," Proc. Intl. Fusion Sciences and Applications, Biarritz, France, 2005; J. Phys. IV France **133** (2006) 857.

Bozek, A.S., Alexander, N.B., Bittner, D., Carlson, L., Drake, T.J., Flint, G., Frey, D.T., Goodin, D.T., Grant, S., Hund, J.F., Kilkenny, J.D., Petzoldt, R.W., Schroen, D., Stemke, R.W., Streit, J., Vermillion, B.A., "The Production and Delivery of Inertial Fusion Energy Power Plant Fuel: The Cryogenic Target," Proc. 24th Symp. on Fusion Technology, Warsaw, Poland, 2006, to be published in Fusion Engin. Design; General Atomics Report GA–A25529 (2006).

DeBono, B., Karim, Z., Waqschal, K., Beg, F.N., Stephens, R.B., "Capsules Using a Compact X-pinch," Bull. Am. Phys. Soc. **50**, 152 (2005).

*Forsman, A.C., Perry, M.D., Campbell, E.M., et al., "Double-pulse machining as a technique for the enhancement of material removal rates in laser machining of metals," J. Appl. Physics **98**, 33302 (2005).

*Forsman, A.C., Komashko, A.M., Dodell, A.L., Armas, M.S., Lundgren, E.H., "SuperPulse: A Double Pulse Format for Increasing the Speed and Quality of Laser Machining," Proc. Advanced Laser Applications Conference (ALAC), Novi, Michigan, 2006.

*Fuchs, J., Sentoku, Y., Nikroo, A., Campbell, E.M., Stephens, R.B., et al., "Comparative Spectra and Efficiencies of Ions Laser-Accelerated from the Front and Rear Surfaces of Thin Foils," Phys. Rev. Lett. **94**, 045004 (2005).

Gallix, R., Rickman, W.S., Alexander, N.B., "Proposed Design and Mass Production of Wire Arrays and Targets for a Z-Pinch IFE Power Plant," Proc. Intl. Fusion Sciences and Applications, Biarritz, France, 2005; J. Phys. IV France **133**, 825 (2006); General Atomics Report GA–A25172 (2005).

Gallix, R., Rickman, W.S., Alexander, N.B., "Z-Pinch IFE, Task 2 — IFE Power Plant Technology Load Production and Debris Removal, Final Report for SNL" General Atomics Report GA–A25247 (2005).

Goodin, D.T., Alexander, N.B., Besenbruch, G.E., Bozek, A.S., Brown, L.C., Carlson, L.C., Flint, G.W., Goodman, P., Kilkenny, J.D., Maksaereekul, W., McQuillan, B.W., Nikroo, A., Paguio, R.R., Petzoldt, R.W., Raffray, R., Schroen, D.G., Sheliak, J.D., Spalding, J., Streit, J.E., Tillack, M.S., Vermillion, B.A., "Developing a Commercial Production Process for 500,000 Targets per Day — A Key Challenge for Inertial Fusion Energy," 47th Annual Meeting of Division of Plasma Physics, Denver, Colorado, 2005, to be published in Phys. Plasmas; General Atomics Report GA–A25258 (2005).

Goodin, D.T., Petzoltd, R.W., Vermillion, B.A., Frey, D.T., Alexander, N.B., Flint, G.W., Brown, L.C., Bozek, A.S., Goodman, P., Maksaereekul, W., McQuillan, B.W., Nikroo, A., Paguio, R.R., "Target Manufacturing — A 'Grand Challenge' for Inertial Fusion," Proc. Intl. Fusion Sciences and Applications, Biarritz, France, 2005; J. Phys. IV France **133**, 35 (2006). Complete version to be published in a topical issue of the European Journal of Physics D on Inertial Fusion Science and Applications, 2005.

Goodin, D.T., Alexander, N.B., Brown, L.C., Callahan, D.A., Ebey, P., Frey, D.T., Gallix, R., Geller, D., Gibson, C.R., Hoffer, J., Maxwell, J.L., Mcquillan, B.W., Nikroo, A., Nobile, A., Olson, C., Petzoldt, R.W., Raffray, R., Rickman, W.S., Rochau, G., Schroen, D.G., Sethian, J., Sheliak, J., Streit, J.E., Tillack, M., Vermillion, B.A., Valmianski, E.I., "Demonstrating a Target Supply for Inertial Fusion Energy," Proc. 16th ANS Topical Meeting on the Technology of Fusion Energy, Madison, Wisconsin, 2004, Fusion Sci. Technol. **47**(4), Part 2, 1131 (2005); General Atomics Report GA–A24816 (2004).

Goodin, D.T., "Developing a Commercial Production Process for 500,000 Targets per Day — A Key Challenge for Inertial Fusion Energy," Bull. Am. Phys. Soc. **50**, 308 (2005).

Hoppe, M.L., Robinson, J.R., "Strength and Permeation Properties of SiO_2 Shells Produced from Silicon Doped GDP Shells," submitted to Fusion Sci. Techol.; General Atomics Report GA–A25260 (2005).

Huang, H., Stephens, R.B., Gunther, J., "Measuring Dopant Concentration in Graded NIF Targets through Quantitative Contact X-Radiography," Bull. Am. Phys. Soc. **50**, 107 (2005).

Huang, H., Vermillion, B.A., Brown, L.C., Besenbruch, G.E., Goodin, D.T., Stemke, R.W., Stephens, R.B., "Evaluation of Fluidized Beds For Mass-Production of IFE Targets," Fusion Sci. Technol. **47**, 46 (2005).

*Kilkenny, J.D., "The Role of Experimental Science in ICF — Examples From X-Ray Diagnostics and Targets," Proc. Intl. Fusion Sciences and Applications, Biarritz, France, 2005; J. Phys. IV France **133,** 101 (2006). Complete version to be published in a topical issue of the European Journal of Physics D on Inertial Fusion Science and Applications, 2005.

*Kilkenny, J.D., Alexander, N.B., Nikroo, A., Steinman, D.A., Nobile, A., Bernat, T.P., Cook, R.C., Letts, S.A., Takagi, M., Harding, D., "Laser Targets Compensate for Limitations in Inertial Confinement Fusion Drivers," Laser and Particle Beams **23**, 475 (2005).

McQuillan, B.W., Besenbruch, G.E., Brown, L.C., Rennels, R.A., Wong, B.Y., "Metal Sulfate Water-Splitting Thermochemical Hydrogen Production Cycles," Proc. 16th World Hydrogen Energy Conf. Lyon, France, 2006.

*Nikroo, A., Chen, K.C., Hoppe, M.L., Huang, H., Wall, J., Xu, H.W., McElfresh, M., Alford, C., Cook, R., Cooley, J.C., Field, R., Hackenburg, R., Doerner, R., Baldwin, M., "Progress Towards Fabrication of Graded Doped Beryllium and CH Capsules for the National Ignition Facility," 47th Annual Meeting of Division of Plasma Physics, Denver, Colorado; Phys. Plasmas **13**, 056302 (2006); General Atomics Report GA–A25285 (2005).

*Nikroo, A., Pontelandolfo, J., Greenwood, A.L., Stillwell, J.L., Callahan, D.A., "Fabrication of Capsules with Angle-Dependent Gold Shims for Hohlraum Drive Symmetry Correction," 15th Intl. Symp. on Heavy Ion Inertial Fusion, Princeton, New Jersey, 2004, Nucl. Instrum. and Methods in Physics Research A **544**, 42 (2005); General Atomics Report GA–A24774 (2004).

*Paguio, R.R., Frederick, C.A., Hund, J.F., Czechowicz, D.G., Nikroo, A., Takagi, M., Acenas, O., Thi, M., "Fabrication Capabilities for Spherical Foam Targets Used in ICF Experiments," Proc. 21st IEEE/NPSS Symp. on Fusion Engineering, Knoxville, Tennessee, 2005; CD Rom, IEEE Catalog No. 05CH37764C, ISBN: 1-4244-0150-X, Library of Congress: 85-654749. (2005); General Atomics Report GA–A25228 (2005).

*Paguio, R.R., Nikroo, A., Takagi, M., Acenas, O., "Fabrication and Over-coating of Divinylbenzene Foam Shells Using Dual Initiators," J. Appl. Polymer Sci. **101**(4), 2523 (2006).

*Paguio, R.R., Nikroo, A., Hund, J.F., Frederick, C.A., Jaquez, J.S., Takagi, M., Thi, M., "Fabrication of Hollow Silica Aerogel Spheres for Direct Drive Inertial Confinement Fusion (ICF) Experiments," Mater. Res. Soc. Symp. Proc. Vol. 901E © 200, 0901-Ra05-23-Rb05-23.1. (2006).

Project Staff, "Inertial Confinement Fusion Annual Report, October 1, 2004 through September 30, 2005," General Atomics Report GA-A25242 (2005).

Project Staff, "Inertial Confinement Fusion Annual Report, October 1, 2003 through September 30, 2004," General Atomics Report GA–A24675 (2005).

Steinman, D.A., Stephens, R.B., Hoppe, M.L., "A Novel Technique for Precisely Measuring the Thickness of Witness Plates," Proc. 16th Target Fabrication Specialists' Meeting, Scottsdale, Arizona, 2005, to be published in Fusion Sci. Technol.; General Atomics Report GA–A25059 (2005).

*Stephens, R.B., Eddinger, S.M., Xu, H.W., et al., "A Potential X-Pinch Based Point X-Ray Source for Phase Contrast Imaging of Inertial Confinement Fusion Capsules," Proc. Intl. Fusion Sciences and Applications, Biarritz, France, 2005; J. Phys. IV France **133**, 761 (2006).

*Stephens, R.B., Steinman, D.A., Hoppe, M.L., "White Light Interferometry for the Optical Characterization of Transparent ICF Shells," Fusion Sci. Technol. **49**(4), 646 (2005); General Atomics Report GA–A25055 (2005).

Wong, B.Y., Brown, L.C., Besenbruch, G.E., Chen, Y., McQuillan, B.W., et al., "A Comprehensive Assessment of Solar Thermochemical Water-Splitting Cycles for Hydrogen Production." to be published in the Intl. J. Hydrogen Energy (2006).

Wong, B.Y., Brown, L.C., Besenbruch, G.E., Chen, Y., McQuillan, B.W., et al., "Evaluation of Water-Splitting Thermochemical Hydrogen Cycles Applicable to Solar Thermal Systems," Proc. 13th Intl. Symp. on Concentrating Solar Power and Chem. Engin. Techologies, Seville, Spain, 2006.

Wong, B.Y., Trester, P., "Materials Development for Sulfur-Iodine Thermochemical Hydrogen Production Process," in *Materials for the Hydrogen Economy*, eds. R.H. Jones and G.J. Thomas, Publisher: CRC Press LLC, to be published, 2007.

*Xu, H.,Youngblood, K.P., Nikroo, A., Hackenberg, R., Cooley, J., "Boron Doped Beryllium Coatings for NIF Target Development," Proc. AVS 53rd Intl. Symp. and Exhibition, San Francisco, California, 2006.

4.2. List of Presentations

Alexander, N.B., "Target Mounting Systems for Rep-Rated Lasers," 17th Target Fabrication Specialists' Meeting, San Diego, California, October 1-5, 2006.

*Alfonso, E.L., "Monolithic Fill-Tube Target Development Update," 17th Target Fabrication Specialists' Meeting, San Diego, California, October 1-5, 2006.

*Bernat, T., "Thermal and Electrical Conductivities of Electroplated Gold," 17th Target Fabrication Specialists' Meeting, San Diego, California, October 1-5, 2006.

*Brocato, B., "Flexure of Composite Polymer Laser Targets," 17th Target Fabrication Specialists' Meeting, San Diego, California, October 1-5, 2006.

*Burmann, J., "Ultra-Precision Assembly of Innovative Hohlraums," 17th Target Fabrication Specialists' Meeting, San Diego, California, October 1-5, 2006.

*Carter, S., Matthews, D., "New ICF Target Developments," 17th Target Fabrication Specialists' Meeting, San Diego, California, October 1-5, 2006.

*Chen, K.C., "Graded Ge-Doped CH Capsule with Reduced Isolated Surface Domes," 17th Target Fabrication Specialists' Meeting, San Diego, California, October 1-5, 2006.

*Czechowicz, D., "Tungsten Sputter Coating Development to Produce Hi-Z Shells," 17th Target Fabrication Specialists' Meeting, San Diego, California, October 1-5, 2006.

*Czechowicz, D., "Investigations to Improve the Surface Finish of Plastic Shells by Minimizing and Removing Domes," 17th Target Fabrication Specialists' Meeting, San Diego, California, October 1-5, 2006.

*Dannenburg, K., "Characterization of Embedded Spheres in Opaque Foams," 17th Target Fabrication Specialists' Meeting, San Diego, California, October 1-5, 2006.

*Eddinger, S., "Measuring Opacity Variations in NIF Shells," 17th Target Fabrication Specialists' Meeting, San Diego, California, October 1-5, 2006.

*Forsman, A., "Drilling of Small High Aspect Ratio Holes in Beryllium Shells," 17th Target Fabrication Specialists' Meeting, San Diego, California, October 1-5, 2006.

*Frederick, C., "Structural Investigation of Resorcinol Formaldehyde Foams using Ultra Small Angle Scattering," 17th Target Fabrication Specialists' Meeting, San Diego, California, October 1-5, 2006.

*Frederick, C., "Fabrication of Multiple Fill Tube Targets for Sandia National Laboratory," 17th Target Fabrication Specialists' Meeting, San Diego, California, October 1-5, 2006.

Frey, D., "Mass Production Layering of Fuel for Inertial Fusion Targets," 17th Target Fabrication Specialists' Meeting, San Diego, California, October 1-5, 2006.

Gallix, R., "Unitized Wire Arrays for Z-Pinch Machines: A Feasibility Study," 17th Target Fabrication Specialists' Meeting, San Diego, California, October 1-5, 2006.

*Gibson, C., "Design of the NIF Cryogenic Target System," 17th Target Fabrication Specialists' Meeting, San Diego, California, October 1-5, 2006.

*Gibson, J., "Full-Surface Wall-thickness Measurements and 3D Visualization," 17th Target Fabrication Specialists' Meeting, San Diego, California, October 1-5, 2006.

*Giraldez, E., "An Overview of Fast Ignition and High Energy Density Physics Target Fabrication at General Atomics," 17th Target Fabrication Specialists' Meeting, San Diego, California, October 1-5, 2006.

Goodin, D. "The Status of Developing the Target Supply for Inertial Fusion Energy," 17th Target Fabrication Specialists' Meeting, San Diego, California, October 1-5, 2006.

*Hoppe, M., "New Developments in Si-GDP to Glass Shells — Residual Gases, Gas Filling and Tailored Half-Lives," 17th Target Fabrication Specialists' Meeting, San Diego, California, October 1-5, 2006.

*Huang, H., "Quantitative Radiography: Film Model Calibration and Dopant/Impurity Measurement in ICF Targets," 17th Target Fabrication Specialists' Meeting, San Diego, California, October 1-5, 2006.

*Huang, H., "Quantitative Radiography: Submicron Dimension Calibration and ICF Target Characterization," 17th Target Fabrication Specialists' Meeting, San Diego, California, October 1-5, 2006.

*Hund, J., "Fabrication and Characterization of Aluminum Oxide Aerogel Backlighter Targets," 17th Target Fabrication Specialists' Meeting, San Diego, California, October 1-5, 2006.

*Hund, J., "Fabrication and Characterization of Machined Tantalum Oxide Aerogel," 17th Target Fabrication Specialists' Meeting, San Diego, California, October 1-5, 2006.

*Jaquez, J., "Al Coatings as a Deuterium Permeation Barrier on Foam Shells and the Dependence on Foam Surface Finish," 17th Target Fabrication Specialists' Meeting, San Diego, California, October 1-5, 2006.

*Kaae, J., "Fabrication of an Unusual Halfraum," 17th Target Fabrication Specialists' Meeting, San Diego, California, October 1-5, 2006.

*Kittelson, M., "Prediction of High Density Resorcinol Formaldehyde (RF) Foam Shell Dimensions Using In-Process Measurements," 17th Target Fabrication Specialists' Meeting, San Diego, California, October 1-5, 2006.

*Krych, J., "Particulate Doped TPX Foams and Embedded Foil Foams for the Z Accelerator at Sandia National Laboratories," 17th Target Fabrication Specialists' Meeting, San Diego, California, October 1-5, 2006.

*Lee, T., "Wallmap Wall Thickness Variation Measurement Optimization," 17th Target Fabrication Specialists' Meeting, San Diego, California, October 1-5, 2006.

*Lundgren, E., "Laser Drilling Through-Holes in Be Foils and Shells Using a Trepanning System," 17th Target Fabrication Specialists' Meeting, San Diego, California, October 1-5, 2006.

*Lundgren, E., "2 mm Beryllium Shell Fabrication for Sandia National Laboratories," 17th Target Fabrication Specialists' Meeting, San Diego, California, October 1-5, 2006.

*Luo, R., "Adjusting Coating Parameters to Optimize GDP Gas Barrier on RF Shells," 17th Target Fabrication Specialists' Meeting, San Diego, California, October 1-5, 2006.

Maudlin, M., "Design and Fabrication of Targets for Proton Focus Cone Fast Ignition Experiments," 17th Target Fabrication Specialists' Meeting, San Diego, California, October 1-5, 2006.

*Moreno, K., "Fabrication and Characterization of Be flats for Omega Experiments," 17th Target Fabrication Specialists' Meeting, San Diego, California, October 1-5, 2006.

*Moreno, K., "Comparison of Techniques to Measure Thin Gold Coatings on Cylindrical Substrates for Cocktail Hohlraum Development," 17th Target Fabrication Specialists' Meeting, San Diego, California, October 1-5, 2006.

*Mota, B., "Verifying PVD Thin Film Thickness," 17th Target Fabrication Specialists' Meeting, San Diego, California, October 1-5, 2006.

*Nguyen, A., "Deterministic Fabrication and Characterization of Fill Tube Surrogate Targets for OMEGA Experiments Using a Polymer Stalk," 17th Target Fabrication Specialists' Meeting, San Diego, California, October 1-5, 2006.

*Nikroo, A., "Investigation of Deuterium Permeability of Sputtered Beryllium and Graded Copper Doped Beryllium Shells," 17th Target Fabrication Specialists' Meeting, San Diego, California, October 1-5, 2006.

*Paguio, R., "Improving the Wall Uniformity of High Density Resorcinol Formaldehyde Foam Shells for Direct Drive Experiments by Modifying Emulsion Components," 17th Target Fabrication Specialists' Meeting, San Diego, California, October 1-5, 2006.

Petta, R., "Target Fabrication and Characterization for High Energy Density Physics Experiments," 17th Target Fabrication Specialists' Meeting, San Diego, California, October 1-5, 2006.

Russell, C., "Indium Bonding for Equation of State Experiments at the Z-Accelerator at Sandia National Laboratories," 17th Target Fabrication Specialists' Meeting, San Diego, California, October 1-5, 2006.

Schroen, D., "A Dual Density Foam Annulus For Z," 17th Target Fabrication Specialists' Meeting, San Diego, California, October 1-5, 2006.

*Sheliak, J., "Solid DT Surface Roughness Measurement Corrections for DT Layers with High Density Bubble Populations," 17th Target Fabrication Specialists' Meeting, San Diego, California, October 1-5, 2006.

*Smith, J., "Deformation of Panel Counter-Bores Used in Isentropic Compression Experiments," 17th Target Fabrication Specialists' Meeting, San Diego, California, October 1-5, 2006.

*Steinman, D., "Improvements in Capsule Gas Fill Half-life Determination," 17th Target Fabrication Specialists' Meeting, San Diego, California, October 1-5, 2006.

Stephens, R., "Target Production Systems for Rep-Rated Lasers," 17th Target Fabrication Specialists' Meeting, San Diego, California, October 1-5, 2006.

*Stolp, J., "Multi-Axis Assembly Station for Omega Targets," 17th Target Fabrication Specialists' Meeting, San Diego, California, October 1-5, 2006.

*Streit, J., "Divinylbenzene Foam Shell Coatings for the High Average Power Laser (HAPL) Program," 17th Target Fabrication Specialists' Meeting, San Diego, California, October 1-5, 2006.

*Taylor, J., "Nexiv Confocal Microscope Capabilities for Experimental Components at the Z-Accelerator at Sandia National Laboratories," 17th Target Fabrication Specialists' Meeting, San Diego, California, October 1-5, 2006.

Valmianski, J., "Target Acceleration Stress, Deflection and Free Vibration," 17th Target Fabrication Specialists' Meeting, San Diego, California, October 1-5, 2006.

*Vermillion, B., "Development of a GDP Coater Enabling Increased Production," 17th Target Fabrication Specialists' Meeting, San Diego, California, October 1-5, 2006.

*Wilkens, H., "Fabrication and Characterization of NIF-scale Cocktail Hohlraums," 17th Target Fabrication Specialists' Meeting, San Diego, California, October 1-5, 2006.

*Xu, H., "Beryllium Capsule Coating Development for NIF Targets," 17th Target Fabrication Specialists' Meeting, San Diego, California, October 1-5, 2006.

*Youngblood, K., "Characterization of Contaminants in Beryllium Capsules," 17th Target Fabrication Specialists' Meeting, San Diego, California, October 1-5, 2006.

ACKNOWLEDGMENT

This report of work was prepared for the U.S. Department of Energy under Contract No. DE-AC03-01SF22260.